



Universiteit
Leiden
The Netherlands

Patient-specific in-vivo QA in MRGRT: 3D EPID dosimetry for the Unity MR-linac

Torres Xirau, I.

Citation

Torres Xirau, I. (2020, September 15). *Patient-specific in-vivo QA in MRGRT: 3D EPID dosimetry for the Unity MR-linac*. Retrieved from <https://hdl.handle.net/1887/136754>

Version: Publisher's Version

License: [Licence agreement concerning inclusion of doctoral thesis in the Institutional Repository of the University of Leiden](#)

Downloaded from: <https://hdl.handle.net/1887/136754>

Note: To cite this publication please use the final published version (if applicable).

Cover Page



Universiteit Leiden



The handle <http://hdl.handle.net/1887/136754> holds various files of this Leiden University dissertation.

Author: Torres Xirau, I.

Title: Patient-specific in-vivo QA in MRGRT: 3D EPID dosimetry for the Unity MR-linac

Issue Date: 2020-09-15

P A T I E N T - S P E C I F I C
I N - V I V O Q A I N M R G R T :
3 D E P I D D O S I M E T R Y F O R
T H E U N I T Y M R - L I N A C

PROEFSCHIRFT

ter verkrijging van

*de graad van Doctor aan de Universiteit Leiden,
op gezag van Rector Magnificus prof.mr. C.J.J.M. Stolker,
volgens besluit van het College voor Promoties
te verdedigen op dinsdag 15 september 2020*

klokke 11.15 uur

door

*Iban Torres Xirau
geboren te Barcelona in 1987*

Dedication.

A la mama. Per cuidar-nos i estimar-nos tant.

P A T I E N T - S P E C I F I C
I N - V I V O Q A I N M R G R T :
3 D E P I D D O S I M E T R Y F O R
T H E U N I T Y M R - L I N A C

Iban Torres Xirau

*Gepersonaliseerde kwaliteitsbeoordeling door MRGRT-
behandelingen: 3D-dosimetrie met EPID voor de Unity
MR-Linac*

*Avaluació personalitzada de qualitat en tractaments
MRGRT: dosimetria 3D mitjançant EPID per a l'Unity
MR-Linac*

Promotor:

Prof. Dr. U.A. van der Heide

Co-promotor:

Dr. A. Mans (NKI-AvL)

Promotiecommissie:

Prof. Dr. C.R.N. Rasch (LUMC)

Prof. Dr. B.W. Raaymakers (UMC Utrecht)

Dr. V. Hansen (Odense Universitetshospital)

Prof. Dr A. Webb (LUMC)

Prof. Dr. R.L.M. Haas (LUMC)

Dr. N. Jornet Sala (Hospital Sant Pau Barcelona)

ISBN: 978-94-6416-129-8

Cover design: Georgina Ferrer Brutau | www.vananaprints.com

Lay-out: Publiss | www.publiss.nl

Printing: Ridderprint | www.ridderprint.nl

Copyright © I. Torres 2020.

All rights reserved. No part of this book may be reproduced, stored in a retrieval system, or transmitted in any form or by any means, without prior written permission of the author.

The work on this thesis was performed at the Netherlands Cancer Institute in Amsterdam, and was funded by the Elekta AB (Stockholm, Sweden), grant NKI 2013 – 5937 and project 10088.

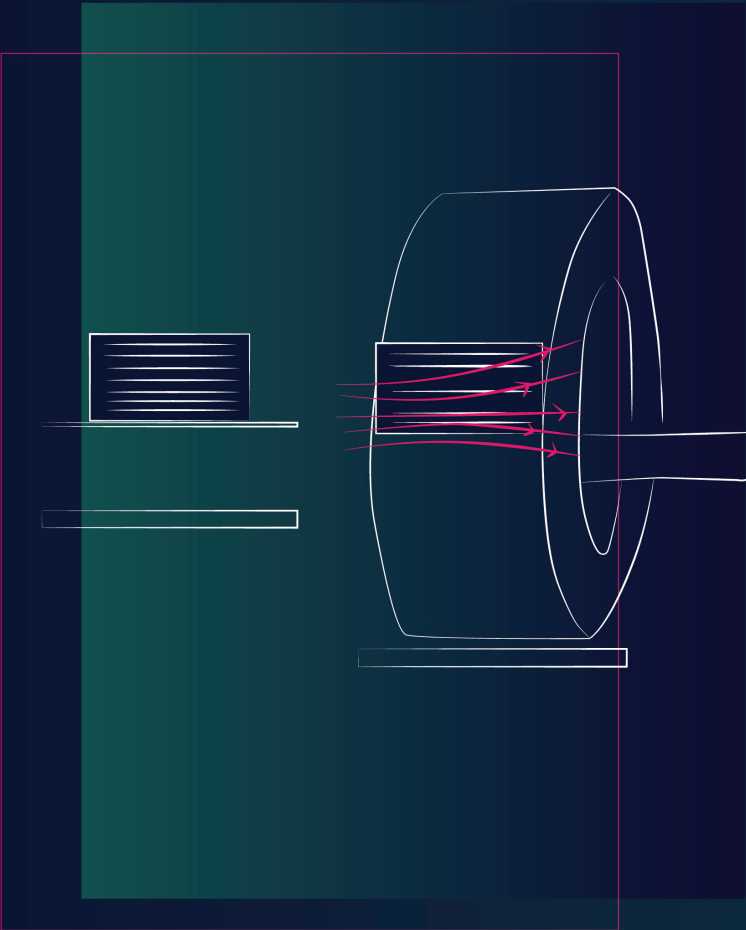
CONTENTS

Chapter 1	Introduction	11
Chapter 2	A back-projection algorithm in the presence of an extra attenuating medium: towards portal dosimetry for the MR-linac.	29
Chapter 3	Characterization of the A-Si EPID in the Unity MR-Linac for dosimetric applications	59
Chapter 4	Two dimensional EPID dosimetry for the MR-linac: proof of concept.	81
Chapter 5	3D dosimetric verification of unity MR-linac treatments by portal dosimetry.	107
Chapter 6	A Deep Learning-based correction to EPID dosimetry for attenuation and scatter in the Unity MR-Linac system	121
Chapter 7	General Discussion	141
Chapter 8	References	153
Chapter 9	Summaries	179
Chapter 10	Acknowledgments	193
Chapter 11	List of publications	199
Chapter 12	Curriculum Vitae	205

List of abbreviations:

ART	Adaptive radiotherapy
CBCT	Cone-beam computer tomography
CNN	Convolutional neural network
CT	Computed tomography
CTV	Clinical tumor volume
EPID	Electronic portal imaging device
EBRT	External-beam radiotherapy
ERE	Electron return effect
FFF	Flattening filter free
GTV	Gross tumor volume
H&N	Head and neck
IC	Ionization chamber
IMRT	Intensity modulated radiotherapy
ISQL	Inverse square law
DVH	Dose volume histogram
DL	Deep learning
DEEPID	Deep electronic portal imaging device
MLC	Multi-leaf collimator
MRI	Magnetic resonance imaging

MRIgRT	Magnetic resonance Imaging guided Radiotherapy
MU	Monitor unit
MV	Mega voltage
OAR	Organ at risk
PET	Positron emission tomography
PTV	Planning target volume
QA	Quality assessment
QC	Quality control
ReLU	Rectified linear unit
ROI	Region of interest
RT	Radiotherapy
TPS	Treatment planning system
VMAT	Volumetric arc therapy



1.

INTRODUCTION

1.1. Radiotherapy

Radiotherapy is one of the main treatment options for cancer, besides surgery and medical oncology. It is estimated that 60% of cancer patients ¹ receive it alone or in combination with other treatment modalities. The aim of this non-invasive and local treatment is to stop proliferation and eradicate malignant cells by exposing them to a high dose of ionizing radiation while minimizing the dose to the surrounding healthy tissue ². When irreparable damage has been done, the body will eliminate these cells. For body sites/tumor types where radiotherapy is generally applied, healthy cells typically have better and faster mechanisms to repair radiation damage than malignant cells, resulting in a higher sensitivity of tumor tissue to radiation damage. Furthermore, the higher the radiation dose to the target volume, the higher the probability that the malignant cells are killed. However, this is constrained by the accuracy of delivering high doses only to the tumorous cells while sparing the healthy tissue.

In the conventional radiotherapy workflow, a pre-treatment Computed Tomography (CT) scan of the patient is made in treatment position. This scan is used to delineate relevant anatomical structures such as the organs at risk (OAR), the gross tumor volume (GTV), clinical target volume (CTV) and the planning target volume (PTV), which results from applying a margin to the CTV to account for uncertainties (e.g. due to organ motion). Next, the optimal dose distribution is computed in the treatment planning system (TPS) balancing the prescribed target dose aims and OAR dose constraints.

1.2. Advances in radiotherapy treatment delivery

Radiotherapy techniques have changed significantly over the past few decades, thanks to improvements in engineering and computing.

Delivery of highly conformal dose distributions enveloping the shape of complex target volumes while avoiding neighboring healthy tissue has become feasible. Simultaneously, treatment complexity has increased from rectangular fields via 3D-conformal treatments to intensity-modulated radiotherapy (IMRT), volumetric arc therapy (VMAT) and tumor motion tracking using planning 4D CT images. Meanwhile patient setup verification has evolved from the use of portal films and 2D megavoltage (MV) imaging to 3D volumetric kV imaging using cone-beam CT (CBCT).

1.3. Imaging techniques

Currently, several imaging modalities are available in the pre-treatment phase. Examples are CT ³, positron emission tomography (PET) ⁴, single photon emission tomography (SPECT) ⁵, ultrasound (US) ⁶ and magnetic resonance imaging (MRI) ⁷. In addition to being used for tumor localization, most of these modalities are employed to visualize tumor tissue characteristics, like cell density, hypoxia or perfusion. Based on this information the dose can be prescribed heterogeneously to the tumor, giving a higher dose to high risk regions. By applying this ‘dose painting’ based on tumor characteristics the treatment of different kinds of malignancies may be improved ⁸⁻¹³.

1.4. Patient specific QA in conventional linacs

1.4.1. Why QA?

With the increase of complexity in radiotherapy treatments over the years, serious incidents have been reported ¹⁴⁻²⁰ and protocols have been established to learn from past errors ^{21,22}. Even though these incidents are recognized to be uncommon events, their impact on patients, staff and radiation oncology in general are harmful. Hence, a demand

for more robust and better quality assurance (QA) techniques has developed. While quality assurance aims at making sure that quality goals will be met in general, quality control (QC) is the regulatory process through which the quality goals are measured for specific standard cases. Quality assurance does not only reduce the likelihood of incidents to occur, it also increases the probability that they will be recognized and rectified sooner in case they occur.

1.4.2. Why patient specific QA

Patient specific QA entails the dosimetric verification of individual patient treatments (i.e. compares planned and measured dose distributions, either in a phantom geometry or using *in-vivo* data acquired during treatment), and aims to detect and reduce clinically relevant dosimetric deviations²³⁻²⁵. *In-vivo* dosimetry involves acquiring dose measurements during treatment delivery, reconstructing patient dose if needed, and comparing it to the intended dose.

Several tools for dosimetric patient specific QA exist; ionization chambers, diode array detectors, radiochromic film, polymer gel, and electronic portal imaging devices (EPIDs) are most commonly applied. In the following sections, the use of these tools for both pre-treatment and *in-vivo* QA is discussed.

1.4.3. Pre-treatment QA

‘Pre-treatment QA’ in radiotherapy is the general term for dose measurements performed in a phantom geometry. The patient plan is delivered to a phantom geometry containing a type of detector. The treatment plan is recalculated on the phantom geometry, and the measured and planned dose distributions are compared.

Radiochromic film is typically placed between the slabs of a polystyrene phantom. Given its high spatial resolution, it can be used for verification

of highly conformal dose distributions such as generated by IMRT²⁶⁻³¹. Thanks to its near tissue equivalence, radiochromic film can be used for 3D dosimetry by embedding multiple films between stacks of phantom slabs. Disadvantages of the use of radiochromic film are the need for elaborate calibration procedures and an impractical and tedious measurement procedure.

The use of point detectors such as ionization chambers (IC) or diodes^{32,33} for dosimetry in radiotherapy has been extensively studied³⁴⁻³⁹, and is considered the ground truth for absolute dosimetry. In pre-treatment QA, single detectors or 2D detector arrays are positioned inside a phantom to measure the absorbed dose in a point or plane. The spatial resolution of 2D arrays, however, tends to be poor in comparison to film, as the number of detectors that can be embedded is constricted by spatial limitations.

Polymer gel dosimetry has been used for pre-treatment 3D volumetric dosimetry in phantoms⁴⁰⁻⁴³. The gel dosimeter has potential for volumetric measurements with sub-mm spatial resolution. A major impediment to the introduction of gel dosimetry as a clinical tool, however, has been its complexity in terms of experimental handling.

An EPID (Electronic Portal Imaging Device) is a 2D detector that captures high-energy radiation, originally developed as an imaging device for patient position verification^{44,45}. EPIDs are mounted opposite to the radiation source and hence detect the radiation after it has left the phantom or patient. It was soon noted that EPIDs are also suitable for dosimetry⁴⁶, as the detected signal is proportional to the dose incident on the panel. For that purpose, it is necessary that pixel intensity is converted to dose, either at the panel level or by back-projecting it into the phantom geometry. EPIDs have the benefit that they can be used either for pre-treatment or *in-vivo* dosimetry.

Fluence detectors ^{47,48} are mounted on the linac head and can serve as an alternative to dose measurement devices in a phantom. When used in combination with a dose calculation engine, the dose distribution delivered to the patient geometry can be estimated. Besides pre-treatment verification, measurements can also be performed during treatment, allowing for dosimetric verification based on data obtained during patient treatment. A similar method for dose reconstruction uses the linac log files ^{49,50} as input. In this case, the linac log files (obtained pre-treatment or during treatment) are used, in combination with a dose calculation engine, to reconstruct dose in a certain geometry. However, the main drawback of log-file approaches is that they rely on the output of the linac.

Despite the effort and support from industry to develop accurate detectors, the use of pre-treatment dosimetry systems leaves some intrinsic issues unsolved:

- the measurements are performed in a phantom geometry. Therefore, the location of any observed dose deviations cannot be related to the patient geometry, complicating assessment of clinical impact.
- dosimetric deviations occurring during patient treatment remain undetected^{51,52}.
- the measurements require linac time and workload due to experimental setup and data analysis

The first issue is currently being addressed by radiotherapy QA vendors by transfer of measured dose onto the patient anatomy (using the planning CT scan). The latter two issues are fundamentally unsolvable by means of pre-treatment verification.

1.4.4. In-vivo QA

In *in-vivo* dosimetry the dose delivered to the patient is estimated from

a measurement performed during treatment. Such measurements can be achieved with detectors positioned in the body of the patient, or with measuring devices located in front of or behind the patient, in combination with a scan of the actual geometry of the patient. Next, the determined dose is compared to the intended dose as calculated by the TPS. Different methods are currently being employed for *in-vivo* dosimetry, based on point-based measurements^{53,54}, or EPIDs^{55-57 58-61}.

The use of point detectors for *in-vivo* dosimetry⁶²⁻⁶⁴ normally involves invasive routines, and often only provides a single point measurement, which makes it not ideal for IMRT.

EPIDs are nowadays the most important 2D transit detectors. The first *in-vivo* dosimetric application was exit-dosimetry⁶⁵⁻⁶⁸, where the dose in the EPID located behind the patient, was verified. Two approaches can be distinguished when using EPID for *in-vivo* dosimetry: in forward approaches^{56,69} the acquired portal dose is compared to the predicted dose at the EPID level, whereas in a back-projection approach⁷⁰ the acquired portal dose is used to reconstruct dose in the patient geometry⁷¹ and compared to the planned dose either in 2D or 3D. In the forward approach, the clinical interpretation of potential discrepancies is difficult as the connection with the patient geometry is missing. The back-projection approach, on the other hand, does not suffer from this drawback. When used for back-projection *in-vivo* dosimetry, the (planning) CT scan of the patient is used in combination with EPID images acquired during treatment. Using the transmission calculated from the CT scan, the dose information in the EPID image is back-projected into the patient geometry, with the EPID reconstructed 2D or 3D dose in the patient geometry as a result.

Interest for EPID based *in vivo* dosimetry has increased in the last years. As patient specific QA has become mandatory in several countries, vendors of radiotherapy QA systems, such as DosiSoft⁷², SunNuclear

⁷³, IBA⁷⁴ and Elekta⁷⁵ have released tools for *in vivo* dosimetry.

The use of fluence detectors or log file based dose reconstruction, in combination with the daily anatomy of the patient (for example CBCT) ^{49,50,76-81}, are potentially powerful methods for patient dose reconstruction. However, the limited capability of these systems to detect patient related errors and the lack of clinically available products makes that these solutions are not widely adopted.

1.4.5. Comparison metrics

Traditionally, the comparison between planned and measured dose distributions, both in 2D and 3D, is performed by means of γ -analysis ⁸², a method to determine the shortest distance in normalized dose-distance space between measured and reference dose curves. Both distance and dose difference are normalized using reference values, typically 3 mm (distance) and 3% (dose).

Dose Volume Histograms (DVHs) are histograms relating radiation dose to tissue volume. They are most commonly used as a dose evaluation tool, to compare dose distributions (e.g. from different plans or from measurement and planning) and to summarize 3D dose distributions in a graphical 2D format. Thus, they can provide an informative description of the deviations observed between delivered and planned dose distributions. Correlation studies showed clinical equivalence for γ - and DVH-based methods ^{83,84}.

1.5. 3D *in-vivo* EPID dosimetry at the Antoni Van Leeuwenhoek - Netherlands Cancer Institute

At the Netherlands Cancer Institute – Antoni Van Leeuwenhoek (NKI-AVL), 3D *in-vivo* EPID dosimetry, based on a back-projection method is the QA tool used for routinely verifying all radiotherapy treatments.

An algorithm was developed to use the EPID not only as a positioning tool, but also as a 2D transit dosimeter⁷⁰ for 3D CRT and IMRT treatments. Soon after, an extension of this work to for 3D verification was built^{58,85}. This was necessary to develop a tool capable of acquiring continuous EPID movies of VMAT treatments to verify arc therapy⁵⁹. Later, the method was improved for the presence of inhomogeneities in or near the irradiated volume⁸⁶. Since August 2011, the EPID-based dose reconstruction and γ -evaluation software runs automatically⁸⁷ for almost all treatments, yielding a dosimetry report for inspection within minutes after treatment delivery without any manual intervention. Further developments to the method have been made, such as the use of the ‘virtual’ reconstruction technique⁸⁸, which uses in-air EPID images to reconstruct the dose to any CT scan (phantom-less pre-treatment), and online EPID dosimetry⁸⁹ to stop the linac *during* treatment in case a large deviation is detected.

These improvements in automation allow for *in vivo* verification of almost all treatments with acceptable workload. When compared to phantom based dose verification, measurement time is greatly reduced, at the cost of an increase in inspection work. The clinical experience with the large scale *in vivo* dosimetry program has been shown^{51,90}.

1.6. The Unity MR-linac

Compared to other commonly used imaging modalities in radiotherapy, MRI provides superior soft-tissue contrast and thus a clear view of both tumorous tissue and OARs. MR imaging uses no ionizing radiation and can therefore be repeated without increasing the patient radiation burden. These properties make MRI an excellent candidate for image guidance. Therefore, the integration of an MRI in a radiotherapy system has been an area of interest and recently, treatment machines combining a radiation source with an MRI system have been developed

and are clinically used. In our department, the Unity MR-linac (Elekta AB, Stockholm, Sweden) ^{91,92} has been installed and clinical treatments started in September 2018. At the time of completion of this thesis, a total of 270 plans have been irradiated at the Unity MR-linac in our department (170 prostate, 42 rectum and 56 oligo metastases).

The Elekta Unity combines a linear accelerator with a 1.5 T MRI scanner (Philips Medical Systems, Best, the Netherlands), and is equipped with an EPID (XRD 1642 AP, Perkin Elmer Optoelectronics, Wiesbaden, Germany) mounted on a rotating ring gantry, opposite to the 7 MV flattening filter free (FFF) accelerator head, allowing for simultaneous beam irradiation, EPID acquisition and MR imaging ⁹³. The source-to-isocenter distance is 143.5 cm, and the source-to-detector distance (SDD) is 265.3 cm, resulting in a magnification factor of 1.84 (**Figure 1**). The central region of the cryostat is designed free of gradient coils and shimming hardware, allowing for minimal and homogenous attenuation of the beam by the cryostat. The dimension of this free-of-coils region determines the size of homogeneously attenuated beams received by the EPID, allowing for a maximum field size at the isocenter of $X=\pm 11$ cm and $Y=\pm 4.8$ cm. Note that the EPID was included in the system for the purpose of machine QA and not for patient imaging or portal dosimetry. It lies in a non-centered position with respect to the beam axis. As a result, beams can only be completely captured if their field size at isocenter is smaller than $X=\pm 11$ cm, $Y=[-11, +8]$ cm, completely encompassing the aforementioned region of homogeneous attenuation.

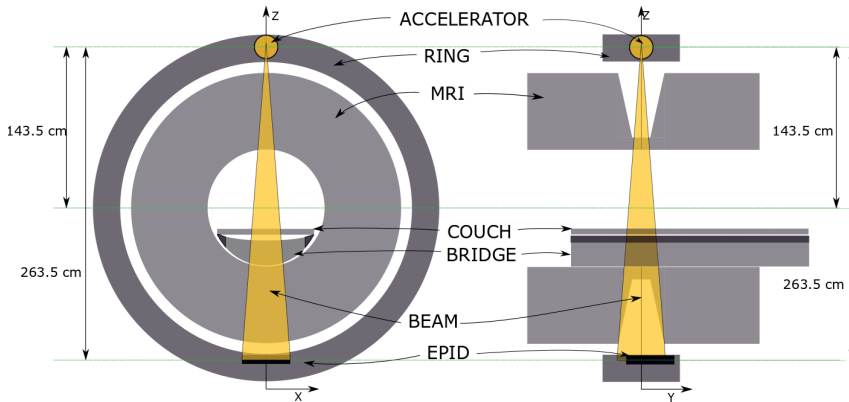


Figure 1.1: Schematic drawing of the Unity MR-linac cross sections. The EPID (black rectangle) is positioned behind the MRI housing, rotating on a ring gantry. Moreover, in the Y direction, the beam center is not aligned with the center of the panel, so parts of large fields cannot be captured.

Moreover, the EPID frame is divided into a ‘central’ region receiving un-attenuated signal and an ‘outer’ region receiving signal with extra attenuation and scatter due to exceeding the free-coils region. Since the detector is displaced 5.7 cm in the cranial direction with respect to the beam axis, fields exceeding 8.1 cm in the caudal direction at isocenter plane cannot be entirely acquired by the EPID and parts of the beam fall outside the panel (**Figure 2**).

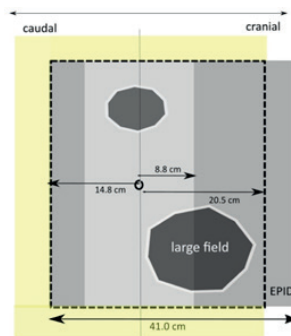


Figure 1.2: Schematic drawing of the EPID and a maximum irradiated square field arriving to the panel (yellow). Beams at the level of the EPID are received in a central unattenuated region (light grey) and in an outer attenuated region (dark grey). In the

context of this thesis, a field is considered 'large' if the corresponding acquired EPID image contains signal in the outer region. The dashed black rectangle represents the cropped EPID image used for dose reconstruction.

Unlike in conventional linacs, the Unity couch and bridge use high density materials. The complexity of their shape (darker gray in bridge structure) has to be taken into account in the TPS.

Adaptive radiotherapy (ART) strategies in MRI-guided radiotherapy (MRIGRT) aim to optimize the delivered dose distribution to the daily anatomy. In the Unity MR-linac, daily adaptation to patient position variations is not done by couch translations but by online re-planning. A reference plan is created using the planning CT and for each fraction an MRI scan is made prior to treatment to adjust the delivery to the daily anatomy/position. For that purpose, two strategies are available: the virtual couch shift (or 'adapt to position') workflow is a shift of the treatment plan to compensate for set-up deviations only. Alternatively, 'adapt to shape' is a re-contouring strategy not only to correct for positional shifts, but also changes in the shape of the anatomy⁹⁴⁻⁹⁶. More complex techniques that at this moment are not clinically adopted, require full re-optimization of the plan to account for all anatomical and setup changes. This translates into daily adaptations, which bring high flexibility and adaptability to improve treatments, but it puts high demands the on-line imaging modalities and the timescale on which a full plan must be adapted or even created and approved.

1.7. QA on the Unity MR-linac

Due to the complexity of the Unity MR-linac workflows and the little experience all centers have with it, independent dosimetric verification is highly desirable. The daily adaptation of the treatment plan to the actual anatomy force us to revisit existing concepts of patient specific QA.

- pre-treatment QA: corresponds to the verification of the reference plan. The value of such a verification is limited, as this plan will not actually be irradiated. Its main use is to test for transfer errors, the validity of TPS dose calculation and the deliverability of the treatment plan.
- online sanity check of the adapted plan: pre-treatment evaluation of the adapted plan. This can be performed using an independent dose recalculation in a separate TPS or with a sanity checks of the treatment plan data. The goal is to prevent gross errors in dose calculation or data transfer.
- QA of the adapted plan: is a dosimetric verification of the daily adapted plan. This can only be performed post-treatment, as there is no opportunity for delivery to a phantom geometry between plan creation and patient delivery. Its main use is to test for transfer errors and the validity of TPS dose calculation.
- in-vivo QA of the adapted plan: in-vivo dosimetric verification of the delivered adapted plan using measurements acquired during treatment. It verifies the actual delivery on the geometry of the patient. Besides transfer errors and TPS dose calculation, it can potentially detect all possible deviations between planning and delivery, as it is an independent end-to-end check. It would be most straightforward to analyze the result after treatment delivery. However, certain in-vivo tools like EPID dosimetry have the potential for real-time in-vivo QA, with the possibility of dosimetric QA for trailing and gating techniques and to interrupt the treatment machine upon gross error detection.

Currently, at the Netherlands Cancer Institute – Antoni van Leeuwenhoek, pre-treatment QA of the reference plans and QA of the adapted plans is performed using the OCTAVIUS 4D MRI system (PTW, Freiburg, Germany). Other centers use similar devices such as Delta4 Phantom+ MR (Scandidos, Uppsala, Sweden). The use of such devices for dosimetric verification of Unity MR-linac treatments is time-consuming⁹⁷⁻¹⁰⁰. As a result, in most clinics dosimetric verification of the daily adapted plans is limited to a few fractions only. Furthermore, in our institute a fast sanity check has been developed, which is applied for each adapted plan¹⁰¹. To our knowledge, all users of

the Unity MR-linac apply pre-treatment sanity checks or independent dose calculations to all adapted treatment fractions.

A new element in the Unity MR-linac treatment chain compared to conventional workflows, is the use of MRI for treatment planning by transformation of the daily MRI into a synthetic CT¹⁰²⁻¹⁰⁴. This presents a new element in the radiotherapy chain, of which no large-scale clinical experience is present yet, and which is not verifiable using log file-based approaches. This is one of the motivations for the use of EPID dosimetry as a complementary method to perform an independent end-to-end check of the whole chain. Errors related to data transfer, MLC calibration and dose calculation¹⁰⁵ can be caught in pre-treatment QA or QA of the adapted plan. Additionally, errors in patient set-up and synthetic CT creation can be detected using *in-vivo* portal dosimetry.

1.8. 3D in-vivo EPID for the Unity MR-linac: the back-projection algorithm

The EPID in the Unity MR-linac is positioned on the outside of the cryostat, which means that beams arrive to the panel after traversing the patient, but also after traversing the cryostat twice. The panel therefore receives the beam signal with an extra component of scatter and attenuation that does not correspond to what the patient received, as opposed to a conventional linac (**Figure 3**).

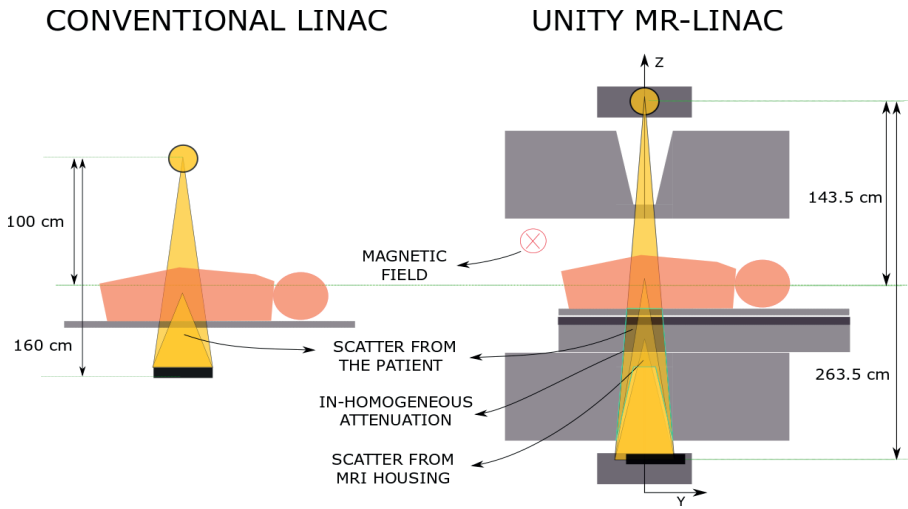


Figure 1.3: Schematic drawing of the conventional linac (left) and the Unity MR-linac (right) treatment delivery cross-sections. In conventional linacs, the EPID (black rectangle) is positioned behind the patient and the determination of the primary portal dose requires the modeling of the scatter from the patient towards the EPID. In the Unity MR-linac, the EPID lies behind the MRI housing, on the ring gantry. An aperture around the cryostat allows for minimum attenuation of the beam entering the bore, but due to divergence, this aperture is insufficient on the exit side, where the beam is larger and travels through this extra source of scatter and in-homogeneous attenuation. This complicates the determination of the primary portal dose as input for the back-projection algorithm.

The main task when adapting portal dosimetry for the Unity MR-linac is to develop models to describe the effects of the extra scatter and attenuation on the portal dose, i.e., to obtain the primary portal dose that would be arriving to the panel if the MRI were not present. New steps were added to the algorithm to account for these effects, the changes in the sensitivity of the panel due its position with respect to the beam, and a gantry angle dependent dose response. Furthermore, adjustments were made to account for the new system characteristics (source to isocenter distance, source to detector distance, EPID position with respect to beam axes, etc.).

In the Unity MR-linac, the Lorentz force produced by the constant 1.5 T magnetic field deflects the paths of moving electrons, thus redistributing the absorbed dose. A remarkable phenomenon of the B-field is the electron return effect (ERE), caused by secondary electrons that exit the patient being directed back into it, increasing the surface dose. The presence of the B-field potentially complicates a MR-linac portal dosimetry method in two ways. First, there is the influence of the B-field on the panel and second, the dose redistribution due to the B-field might have to be taken into account in the back-projection of dose.

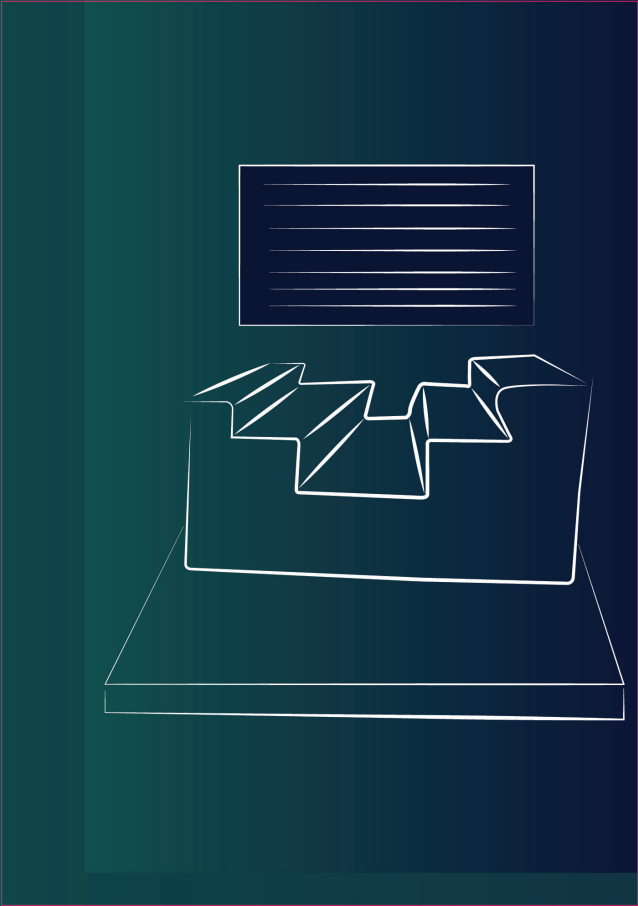
1.9. Thesis Objectives

The aim of this thesis was to extend the existing portal dosimetry method, routinely applied in the clinic for *in vivo* verification of all radiotherapy treatments, to the Unity MRI-linac system, and to provide experimental evidence that both pre-treatment and *in-vivo* 3D portal dosimetry are feasible for the Elekta Unity MR-linac.

1.10. Thesis Outline

The work presented in this thesis is organized as follows. **Chapter 2** describes the physics and practical issues to account for the extra scatter and attenuation received by the panel, as well as changes in photon energy spectrum when the beam traversed a mock-up of the MRI scanner. A characterization of the EPID panel in the Unity MR-linac was performed in **Chapter 3**. The purpose of this study was to validate the feasibility of using the panel as a dosimeter. A collection of EPID and ionization chamber (IC) dose measurements were performed and compared to similar measurements for conventional linacs. **Chapter 4** describes a proof of concept of the adapted back-projection algorithm for 2D dose reconstruction for three cardinal

gantry angles. The results were compared to measurements using a 2D IC array. **Chapter 5** presents the first clinical pre-treatment and *in-vivo* verification results of patient treatments at the MR-linac, comparing 3D EPID back-projected and planned dose distributions. In **Chapter 6**, the use of a deep learning method to correct EPID image distortions due to beam attenuation and scatter, allowing for the use of the entire EPID image for dose reconstruction. **Chapter 7** provides a general discussion, a future perspective and conclusions on the research performed regarding EPID dosimetry for the Unity MR-linac.



2.

A BACK-PROJECTION ALGORITHM IN THE PRESENCE OF AN EXTRA ATTENUATING MEDIUM: TOWARDS EPID DOSIMETRY FOR THE MR-LINAC

**I Torres-Xirau
I Olaciregui-Ruiz
R A Rozendaal
P González
B J Mijnheer
J-J Sonke
U A van der Heide
A Mans**

Department of Radiation Oncology,
The Netherlands Cancer Institute–Antoni van Leeuwenhoek Hospital,
Plesmanlaan 121, 1066 CX Amsterdam, The Netherlands

*Physics in Medicine & Biology, Volume 62, Number 15
Published 17 July 2017 • © 2017 Institute of Physics and Engineering in Medicine*

Abstract

In external beam radiotherapy, Electronic Portal Imaging Devices (EPIDs) are frequently used for pre-treatment and for *in vivo* dose verification. Currently, various MR-guided radiotherapy systems are being developed and clinically implemented. Independent dosimetric verification is highly desirable. For this purpose, we adapted our EPID-based dose verification system for use with the MR-Linac combination developed by Elekta in cooperation with UMC Utrecht and Philips.

In this study we extended our back-projection method to cope with the presence of an extra attenuating medium between the patient and the EPID. Experiments were performed at a conventional linac, using an aluminum mock-up of the MRI scanner housing between the phantom and the EPID. For a 10 cm square field, the attenuation by the mock-up was 72%, while 16% of the remaining EPID signal resulted from scattered radiation.

58 IMRT fields were delivered to a 20 cm slab phantom with and without the mock-up. EPID reconstructed dose distributions were compared to planned dose distributions using the γ -evaluation method (global, 3%, 3mm). In our adapted back-projection algorithm the averaged γ_{mean} was 0.27 ± 0.06 , while in the conventional was 0.28 ± 0.06 . Dose profiles of several square fields reconstructed with our adapted algorithm showed excellent agreement when compared to TPS.

Keywords: EPID dosimetry, MR-Linac, patient-specific, pre-treatment, *in vivo*, verification, IMRT

2.1. Introduction

Image-guided radiotherapy strives to correct for tumor misalignments derived from setup error, posture change, organ motion, etc., which may otherwise lead to suboptimal treatments. However, deformation and anatomical changes related to treatment response are typically not included in the regular IGRT workflow. Moreover, the in-room image quality is not always sufficient to visualize the tumor and relevant organs-at-risk. Hence, several groups are currently investigating the potential of radiotherapy treatment systems with integrated MR imaging modality. One example is the MRIdian System (ViewRay, Inc., Oakwood Village, OH), which integrates three Cobalt-60 heads with a 0.35-T split MRI system¹⁰⁶. The Linac-MR (Cross Cancer Institute, Edmonton AB, Canada) consists of an isocentrically rotating 6 MV linac with a biplanar 0.5-T MRI in the transverse plane allowing perpendicular and parallel irradiation to the magnetic field^{107,108}. The Australian MRI-Linac system connects a specifically designed 1-T open-bore MRI with a 6-MV linac¹⁰⁹. The MRI-linac program investigated by Siemens places a 6MV linac in a ring around a conventional MRI magnet¹¹⁰. Another initiative couples a 1.5-T, diagnostic quality, magnetic resonance imaging with a linear accelerator (Elekta AB, Stockholm, Sweden in cooperation with UMC Utrecht, The Netherlands and Philips, Best, The Netherlands)⁹². When combined with fast (re)contouring and (re)planning software, MRI-based online adaptive strategies are expected to become feasible⁹⁴. The Elekta MR-Linac is currently being installed in our institute.

The high complexity of online treatment adaptation makes independent dosimetric verification in the MR-Linac system highly desirable. Alternative quality assurance techniques involving the use of the linac log files and MRI 3D patient anatomy could allow identification of potential errors in data transfer, dose delivery, patient set-up, and

changes in patient anatomy, but not in dose calculation or MLC calibration¹⁰⁵ and not in real-time. The aim of transit EPID dosimetry at the MR-Linac is to verify the delivered 3D dose to the patient, hence providing an independent real-time verification of the entire treatment chain.

Several studies of dose-response characteristics have shown that a-Si EPIDs are suitable for dose verification^{111, 112, 113, 114, 115}. It was demonstrated⁹³ in addition that the portal imager integrated in the MR-Linac is able to acquire EPID images simultaneously to MRI imaging. Our back-projection algorithm has been described previously in detail^{70, 58} and is used to perform *in vivo* EPID dosimetry routinely for almost all IMRT and VMAT as well as 3D conformal radiotherapy treatments in our clinic since January 2008⁹⁰.

The geometry of the MR-Linac poses several challenges for EPID based dosimetry:

- The presence of the MRI housing between the patient and the EPID serves as a non-uniform attenuating medium and as a source of scattered radiation. Furthermore, it alters the photon energy spectrum of the beam.
- The 1.5T magnetic field affects the dose deposition in the patient (or phantom)^{91, 117}
- The small magnetic field at the EPID location possibly influences the dose-response characteristics of the EPID⁹³.

As a first step towards portal dosimetry in the MR-Linac, the purpose of this study was to correct for the scattering and attenuating effects in the EPID images caused by a step-shaped extra attenuating medium mimicking the MRI housing, and to back-project the corrected portal dose images into the patient's geometry.

The use of such an MRI scanner mock-up at a conventional linac is

an excellent opportunity to investigate the first of the aforementioned challenges separately, in a controlled fashion, without the need for solving the other challenges simultaneously. The influence of the magnetic field on the dose delivery both in the patient/phantom inside the bore of the MR-Linac and at the EPID level is beyond the scope of this study, but will be subject of future work.

2.2. Materials and Methods

2.2.1 Conventional back-projection algorithm

In summary, our in-house technique^{58,70} requires seven steps to reconstruct the dose in the phantom or patient from the EPID images acquired during treatment. These seven steps account for:

- i. Pixel sensitivity matrix (*S_{ij}* Matrix) which corrects for the variation in individual pixel sensitivity and in the off-axis differential photon energy⁴⁶.
- ii. Dose response of the EPID.
- iii. Lateral scatter within the EPID.
- iv. Scatter from the phantom or patient to the EPID.
- v. Attenuation of the beam by the phantom or patient.
- vi. Scatter within the phantom or patient.
- vii. Build-up effects.

In the conventional algorithm, the dose measured at the EPID level is determined after step 3.

2.2.2 Adapted back-projection algorithm

In the MR-Linac, before reaching the EPID, the

beam is affected by the presence of the MRI scanner. A sketch of the geometry of the conventional linac and the MR-Linac is given in **Figure 2.1**. The MRI housing acts as the main source of scatter in portal images, attenuates the beam and modifies its photon energy spectrum. In this work the measured portal dose behind the MRI scanner, PD_{ij}^{MRI} is corrected for the aforementioned effects, determining $PD_{ij}^{MRI,corrected}$.

In other words, $PD_{ij}^{MRI,corrected}$ estimates what would be the dose measured at the EPID level in the absence of the MRI housing, taking as input images that have been measured behind the the MRI housing.

The index pair ij refers to a pixel of the EPID at position (i,j) .

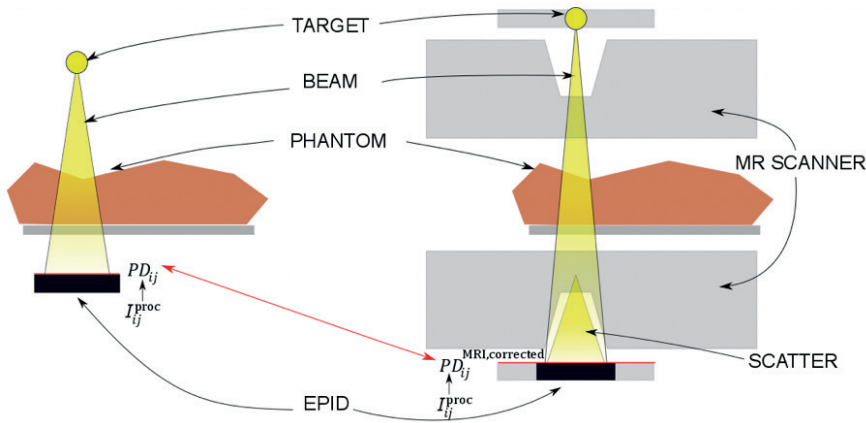


Figure 2.1: Cross section of the conventional Linac (left) and the MR-Linac (right) geometry. After the portal images I_{ij}^{proc} are processed, the portal dose PD_{ij} on the left corresponds to the portal dose corrected $PD_{ij}^{MRI,corrected}$ on the right and the back-projection is continued as in the conventional method.

To achieve this, the 3rd step of our conventional algorithm (portal dose determination) has been expanded to:

- correction for lateral scatter within the EPID (step 3 in conventional algorithm), obtaining the portal dose behind the MR-Linac, PD_{ij}^{MRI} ,
- subtraction of that part of the portal dose due to scatter from the MRI housing to the EPID, $Sc_{ij}^{MRI \rightarrow EPID}$, obtaining $PD_{ij}^{MRI,ScatCorr}$,
- correction for the extra attenuation in $PD_{ij}^{MRI,ScatCorr}$ and changes in energy spectrum due to the MRI housing, obtaining $PD_{ij}^{MRI,ScatCorr}$.

After the effects caused by the MRI scanner on the EPID images are corrected, the resulting the portal dose MRI-corrected, $PD_{ij}^{MRI,Corrected}$, is used in the remaining steps of the algorithm, which is identical to the conventional version.

In what follows, two specific configurations are used:

- MRI geometry: in the MR-Linac the beam always traverses the MRI scanner. I_{ij}^{MRI} images can be obtained with patient $I_{ij}^{MRI,patient}$, or without patient $I_{ij}^{MRI,open}$. Along the description of the fitting algorithm and the commissioning of the model, “open” or “patient” are specified, unless the expression is valid for both set-ups.
- Empty geometry: in this case the MRI scanner, patient and couch are not present. Although this set-up is unrealistic in the clinical/actual set-up, the current calibration procedure of our transmission-based algorithm requires a set of I_{ij}^{empty} images to determine the parameters of the MRI \rightarrow EPID scatter kernel.

A. Subtraction of radiation scattered from the MRI housing to the EPID

The scattered radiation from the MRI scanner to the EPID is treated in the same way as the scattered radiation from the patient reaching the EPID in our conventional algorithm because of the similarity of these cases. The scatter is modeled as a convolution between the portal dose image and a scatter kernel, and the kernel parameters are determined by a fitting process described below.

The portal dose behind the MRI scanner PD_{ij}^{MRI} , includes the component $Sc_{ij}^{MRI \rightarrow EPID}$ due to scatter from the MRI scanner to the EPID.

$$PD_{ij}^{MRI} = PD_{ij}^{MRI, ScatCorr} + Sc_{ij}^{MRI \rightarrow EPID}, \quad (1)$$

where $PD_{ij}^{MRI, ScatCorr}$ represents the portal dose of radiation reaching the EPID as if the scatter from the MRI scanner was not present.

The portal dose in the conventional algorithm (i.e., after step 3) PD_{ij} , corresponds to a processed EPID image containing dose information and is calculated as:

$$PD_{ij} = I_{ij}^{proc} \cdot S_{ij} \cdot Dr \otimes^{-1} K1_{\square} \otimes K2_{\square} \quad (2)$$

where I_{ij}^{proc} is the time-integrated EPID image processed for the dark field, flood field and bad pixels¹¹⁹. S_{ij} is the pixel sensitivity matrix, Dr is the dose response of the EPID, and $K1_{\square}$ and $K2_{\square}$ are kernels correcting for the lateral scatter within the EPID. $K1_{\square}$ accounts for the lateral scatter within the EPID based on a central axis parametric fit, and $K2_{\square}$ is a blurring kernel such that the EPID images

agree with the off-axis data from the ionization chamber, affecting mainly the penumbra region ⁷⁰. The aim of the convolution with $K2$ is to match better the penumbras while maintaining the on-axis agreement obtained by $K1$.

Note that fluence is not determined in our semi-empirical algorithm.

Convolution and deconvolution were performed in frequency domain using the fast Fourier transform in two dimensions and the calculation time to process the EPID image after acquisition was of the order of 10 ms.

Unlike in the conventional linac, in the MR-Linac, a large scatter contribution from the MRI housing to the EPID exists, together with a step-shaped attenuation and differences in photon beam energy spectra. Therefore, the EPID responds differently behind the MRI scanner, and both PD_{ij}^{empty} and PD_{ij}^{MRI} portal dose images require separate calibration data-sets and have to be calculated with different parameters:

$$PD_{ij}^{MRI} = I_{ij}^{MRI} \cdot S_{ij}^{MRI} \cdot Dr_{ij}^{MRI} \otimes^{-1} K1_{ij}^{MRI} \otimes K2_{ij}^{MRI} \quad (3)$$

$$PD_{ij}^{empty} = I_{ij}^{empty} \cdot S_{ij}^{empty} \cdot Dr_{ij}^{empty} \otimes^{-1} K1_{ij}^{empty} \otimes K2_{ij}^{empty} \quad (4)$$

The transmission of the beam through the MRI scanner is now defined as the ratio between “MRI-open” (3) and “empty” (4) portal dose images

$$T_{ij}^{total,MRI} = \frac{PD_{ij}^{MRI,open}}{PD_{ij}^{empty}} \quad (5)$$

and will be called MRI total transmission. By using (1) it can be

separated into a primary and a scatter component,

$$T_{ij}^{total,MRI} = T_{ij}^{primary,MRI} + \frac{Sc_{ij}^{MRI \rightarrow EPID}}{PD_{ij}^{empty}} \quad (6)$$

where $T_{ij}^{primary,MRI}$ denotes the transmission of the primary photons measured with the EPID.

The scatter from the MRI to the EPID and consequently the total transmission $T_{ij}^{total,MRI}$ in (6) are field size dependent¹²⁰, while the primary transmission $T_{ij}^{primary,MRI}$ is by definition field size independent. To determine the scatter component to the portal dose, the total transmission $T_{ij}^{total,MRI}$, is experimentally determined with (5) as a function of field size fs , by irradiating the EPID with and without the mock-up of the MRI scanner with square fields of different sizes. In the limit of zero field size, the total transmission $T_{ij}^{total,MRI}$ equals the primary transmission $T_{ij}^{primary,MRI}$ as the scatter from the MRI scanner reaching the EPID tends to zero. On-axis values of the total transmission, $\langle T_{ij}^{total,MRI} \rangle_{cROI}$, are plotted as a function of field area, fs^2 , and the limit to zero field area is calculated by parametrizing the curve of $\langle T_{ij}^{total,MRI} \rangle_{cROI}$. The brackets $\langle \rangle_{cROI}$ represent the average over a small central region of interest (cROI) of the EPID at the central axis.

$$\langle T_{ij}^{primary,MRI} \rangle_{cROI} \approx \lim_{fs \rightarrow 0} [\langle T_{ij}^{total,MRI}(fs^2) \rangle_{cROI}] \quad (7)$$

Since at small air-gaps the transmission is no longer linearly related with field area¹²⁰, a second-order polynomial was used to parametrize the $\langle T_{ij}^{total,MRI} \rangle_{cROI}$ for the 15cm air-gap used in our set-up (see section 2.4), and the constant $\langle T_{ij}^{primary,MRI} \rangle_{cROI}$ is obtained using (7).

The scatter from the MRI scanner to the EPID is modeled in the portal

dose as a convolution of the MRI- open portal dose image with a scatter kernel $K_{ij}^{MRI \rightarrow EPID}$,

$$S_{C_{ij}}^{MRI \rightarrow EPID} = PD_{ij}^{MRI,open} \otimes K_{ij}^{MRI \rightarrow EPID} \quad (8)$$

Based on the iterative approach to determine the scatter from the patient to the EPID suggested in^{121, 122}, we investigated the use of a similar iterative approach using the scatter corrected MRI-open portal dose $PD_{ij}^{MRI,open,ScatCorr}$ in (8) instead of the MRI-open portal dose $PD_{ij}^{MRI,open}$. However, preliminary results showed that the MRI-open portal dose itself appeared to be a good approximation, as the fitting results after 6 iterations improved only 0.025% the Euclidean distance between $\langle T_{ij}^{primary,MRI} \rangle_{cROI}$ and $\langle T_{ij}^{primary,MRI}(fS; \sigma_{MRI}^2, c_{MRI}) \rangle_{cROI}$. In this work, a gaussian filter was used as a scatter kernel,

$$K_{ij}^{MRI \rightarrow EPID} = \frac{c_{MRI}}{2\pi\sigma_{MRI}^2} \exp\left(-\frac{r_{ij}^2}{2\sigma_{MRI}^2}\right), \quad (9)$$

where r_{ij} is the distance of a pixel ij from the central axis.

In order to determine the parameters σ_{MRI}^2 and c_{MRI} , the primary transmission $\langle T_{ij}^{primary,MRI}(fS; \sigma_{MRI}^2, c_{MRI}) \rangle_{cROI}$, is calculated for different field sizes using (6) (and (8), (9) to introduce σ_{MRI}^2 and c_{MRI}) and fitted for all field sizes to the zero-field-size limit of the total transmission calculated in (7)), $\langle T_{ij}^{primary,MRI} \rangle_{cROI}$ by:

$$\min_{\sigma_{MRI}^2, c_{MRI}} \left(\langle T_{ij}^{primary,MRI} \rangle_{cROI} - \langle T_{ij}^{primary,MRI}(fS; \sigma_{MRI}^2, c_{MRI}) \rangle_{cROI} \right) \quad (10)$$

where $\min()$ is a minimization function, and the aim is to fulfill the field size independence of the $\langle T_{ij}^{primary,MRI} \rangle_{cROI}$ with the correct parameters

determination.

B. Correction for the MRI housing attenuation

An experimentally determined primary transmission 2D map is applied to the scatter corrected MRI-open image, $PD_{ij}^{MRI,open,ScatCorr}$, to account for the attenuation and beam hardening in the MRI housing.

This primary transmission map is defined as the ratio between the portal dose MRI-open image corrected or the scatter $PD_{ij}^{MRI,open,ScatCorr}$, and an empty portal dose image PD_{ij}^{empty} for a large square field ($26 \times 26 \text{ cm}^2$):

$$Tmap_{ij} = \frac{PD_{ij}^{MRI,open,26 \times 26} - Sc_{ij}^{MRI \rightarrow EPID}}{PD_{ij}^{empty,26 \times 26}} \quad (11)$$

The final portal dose corrected for the effects of the MRI scanner

$PD_{ij}^{MRI,corrected}$ can be expressed as:

$$PD_{ij}^{MRI,Corrected} = \frac{PD_{ij}^{MRI,ScatCorr}}{Tmap_{ij}} \quad (12)$$

2.2.3 Commissioning data

To support the additional two steps in our dose reconstruction engine, new measurements had to be added to the regular set of commissioning data, which is summarized in¹²³. Also, the reconstruction dose engine had to be adapted in the commissioning and in the verification software. The required complete new set of commissioning data consists of EPID images, water tank measurements and reference ionization chamber values for each configuration (“MRI-phantom”, “MRI-open” and “empty”) irradiated with square fields of increasing size (2×2 - 26×26

cm²) and is summarized in **Table 2.1**.

Commissioning measurements for the “empty” configuration were acquired on a regular 6 MV photon beam of an SL20i linear accelerator with flattening filter, without the aluminum structure in place, while the set-up for the rest of the measurements included the mock-up between isocenter and EPID, and a slab phantom only when indicated.

Table 2.1: Measurements required for commissioning of the model. The required extra measurement series (with respect to the conventional model) that are used for the determination of the scatter from the MRI and the attenuation map of our adapted method, are marked with (*). The commissioning measurements that determine the rest of the parameters are acquired similarly to as in the conventional method, considering the “MR” as the standard configuration in the MR-Linac.

Measurement	Configuration	Comment	Equipment	Phantom (cm ³)	Field Size (cm ²)
1. S_{ij} matrix	Empty*	To measure the relative sensitivity over the entire EPID	a) Ionization chamber in a mini-phantom in an empty water tank b) 2 EPID images		26x26
2. Field size series	Empty*	Measure and acquire at the EPID level (160 cm SSD)	a) Ionization chamber in a mini-phantom b) EPID images		Series 2x2- 20x20

3. S_{ij} matrix	MR-open	To measure the relative sensitivity over the entire EPID behind the MRI	a) Ionization chamber in a mini-phantom in an empty water tank b) 2 EPID images		26x26
4. Field size series	MR-open	Measure and acquire at the EPID level (160 cm SSD)	a) Ionization chamber in a mini-phantom b) EPID images		Series 2x2- 20x20
5. Field size series	MR-phantom	Constant phantom thickness, varying field size	a) Ionization chamber at isocenter in slab phantom b) EPID images	30x30x20 slab	Series 2x2- 20x20
6. Thickness series	MR-phantom	Constant field size, varying phantom thickness	a) Ionization chamber at isocenter in slab phantom b) EPID images	Series 30x30x4-40	10x10
7. Build up	MR-phantom	Constant field size, constant phantom thickness	Ionization chamber in a slab phantom at different depths	30x30x20	10x10

2.2.4 MRI scanner surrogate

To quantify the performance of our adapted algorithm, an experimental set-up was built in a conventional linac, consisting of an aluminum structure positioned between the phantom and the EPID, mimicking the geometry of the exit beam side of the MRI scanner. We define the axis of an EPID image parallel to the gun target direction as Y, and the axis perpendicular to it, X.

In the magnet of the MR-Linac, the central 15 cm in the Y direction is free of coils and shimming hardware in order to minimize beam attenuation and obtain homogeneous transmission. This 15 cm gap allows a maximum irradiation field of 22 cm in the cranial-caudal direction at the isocenter. However, for field sizes larger than 10 cm at the isocenter, the exit beam exceeds the 15 cm of the gap at the exit side and therefore, EPID images suffer from an extra attenuation at the edges in the Y direction as can be seen from **Figure 2.2.a,b**.

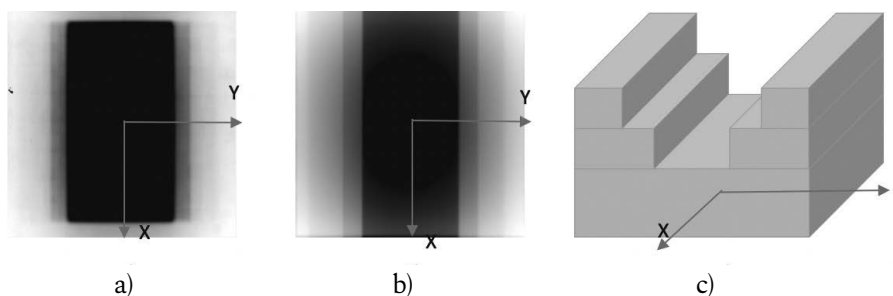


Figure 2.2: a) EPID images of a large field size acquired at the second MR-Linac prototype at the UMC Utrecht; b) EPID images of a large field size acquired at our institute with the aluminum structure; c) Schematic drawing of the aluminum structure used at our institute to mimic the effect of the MRI scanner.

To mimic this configuration at a conventional linac, an aluminum MRI-scanner mock-up was designed making use of the available information in literature. As reported^{124, 126, 93}, the irradiation beam travels through the equivalent of approximately 12 cm of aluminum

on-axis, hence an aluminum plate of 12 cm thickness at 15 cm distance from the EPID was used. Off-axis, the larger thickness of the magnet in the Y direction was mimicked by thicker aluminum blocks of 18 cm and 21 cm (**Figure 2.2.c**).

The presence of the MRI scanner between source and patient was not included in our mock-up since the effects it causes are not to be taken care of by our back-projection dosimetry model. To validate this choice, an experiment was performed with an extra structure of aluminum between the source and the isocenter. EPID images were acquired in a conventional linac with the aluminum structure between the isocenter and the EPID, both with and without 12cm extra of aluminum between the source and the isocenter. EPID readouts (normalized to the 10x10 cm² field size) were compared. For further experiments, no aluminum mock-up was used between source and isocenter.

2.2.5 Accelerator and EPID

All measurements in our institute were performed using a 6 MV photon beam of an SL20i linear accelerator with flattening filter (Elekta AB, Stockholm, Sweden), equipped with a multileaf collimator (MLC) of 80 leaves with a projected leaf width of 1 cm at the isocenter, which is located 100cm from the target. A PerkinElmer RID 1680 AL5/Elekta iViewGT a-Si EPID was used for all measurements. Images were acquired using in-house developed software^{114, 119}.

2.2.6 Square field and test field validation

To validate our method off-axis, EPID images acquired behind the phantom and the aluminum structure during the commissioning were back-projected using our adapted method into a 20 cm slab phantom for different square field sizes (2x2, 3x3, 5x5, 10x10, 15x15, 20x20 cm²).

A test field presenting a more complex geometry was included in the validation. The test field contained areas with signal coming from a single open MLC leaf (with adjacent leaves blocking radiation), another area with signal from two leaves only, and so on, resembling characteristics of an IMRT beam.

Cross-plane dose profiles and depth-dose curves were obtained and compared to the planned dose distributions and to measured curves in a water tank by an ultra-small detector: the microDiamond detector (PTW, Freiburg, Germany). 2D dose distributions reconstructed at the isocenter were compared to the planned dose distributions by γ -evaluation (global 3%, 3mm). For visual inspection, a 2D signed γ -evaluation is used in our clinic to indicate under-dosage or over-dosage when compared to the TPS.

2.2.7 IMRT plans and Treatment Planning System (TPS)

58 beams of 10 IMRT plans (5 tumor sites: lung, H&N, rectum, brain, breast) were included in this study. The plans were calculated for a step-and-shoot IMRT technique irradiating a 20 cm thick slab phantom, using 6 MV photon beams, with 2 to 7 segments per beam, with the beam angle set to 0° . Dose distributions were optimized in Pinnacle Version 9.8 (Philips Medical Systems, Eindhoven, The Netherlands). The treatments were randomly selected and their field sizes in the Y direction ranged from 7 to 17 cm. 2D dose distributions reconstructed at the isocenter were compared to the TPS dose distributions by means of γ -analysis (global 3%, 3mm) and the ROI of the γ -analysis was set to all pixels receiving more than 20% of the per-beam maximum dose.

To test the performance of our algorithm at different depths, 2D dose distributions reconstructed with our adapted algorithm were compared to the TPS for a 5-field Lung IMRT treatment on a 20 cm slab phantom by means of γ -analysis (global 3%, 3mm) at isocenter plane, and planes

5cm below and above that plane. The X and Y profiles obtained from the reconstructed dose distributions at the three depths were compared to the TPS profiles by visual inspection.

2.3 Results

2.3.1 EPID readouts with and without extra aluminum plate between source and isocenter

Figure 2.3 shows EPID output factors acquired with the aluminum mock-up between the isocenter and the EPID, both with and without a mock-up between the source and the isocenter. The curves show similar behavior, differences ranged from -3% to +3% for 3x3 cm² and 20x20 cm² fields respectively.

This indicates that scatter from the upper part of the MRI housing does not have a significant contribution in the EPID images.

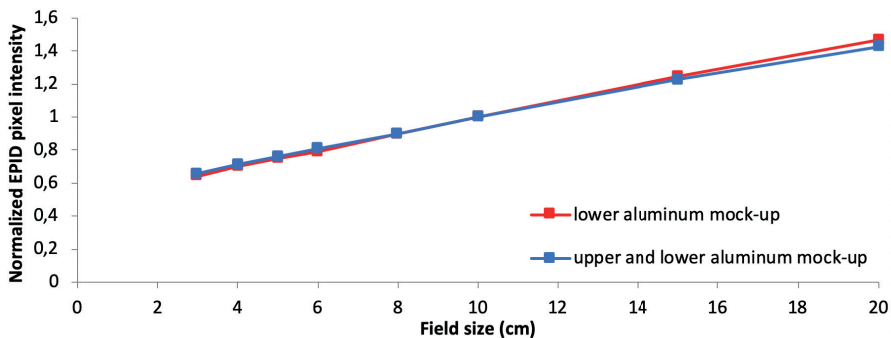


Figure 2.3: Central pixel values of EPID images for increasing square field sizes (3x3 - 20x20 cm²) normalized to the 10x10 cm² field size, acquired in a conventional linac both with the aluminum mock-up mimicking the effects of the upper and lower part of the MRI housing (blue), and only the lower part (red).

2.3.2 Magnitude of the corrections:

A quantitative description of the additional corrections applied to the portal dose measured by the EPID is reported for a 10x10 cm² field irradiating a 20 cm thick slab phantom. The scattered radiation from the aluminum mock-up reaching the EPID contributes to 16% of the measured EPID dose on-axis, which we successfully subtracted from the total portal dose using (1) as explained in section 2.2.2.A. The attenuation of the primary photons measured with the EPID as defined in (6), of the aluminum mock-up on-axis for the 6MV beam is 72%.

2.3.3 Square fields and test field validation:

In **Table 2.2** the 2-D γ -evaluation results comparing reconstructed dose distributions from back-projected EPID images acquired behind the aluminum structure to TPS dose distributions are presented for various square field sizes.

Table 2.2: Two-dimensional γ -evaluation for increasing square field sizes of a 6 MV photon beam comparing the reconstructed EPID midplane dose at 10 cm depth in a 20 cm thick polystyrene slab phantom at an SSD of 90 cm to the planned dose distribution by the TPS.

Field size (cm ²)	2x2	3x3	5x5	10x10	15x15	20x20
γ -evaluation						
γ_{mean}	0.38	0.38	0.33	0.27	0.26	0.22
$\gamma_{1\%}$	0.80	0.82	0.81	0.75	0.79	0.67
$\%_{\gamma \leq 1}$	100	100	100	100	99.9	100
$\Delta Dose_{iso}$	-0.7%	1.6%	-0.6%	0.2%	0.7%	0.8%

In **Figure 2.4.a,b**, X and Y dose profiles of square fields of different sizes from the TPS are shown respectively, together with dose profiles reconstructed from EPID images acquired behind the aluminum structure and also to dose profiles measured with a microDiamond detector. The X profile of the described test field is also shown in **Figure 2.4.c** for the microDiamond detector, the planned dose distribution, and for the EPID-derived dose distribution.

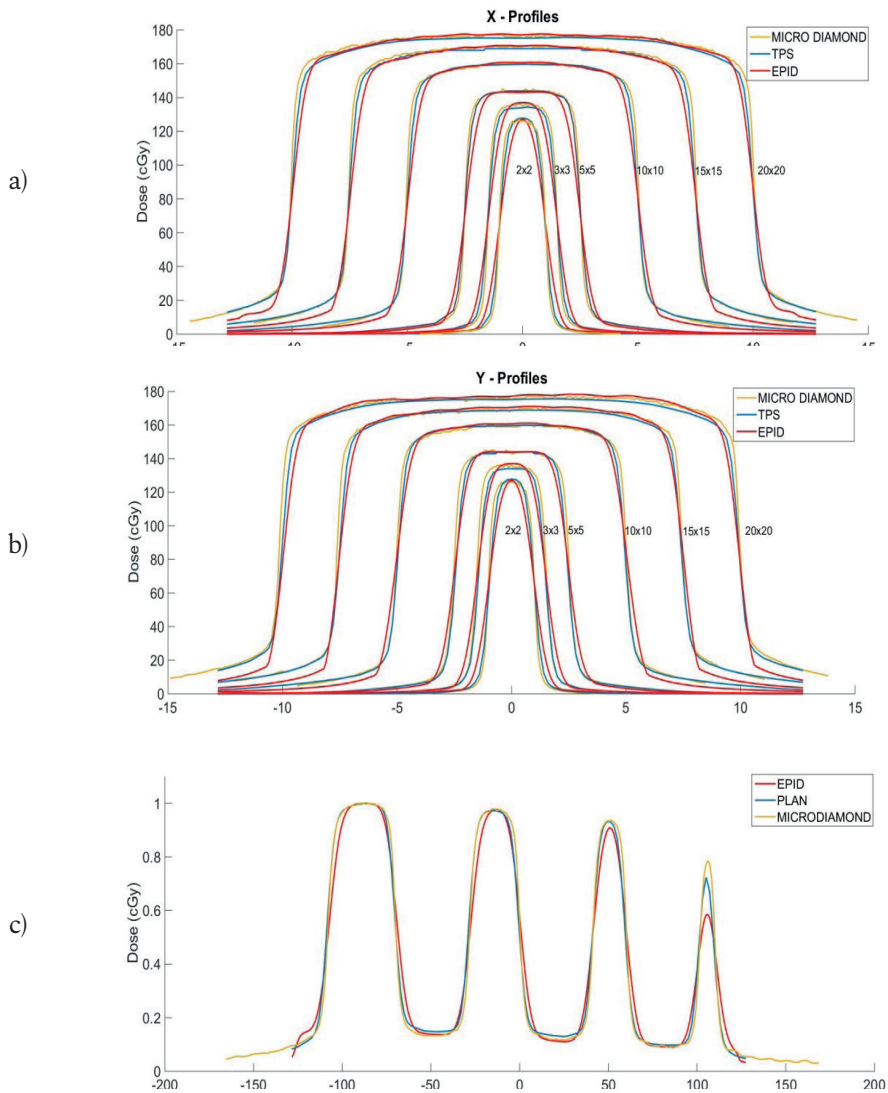


Figure 2.4: a,b) X and Y lateral profiles from the reconstructed EPID midplane dose at 10 cm depth for 6 MV photon beams of different square field sizes irradiating to a 20 cm thick slab. In blue, the X and Y profiles calculated by the treatment planning system at 10 cm depth. In yellow, measured dose profiles by a microDiamond detector in a water tank at the same depth; c) EPID, TPS and microDiamond detector curves of the lateral X profile of the described test field.

In **Figure 2.5** the depth-dose curve obtained from the EPID back-projected dose distribution is compared to TPS data and to the microDiamond detector measured curve for the 10x10 cm² square field.

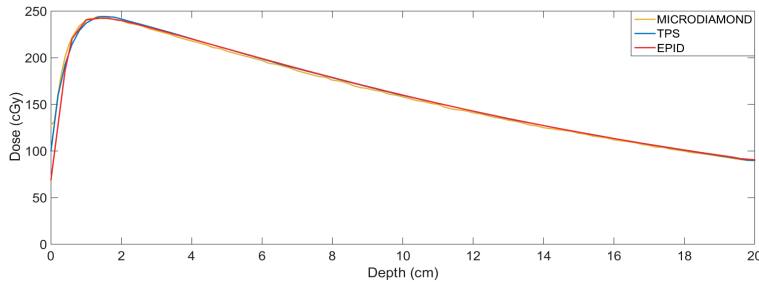


Figure 2.5: Comparison between depth-dose curves along the central beam axis through the isocenter for a 10x10 cm² field of a 6 MV photon beam irradiating a 20 cm thick slab phantom, taken from the reconstructed 3D dose distribution using EPID images behind the aluminum structure (blue), the planned TPS dose distribution (red), and the microDiamond measured curve (yellow).

When compared to the TPS, 96% of the points of the EPID curve showed deviations smaller than 2% and those points having larger deviations were situated at depths smaller than 0.4 cm and at depths larger than 19.5 cm. When compared to the microDiamond, 97% of the points of the EPID curve showed deviations smaller than 2% and those points having larger deviations were situated at depths smaller than 0.6 cm and at depths larger than 19.5 cm.

2.3.4 Reconstruction of IMRT plans:

As an example, **Table 3** presents the 2-D γ evaluation (3%, 3mm) at the isocenter plane of a 6 MV lung IMRT plan consisting of 5 beams delivered to a 20 cm thick slab phantom.

Table 2.3: 2D γ -evaluation of EPID reconstructed dose distributions compared to the TPS at the isocenter for a 5-field IMRT plan delivered to a 20 cm thick polystyrene phantom. The top row uses the conventional back-projection algorithm and the bottom row the MRI-adapted back-projection algorithm for the situation without and with the bottom aluminum structure, respectively.

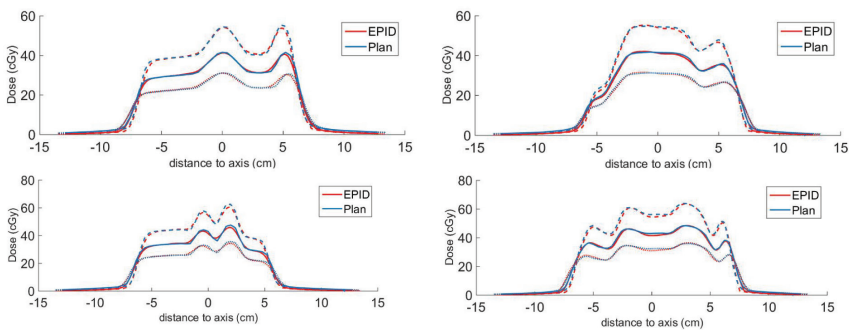
Without aluminum structure						Δ Dose isocentre
γ_{mean}	0.34	0.20	0.17	0.34	0.21	-0.5%
$\gamma_{1\%}$	0.89	0.61	0.51	0.85	0.70	
$\% \gamma_{\leq 1}$	99.7	100.0	100.0	99.7	99.8	
With bottom aluminum structure						Δ Dose isocentre
γ_{mean}	0.24	0.24	0.19	0.23	0.18	-0.6%
$\gamma_{1\%}$	0.69	1.03	0.71	0.86	0.58	
$\% \gamma_{\leq 1}$	100	98.6	99.6	99.7	100	

A 2D γ -evaluation per beam of the same treatment was performed at isocenter+5cm and isocenter-5cm with the aluminum mock-up between the phantom and the EPID and using our adapted back-projection algorithm. The γ results when compared to the TPS are presented in **Table 2.4:**

Table 2.4: 2D γ -evaluation of EPID reconstructed and planned dose distributions at 5 cm above and below the isocenter plane, for a 5-field IMRT plan delivered to a 20 cm thick polystyrene phantom.

Isoc +5cm						Δ Dose
γ_{mean}	0.26	0.24	0.24	0.25	0.21	-0.6%
$\gamma_{1\%}$	0.83	0.80	0.80	0.87	0.69	
$\% \gamma_{\leq 1}$	99.7	99.9	99.7	99.4	99.7	
Isoc -5cm						Δ Dose
γ_{mean}	0.27	0.26	0.23	0.25	0.21	-0.6%
$\gamma_{1\%}$	0.90	1.21	0.80	1.08	0.64	
$\% \gamma_{\leq 1}$	99.7	98.15	99.3	98.6	100	

X and Y profiles for the three depths (isocenter+5cm, isocenter and isocenter-5cm) are also plotted for each beam and presented in **Figure 2.6**.



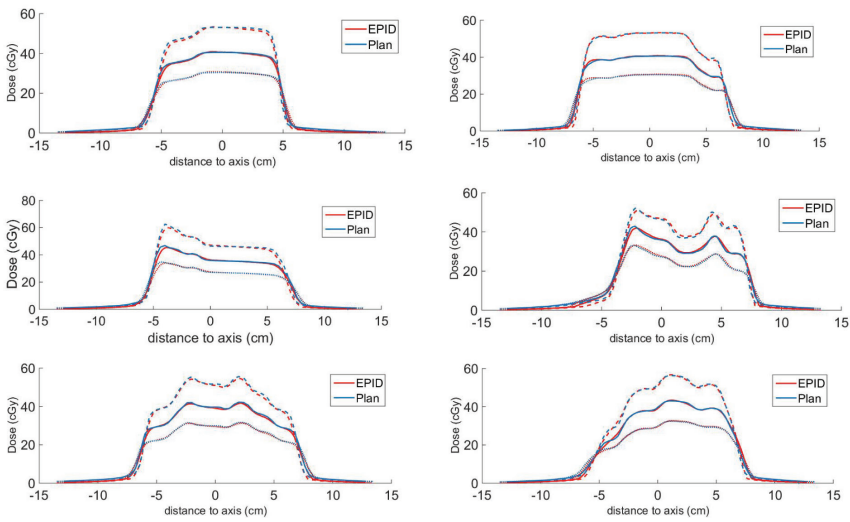


Figure 2.6: X-profiles are plotted in left column and Y-profiles in right column for each field (A-E). In dotted line the curve at isocenter-5cm, in solid the isocenter curve, and in dashed the isocenter+5cm curve.

In **Table 2.5** the γ parameters of the 2D γ -evaluation at the isocenter averaged over 58 IMRT fields are reported.

Table 2.5: γ -evaluation results (3%,3mm) averaged over the 58 IMRT fields. Our conventional algorithm was used to back-project portal images acquired without the aluminum structure (top) and our adapted algorithm to correct and back-project portal images acquired with the aluminum in place (bottom).

	γ_{mean}	$\gamma_{1\%}$	$\% \gamma_{\leq 1}$	$\Delta Dose_{iso}$ (cGy)
No-aluminum	0.28 ± 0.06	0.83 ± 0.15	99.5 ± 0.97	-0.80 ± 0.65
With aluminum	0.27 ± 0.06	0.91 ± 0.32	99.0 ± 1.3	-0.16 ± 0.90

2.4 Discussion

We have adapted our portal dosimetry algorithm to account for the presence of an MRI housing mock-up between patient and EPID in an MR-Linac system, that attenuates 72% and increases the scatter contribution of the EPID signal to 16%. The two new steps added to the conventional back-projection algorithm successfully corrected the portal dose images for the non-uniform attenuation between phantom (or patient) and EPID, and converted to the situation as if the MRI housing mock-up was not present. A complete back-projection of EPID images through the MRI mock-up was achieved, proving that the presence of an MRI scanner between patient and EPID in the MR-Linac should not become an impediment for the implementation of EPID dosimetry in the MR-Linac. The results presented in **Table 5** show that the performance of the adapted algorithm is similar to the conventional algorithm.

The accelerator where our experiments were performed at is equipped with an MLCi2 and the width of its leafs is 1 cm when projected at the isocenter. Because the commissioning of our algorithm was performed for field sizes not smaller than $2 \times 2 \text{ cm}^2$, the agreement of our EPID reconstructed profiles is less good for smaller fields sizes, such as in the area in which a single MCL leaf is open in the test field of **Figure 4.c**, where differences between the reconstructed EPID profile and the planned profile are up to 20%. This might yield to inaccuracies for highly modulated clinical fields, since results worsen the more, we differ from commissioning conditions. A commissioning including field sizes of $1 \times 1 \text{ cm}^2$ was not used because below $2 \times 2 \text{ cm}^2$, the field becomes smaller than the mini-phantom and the uncertainty in miniphantom setup increases considerably. Unwanted variations in $1 \times 1 \text{ cm}^2$ measurements may affect the results of the fit for larger field sizes, meaning that a fit to $1 \times 1 \text{ cm}^2$ data worsens the fit for larger field sizes.

Differences in linac energy, MLC design, and flattening filter between the linac where the experiments were carried out and the MR-Linac should not imply consequences in our reconstruction algorithm, since the original method has been used in our institute in linacs equipped with different MLC's, both with 6 and 10 MV and also FFF.

The scatter originated in the aluminum structure reaching the EPID is estimated via an on-axis fitting process for several field sizes, providing an accurate assessment of the scatter on axis but less precise off-axis. This is the cause of the wider penumbras in the EPID-derived profiles when compared to the TPS or microDiamond measured data. A better modelling of the scatter can only be achieved by a two-dimensional fitting procedure minimizing the distance between estimated scatter profiles and Monte Carlo simulated scatter profiles. We intend to apply this approach in the future adaptation of the algorithm for the real MR-Linac geometry. However, such Monte Carlo simulations were not performed for the aluminum mock-up.

Besides more sophisticated scatter modeling, other challenges will arise when we validate the proposed method in the real MR-Linac. The challenges for that are discussed next.

The calculations and measurements discussed in this paper were performed using a mock-up of the MR-Linac prototype geometry described by^{126, 93} and¹²⁴, which approximates the MRI housing on axis well. The actual design of the clinical MRL, however, has a smaller amount of material in the radiation beam causing less attenuation, scatter and beam hardening. The geometry of the more shielded areas (on the Y edges) has not been reported in literature and therefore the thickness of the thicker parts of our mock-up was chosen based on the values of EPID images acquired in the second MR-Linac prototype at UMC Utrecht. The reconstruction results for treatments with large field sizes (i.e. those exceeding 10 cm in the Y direction) demonstrate

that our adapted back-projection algorithm is able to reconstruct through these thicker parts.

Due to spatial constraints when mounting the aluminum mock-up between couch and EPID, for the verification of our IMRT plans the gantry was forced to be at 0° . Consequently, verification of VMAT plans could not be included in this study. However, in the actual MR-Linac and given its geometry, the beam will equally traverse the MRI scanner before hitting the EPID perpendicularly at any gantry angle. Therefore, the rotation of the gantry is not expected to alter the results of this study.

In contrast to the mock-up geometry, in the MR-Linac the beam will also traverse the MRI housing before reaching the patient. First of all, the influence of the MRI housing on the patient dose delivery will have to be taken care of in the TPS. Furthermore, the results of section 3.1 demonstrate that the scatter from the upper part of the aluminum mock-up is mostly absorbed by the lower aluminum structure, indicating that its effects on the EPID signal are limited. However, this is not relevant from the perspective of our algorithm, since empirical fits are performed to associate EPID pixel intensities to ionization chamber measurements. In other words, when an upper aluminum mock-up had been used for the commissioning of our model, similar results would have been expected. The extra the mock-up between source and isocenter was not included in the rest of the study to allow for straightforward comparison of EPID reconstructed and planned dose distributions.

The adapted method requires a set of commissioning data that includes EPID images and ionization chamber readings without the extra attenuating medium. While in this study the aluminum MR-Linac mock-up could easily be removed, the acquisition of these data in case of the MR-Linacs is less straightforward. Currently, we are

working on two approaches: the use of Monte Carlo simulations and measurements performed at an MR-Linac before the installation of the MRI scanner. Either of the two approaches are expected to provide sufficient information for a complete EPID dosimetric calibration for the MR-Linac.

2.5. Conclusion

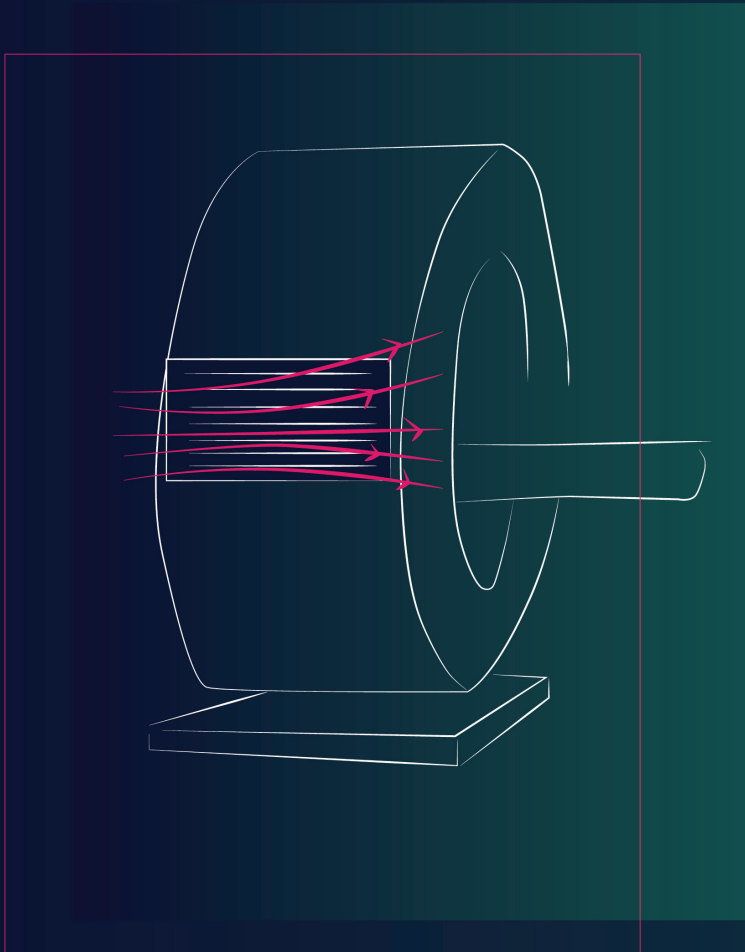
Our EPID dosimetry back projection algorithm was successfully adapted for the presence of an extra step-shaped attenuating medium between phantom (or patient) and EPID. The aluminum MRI housing mock-up attenuates the beam by 72%, and causes 16% of the remaining EPID signal to consist of an extra scatter contribution. Experiments show excellent agreement between planned and EPID reconstructed dose distributions in a phantom positioned at the isocenter. This result is an essential step towards an accurate and independent dose verification tool for the MR-Linac.

2.6. Disclosure of conflicts of interest

Support for this research was provided, in part, by Elekta AB, Stockholm, Sweden.

2.7. Acknowledgments

We would like to thank Jan Kok, Job Geuze, Jochem Kaas, Thijs Perik and Begoña Vivas for assistance with the measurements.



3.

A BACK-PROJECTION ALGORITHM IN THE PRESENCE OF AN EXTRA ATTENUATING MEDIUM: TOWARDS EPID DOSIMETRY FOR THE MR-LINAC

**I Torres-Xirau
I Olaciregui-Ruiz
R A Rozendaal
P González
B J Mijnheer
J-J Sonke
U A van der Heide
A Mans**

Department of Radiation Oncology,
The Netherlands Cancer Institute–Antoni van Leeuwenhoek Hospital,
Plesmanlaan 121, 1066 CX Amsterdam, The Netherlands

*Physics in Medicine & Biology, Volume 62, Number 15
Published 17 July 2017 • © 2017 Institute of Physics and Engineering in Medicine*

Abstract

Electronic portal imaging devices (EPIDs) are frequently used in external beam radiation therapy for dose verification purposes. The aim of this study was to investigate the dose-response characteristics of the EPID in the Unity MR-linac (Elekta AB, Stockholm, Sweden) relevant for dosimetric applications under clinical conditions. EPID images and ionization chamber measurements were used to study the effects of the magnetic field, the scatter generated in the MR housing reaching the EPID, and inhomogeneous attenuation from the MR housing. Dose linearity and dose rate dependencies were also determined.

The magnetic field strength at EPID level did not exceed 10 mT, and dose linearity and dose rate dependencies proved to be comparable to that on a conventional linac. Profiles of fields, delivered with and without the magnetic field, were indistinguishable. The EPID center had an offset of 5.6 cm in the longitudinal direction, compared to the beam central axis, meaning that large fields in this direction will partially fall outside the detector area and not be suitable for verification. Beam attenuation by the MRI scanner and the table is gantry angle dependent, presenting a minimum attenuation of 67% relative to the 90° measurement. Repeatability, observed over 2 months, was within 0.5% (1 SD).

In order to use the EPID for dosimetric applications in the MR-linac, challenges related to the EPID position, scatter from the MR housing, and the inhomogeneous, gantry angle-dependent attenuation of the beam will need to be solved.

Keywords: EPID, dosimetry, MR-linac, QA, Unity.

3.1. Introduction

Electronic portal imaging devices (EPIDs), although originally intended for patient position verification, are increasingly being utilized for dosimetric applications, both for pre-treatment and *in vivo* dose verification. The amorphous silicon (a-Si) EPIDs mounted on conventional linacs have been extensively studied and have shown dose-response characteristics suitable for dose verification^{111–115,127–129}. The use of EPIDs for dosimetric purposes is already clinical routine^{88,90,130–132}.

One of the most interesting advancements in radiotherapy in recent years is the introduction of machines that combine a radiation source with an MRI system. The Elekta MR-linac system⁹² is equipped with an EPID, mounted on the rotating gantry, opposite to the accelerator head. This allows for simultaneous EPID acquisition and MR imaging⁹³.

The integration of a linac and an MRI system, combined with emerging techniques for fast re-contouring and re-planning, is expected to make online adaptive strategies a feasible technique in the clinic⁹⁴. The complexity of these techniques and of the newly developed MR-linac makes independent patient-specific dosimetric verification and quality assurance (QA) highly desirable.

EPID dosimetry has proven to be a valuable technique to identify errors related not only to data transfer, dose delivery, and patient set-up, but also to MLC calibration and to dose calculation¹⁰⁵. An intrinsic advantage of EPIDs is that they allow for dose verification in real-time^{89,133}. Within the framework of the MR-linac, where a different plan is generated and delivered every day, transit EPID dosimetry could provide an independent real-time verification of the entire treatment chain.

The purpose of this work was to examine the challenges related to the implementation of EPID-based dosimetric applications in the MR-linac. The presence of the MRI housing between the patient and the EPID acts as a secondary source of scatter and attenuates the primary beam. Also, the magnetic field causes an electron return effect on the secondary scattered electrons, both inside the bore and at the EPID level. The relative position of the panel in the system, the gantry angle dependence of the EPID signal, the EPID response to the MRI scatter and the pixel sensitivity variation with and without magnetic field were examined in this work. The panel repeatability, EPID ghosting, linearity and dose rate dependence of the panel were also studied.

A practical approach towards the development of an EPID dosimetry method for the MR-linac would be to adapt existing EPID solutions for conventional linacs. For this sake, and whenever applicable, the characteristics of the EPID in the MR-linac are compared to those in conventional linacs.

3.2. Materials and Methods

MR-linac, EPID, and acquisition software

The Unity MR-linac system consists of a linac (Elekta AB, Stockholm, Sweden) with a nominal 7 MV flattening filter free (FFF) beam and an integrated wide bore 1.5 T MRI scanner (Philips Medical Systems, Best, the Netherlands). The system is equipped with a multi-leaf collimator (MLC) consisting of 160 leaves with a projected width of a single leaf of 0.72 cm at the isocenter plane.

A ring gantry, on which the accelerator and EPID are mounted, is built around the MRI scanner, with the EPID opposite to the accelerator. In the geometry of the MR-linac, the source-to-isocenter distance is

143.5 cm, and the source-to-detector distance (SDD) is fixed to 263.5 cm, yielding to a magnification factor of 1.84. The maximum field size achievable with this MLC is $57 \times 22 \text{ cm}^2$ at the isocenter.

To minimize beam attenuation and obtain homogeneous transmission towards the isocenter, the central region (along the longitudinal direction) of the magnet is free of gradient coils and shimming hardware (Figure 1). A pipe in the MR scanner connecting the split coils is located at a gantry angle of 13° and the system does not allow the use of leaf pair/gantry combinations that cause direct irradiation to the pipe. The gap also limits the acquisition of un-attenuated beams to an irradiation field of a maximum of $\pm 4.8 \text{ cm}$ in each direction of the longitudinal axis at the isocenter. For larger fields, the exit beam's dimensions exceed the coil-free region and therefore, the beam is inhomogeneously attenuated at the EPID level.

The Elekta iViewGT panel is an a-Si flat panel X-ray detector (XRD 1642 AP, Perkin Elmer Optoelectronics, Wiesbaden, Germany) with a $41 \times 41 \text{ cm}^2$ detection area (1024×1024 pixels), with a pixel pitch of 0.4 mm. The integrated images were acquired using Elekta's iViewGT software (5.0.0). Frames were acquired with a frame integration time of 285 ms (3.5 fps). EPID movies were acquired with the XIS software (Perkin Elmer) with 266 ms frame integration time (3.7 fps). Single level gain calibration, bad pixel map and offset (dark current) correction were applied to all images. No saturation issues were experienced during the acquisition, given the fact that at the MR-Linac the panel is at a greater distance from the source and in addition there is a lot of extra attenuation, the panel therefore sees a very low dose rate compared to the dose rate of a panel in a standard linac with FFF beams.

Measurements for comparison to a conventional linac were performed using a 6 MV flattened photon beam of an SL20i linear accelerator

(Elekta AB, Stockholm, Sweden), equipped with a multileaf collimator (MLC) of 80 leaves with a projected leaf width of 1 cm at the isocenter, which is located 100 cm from the target. An Elekta iViewGT a-Si EPID (PerkinElmer RID 1640 AL5) was used at 60 cm from the isocenter.

In this work, the EPID output was calculated by averaging the signal received by the EPID on the on-axis region of 10×10 pixels ($4 \times 4 \text{ mm}^2$ at the EPID level). Unless explicitly mentioned, measurements in the MR-linac were performed with the magnetic field on, and all field sizes refer to the isocenter plane. As only relative measurements were performed using ionization chambers, array detectors and microDiamond detectors, no correction factors were required to account for effects of the magnetic field ^{134,135}.

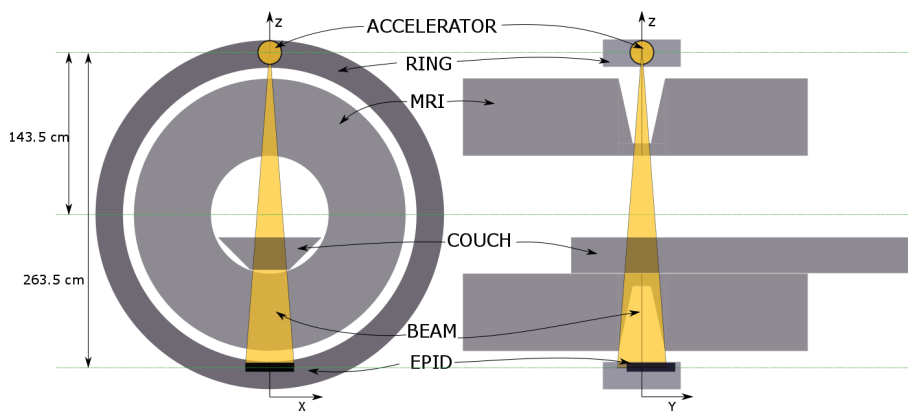


Figure 3.1. MR-linac cross-sections. In the Y-Z plane, the beam center is not aligned with the center of the panel (black box), so parts of large fields will fall outside the EPID detection area.

EPID relative position and MRI scanner

Due to mechanical constraints, the EPID is mounted in a fixed position and its center is not aligned to the center of the beam in the longitudinal direction (Y-direction in **Figure 3.1**). To measure the displacement of the EPID, square fields of sizes ranging from 2×2 to $8 \times 8 \text{ cm}^2$ of 200 MU

were used to irradiate the EPID and images were acquired. Borders of the fields were detected by an edge detection algorithm and the average offset for all images was determined.

The mechanical flex of the EPID in the MR-linac was calculated by irradiating a $5 \times 5 \text{ cm}^2$ field every 5 degrees and the field edge tracked on the EPID images to measure the lateral displacement.

EPID response to scatter from the MRI scanner

To study the effect of scatter from the MRI scanner on EPID images, microDiamond detector (PTW, Freiburg, Germany) measurements were performed at the EPID level and compared with portal images acquired for fields of increasing sizes (2×2 - $22 \times 22 \text{ cm}^2$) irradiated with 200 MU at gantry 0° . The results, normalized to the $10 \times 10 \text{ cm}^2$ measurement, were also compared to those from a conventional linac. A brass build-up cap was used to perform the microDiamond detector measurements on top of the EPID, and its position was aligned to the center of the beam using EPID images.

Angular dependence of the beam attenuation at isocenter and EPID level

With the design of the non-clinical prototype, structures of the couch, as well as structures in the MRI scanner, cause high attenuation of the beam at several gantry angles. This needs to be taken into account by the treatment planning system for delivery, but also when characterizing the response of the EPID for dosimetric purposes.

The dose at the isocenter was compared to the EPID signal. A Farmer-type ionization chamber (IC) (NE2571, Phoenix Dosimetry Ltd, Sandhurst, UK) in a homemade 20 cm diameter cylindrical PMMA phantom was used to acquire the angular output dependency of the

beam. The phantom was isocentrically aligned using two orthogonal EPID images. Readings were acquired for every 5 degrees, and every degree for regions with high gradient in attenuation. EPID images were acquired without the phantom in the beam, using a 10x10 cm² field, at the same angles as for the Farmer chamber measurements.

The angles 7-19 degrees were excluded from the study, as they are prohibited for 10x10 cm² fields due the pipe at 13°.

EPID response with and without magnetic field

In the presence of a magnetic field, the so-called electron return effect (ERE) occurs at interfaces between media with different electron densities. The ERE has been a subject of study within the MR-linac community for its role in dose redistributions at tissue-air boundaries^{91,117,136}. The ERE also affects scattered electrons, originating from the MRI housing between the isocenter and the EPID, the ring where the EPID is mounted, or within the EPID itself.

A 20 cm thick slab phantom was irradiated with square fields with sizes varying from 2x2 to 20x20 cm² using 200MU and EPID images were acquired, both with and without the magnetic field. The images with the magnetic field on were acquired one month after those with the field off. In that time, the EPID was recalibrated. Therefore, images acquired without the magnetic field were normalized to their counterpart in field-size with the magnetic field and compared by means of a 2D γ -analysis (local, 2%, 1mm, 50% isodose region) and X and Y lateral profiles were compared directly.

Finally, the magnetic field strength at the surface of the EPID was measured with a THM1176 magnetometer (MetroLab Technology SA, Geneva, Switzerland) and the radius of the curvature of the scattered electrons was calculated for the peak and average energies.

Linearity of the EPID signal with dose in integrated images

The EPID response has been shown to deviate from linearity for short exposures, and this behavior becomes more pronounced for higher dose rates^{113,114}. We investigated the linearity of the EPID dose response by delivering square fields of 20x20 cm² with different number of MUs (5, 10, 20, 50, 100, 200, 500, 1000 MU). Images were acquired with iViewGT in averaging mode, where the time-average of all acquired frames is recorded, along with a pixel factor which allows for the total signal to be calculated from the average image. A Farmer-type chamber was used simultaneously to record the linac output at the isocenter. The on-axis EPID pixel intensity was divided by the Farmer chamber value of each delivery to eliminate the effects of any fluctuation in the beam output, and the result was plotted as function of the number of MU and normalized to the 200 MU measurement. These measurements were performed for three dose rates (100%, 50% and 10% of 450 MU/min, the maximum dose rate) and each series was repeated three times.

Image lag in continuously acquired images

To study image lag in the EPID, the falling step response function (FSRF) was measured at maximum dose rate. Fields of 20x20 cm² were used and 1000 MU were delivered to reach equilibrium in the EPID signal. Frames were acquired until 100 frames after beam-off.

EPID response reproducibility

To study the short-term repeatability of the EPID response, an image was acquired every working day, over the course of 8 weeks. A field of 22x22 cm² field with 200 MU was used. At the same time, an IC measurement at the isocenter was performed to account for any fluctuations in the beam output.

For the IC measurement, a STARCHECK maxi MR ionization chamber

array (PTW, Freiburg, Germany) with 2 cm solid water buildup was used to measure the dose near d_{\max} on top of the couch inside the bore of the MR-linac, at 153.5 cm from the source. Both the central value of the STARCHECK and the averaged on-axis region of the EPID image were normalized to the $10 \times 10 \text{ cm}^2$ value of each measurement and the EPID values were divided by the IC ones.

3.3. Results

EPID relative position and MRI scanner

The displacement of the EPID was calculated to be 5.6 cm in the cranial direction at the EPID level, meaning that fields exceeding 8.1 cm in the cranial direction at isocenter plane cannot be completely detected by the EPID since part of the beam falls outside the panel.

Behind the parts of the beam that are shielded by the gradient coils, the attenuation was found to be up to 47% larger than on the beam axis, affecting only beams larger than 4.8 cm in both the cranial and caudal directions of the longitudinal axis.

The non-centered position of the panel and the strongly attenuated parts of the beam travelling through the gradient coils of the MRI can be seen in **Figure 3.2** where EPID images acquired with a large square field on the MR-linac and a conventional linac are compared.

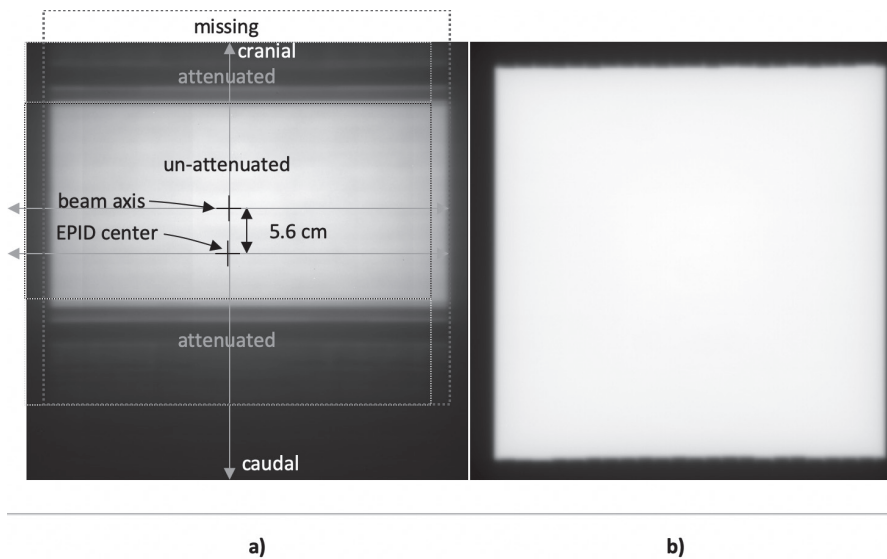


Figure 3.2. a) EPID image of a $20 \times 20 \text{ cm}^2$ (FFF) beam, acquired on the MR-linac system. The centers of the EPID and the beam are marked with a cross and a dashed line shows the entire square shape of the field arriving to the EPID, which the EPID receives in un-attenuated parts (like in conventional linacs), attenuated parts, and missing parts. b) EPID image of a $23 \times 23 \text{ cm}^2$ beam in a conventional linac (with flattening filter). Note that, for the sake of visual comparison, the field sizes at isocenter differ in order to receive an effective field of approximately 36.8 cm^2 at the EPID level in both cases.

The mechanical flex of the EPID in the MR-linac was found to have a largest deviation of 0.6 mm in the left-right direction and 0.2 mm in the cranial-caudal direction. This is a smaller deviation than in conventional linacs, where the average of the largest deviations are 1.3 mm and 1.6 mm respectively, probably because the EPID in the MR-linac is mounted on a ring allowing for minimum movement.

EPID response to scatter from the MRI scanner

In the MR-Linac (with the magnetic field activated), the EPID central area pixel intensity as a function of field size, presented in **Figure 3.3**, shows a different response compared to the microDiamond detector measurements at the EPID level (same SDD). For direct comparison,

EPID and microDiamond relative outputs acquired at a conventional linac are also plotted, showing closer agreement with each other. A ratio of the microDiamond measurement to the EPID signal output is shown for the MR-Linac and the conventional Linac.

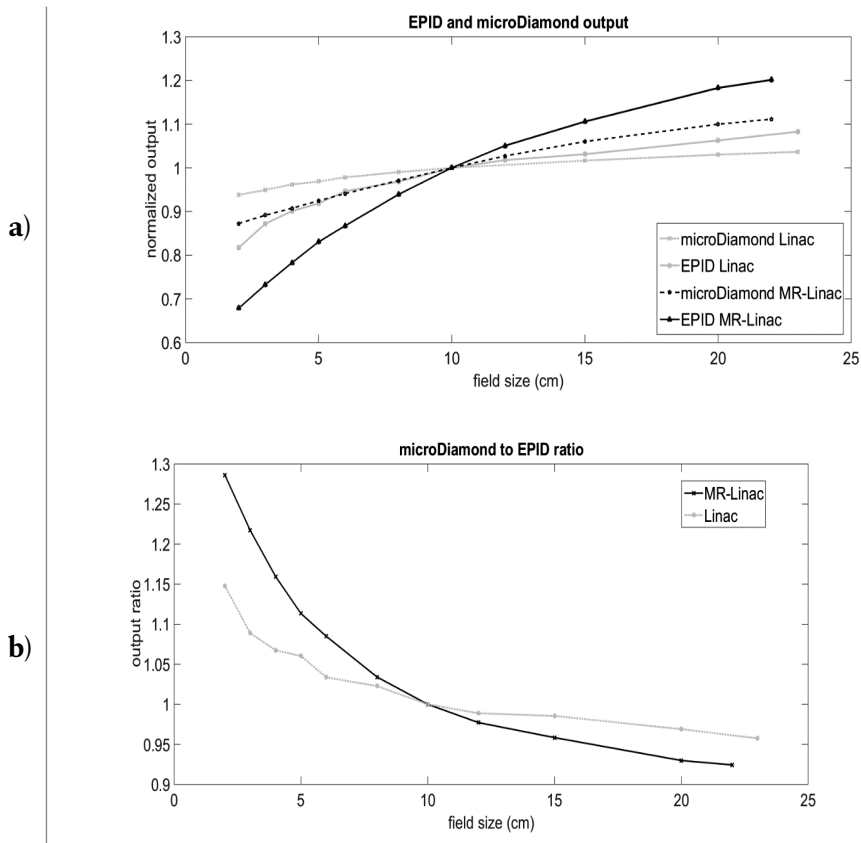


Figure 3.3. **a)** Field size dependence of microDiamond detector measurements at the EPID level (dashed line) and averaged EPID signal over the central 10x10 pixels (solid line) for the MR-linac system (black) and a conventional linac (grey); **b)** the output ratio of the microDiamond detector to the EPID signal is plotted for both the conventional linac (dashed grey) and the MR linac (solid black).

In the MR-linac, the steeper curve of the EPID response, compared to the MicroDiamond detector signal, can be attributed to the higher

sensitivity of the EPID to low-energy scatter, resulting from the combination of electrons scattered from the MRI-housing and the small air gap.

In the MR-linac, the relative output of the EPID compared to the MicroDiamond detector ranged from -22.3% to 8.2%, whereas in a conventional linac it ranged from -12.9% to 4.4% for field sizes of 2x2 and 22x22 cm² respectively.

Angular dependence of the beam attenuation at isocenter and EPID level

In **Figure 3.4. a)**, an experiment performed with the magnetic field activated, shows the output of the beam measured at the isocenter with an IC (black) in a cylindrical phantom for a 10x10 cm² square field. In grey, the averaged signal from the central region of the EPID images is plotted. The curves are normalized at the 90 degrees gantry angle, where the beam does not traverse the treatment couch for the two measurements.

Figure 3.4. b) shows a polar plot of the ratio of the IC/EPID readings as a function of the gantry angle indicating that there is a varying attenuation between the isocenter and the EPID. Note that in both graphs the region between 7 to 20 degrees is omitted, since irradiation is prohibited due to the presence of a pipe, at 13 degrees. In **Figure 3.4. a)** and **b)** the attenuation of the pipe is clearly apparent as a drop in EPID signal for gantry angles around 193 degrees.

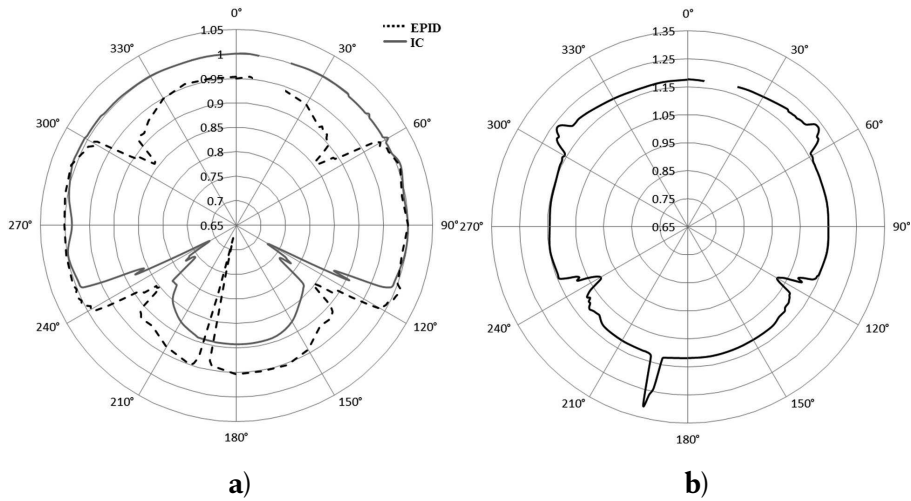


Figure 3.4. a) The output factor at the isocenter (solid-grey) and at EPID level (dashed-black) as function of the gantry angle and normalized to the measurement at 90 degrees. b) The normalized ratio of IC/EPID.

Drops in the EPID measured output at gantry angles 55, 120, 240 and 305 are related to structures of the couch attenuating the beam non-uniformly on its path towards to EPID. The output factor measured at the isocenter only reflects the attenuation at gantry angles 120 and 240, when the couch structures are irradiated before reaching the detector at isocenter.

EPID response with and without the magnetic field

The magnetic field measured on the surface of the panel did not exceed 10 mT, yielding an electron trajectory radius of 2.2 m for a peak energy of 6 MeV, and of 0.84 m for an average energy of 2 MeV. **Figure 3.5** shows the normalized relative profiles of EPID images acquired when a 20 cm thick slab phantom was irradiated with square fields with and without the magnetic field. More than 99% of points show local deviations smaller than 3%. 2D γ -analysis (local, 2%, 1 mm, 20%) reported an average value of γ_{mean} of 0.15 ± 0.06 (1SD) and an average γ pass rate of 98.6% ([98.0, 99.1], 95% CI).

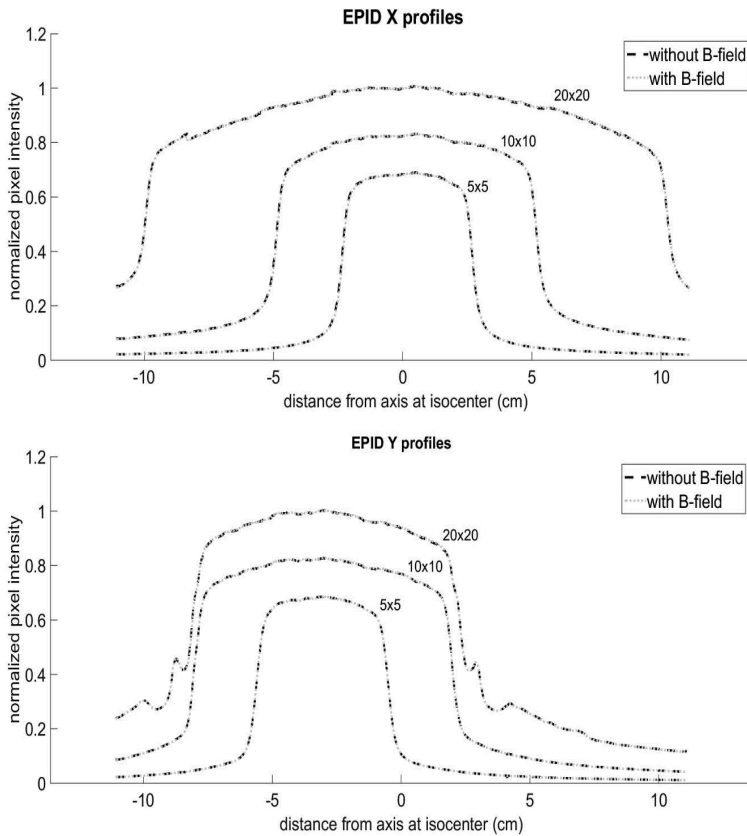


Figure 3.5. X (top) and Y (bottom) EPID lateral profiles of square fields irradiated with 5x5, 10x10 and 20x20 cm² to a 20 cm slab phantom are shown for images acquired with (dotted-grey) the magnetic field, and without (dashed-black). Note the shift of the Y profiles due to the non-centered position of the EPID, as well as the strong attenuation because of coils affecting the 10x10 cm² curve in the penumbra, and more clearly the 20x20 cm² field, creating also oscillations due to heterogeneities in the cryostat, and the ring.

Linearity of the EPID signal with dose in integrated images

With the magnetic field activated, the relative response of the panel, calculated as the EPID signal divided by the corresponding IC value, is plotted against the delivered MUs, normalized to 200 MU (**Figure**

3.6. a)). Also included is the data from a measurement performed on a conventional linac. Variations in the EPID response are within 4% for the MR-linac. This is similar to previously published results in conventional linacs ^{137,138} and comparable to other panels at our department that are currently used for *in vivo* dosimetry. In **Figure 3.6. b)** the relative EPID response at different dose rates is plotted. The best linearity is observed at lower dose rates.

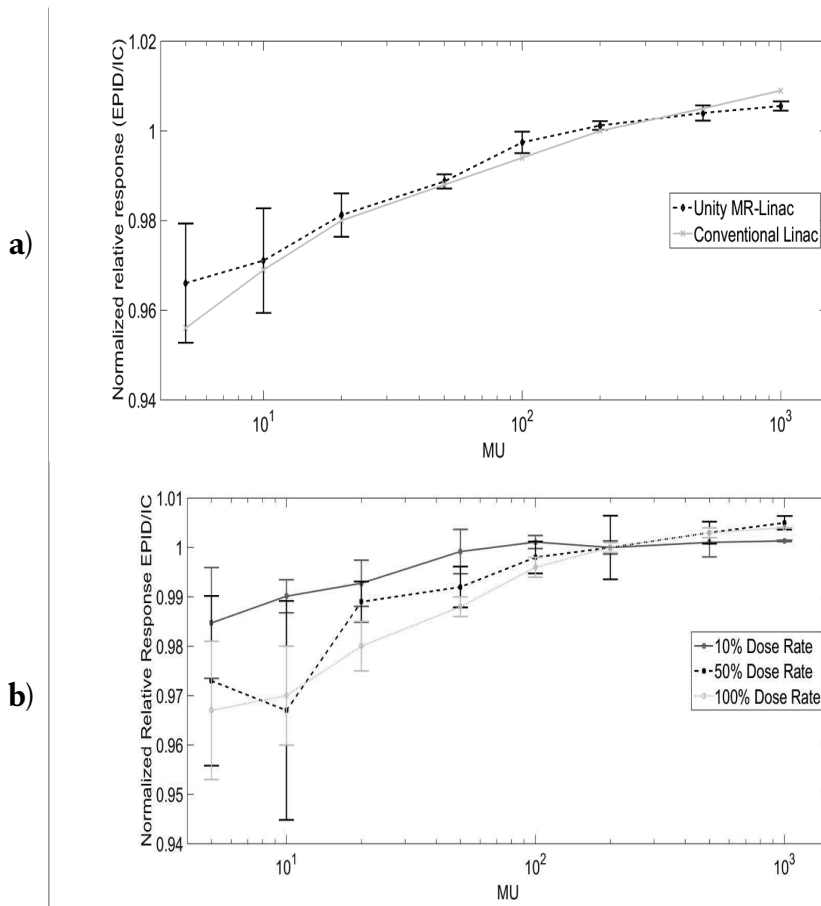


Figure 3.6. a) The relative EPID response (EPID/IC) as a function of dose for a varying number of MUs is plotted for the MR-linac (dashed-black) and in a conventional linac (solid-grey), normalized to the 200 MU point. Variations of the EPID signal divided

by the IC measurement are found within 4% at low MUs for the MR-linac. When compared to the same experiment performed at a conventional linac with the same model panel, deviations were within 5%. **b)** The relative EPID response (EPID/IC) as a function of dose for the MR-linac, normalized to the 200MU point, for 100% dose rate (dotted-light grey), 50% (dashed-black) and 10% (solid-dark grey). Error bars show the standard deviation of 3 measurements.

Image lag in continuously acquired images

Measuring the falling step response function (FSRF), after the beam at equilibrium was turned off, the EPID signal dropped below 2% of equilibrium value after 0.6 seconds (2 frames) and below 1% after 2 seconds (or 7 frames).

EPID response reproducibility

The ratio of the daily EPID and ionization chamber output was normalized to the average ratio measured over 8 weeks. A standard deviation of 0.5% (1 SD) was found, comparable to other EPID studies in conventional linacs ¹¹⁹.

3.4 Discussion

We have studied the dosimetric characteristics of the a-Si panel in the Elekta Unity machine and pointed out the challenges and limitations towards its use in dose verification applications.

A main drawback of the current setup is that parts of fields exceeding 8.1 cm in the cranial direction at isocenter will not be able to be verified with the EPID due to the non-centered position of the panel. The consequences of this EPID displacement will vary depending on the solution to be used. For *in vivo* EPID dosimetry in 3D, transit EPID patient images are typically used to reconstruct the 3D dose distribution within the patient whether using a back-projection algorithm or by

estimating the energy delivered fluence by the accelerator and then using it as input to a dose engine for a forward dose calculation. In these solutions, the EPID images of large fields will miss parts of the beam and this will lead to wrong reconstructions. For these large fields though, *in vivo* dose verification in 2D (or point dose) may still be possible by using back-projection algorithms on the available part of the beam or by using other transit EPID-dosimetry solutions such as predicted portal image methods. In all cases, an automatic position correction of the EPID images to the center of the beam has to be introduced for EPID dosimetry at a pre-processing stage.

The relative signal of the EPID, for increasing field sizes, compared to the relative output of a microDiamond detector measuring on top of the EPID, confirms the over-sensitive response of the panel compared to the chamber, suggesting a large amount of scatter, originating in the MRI housing and reaching the EPID. When EPID images are used for dosimetry, a correction for the MRI to EPID scatter must be applied after the raw image is processed. Moreover, although the definitive version of the couch is expected to differ from the current design, we showed that the attenuation of the beam between the isocenter and the EPID is not homogenous for the entire image, since couch structures and the MRI gradient coils cause extra attenuation as the beam traverses them. Additionally, this attenuation has been shown to be gantry angle dependent, suggesting that any correction applied to correct for scatter and attenuation through the MRI scanner would also have to be gantry angle dependent. A proof of concept for an adaptation of a back-projection algorithm to account for the presence of the MRI scanner between the isocenter and the EPID is investigated in ¹³⁹. The EPID signal in Figure 4 is, withal, less modulated with rotation than the IC output due to scattered photons that the EPID receives from the MRI scanner, therefore the attenuation factor should be determined after the scatter from the MRI scanner has been subtracted. However,

the use of the EPID for predicted portal images would not require the correction for scatter and attenuation from the MRI scanner, but only a characterization of the EPID response.

The low field strength and calculated radius of curvature of electrons at the level of the EPID suggested that any effect of the magnetic field on the EPID images would be negligible. This was confirmed in this study with EPID images acquired without the magnetic field. In other words, no additional refinements are required for the dose modelling of the EPID in the MR-linac due to the presence of a magnetic field. The magnetic field will have to be accounted for in *in vivo dose* reconstructions, of course. This could be achieved by using the log files of the linac to estimate the delivered fluence by the accelerator and then using it as input to a dose engine that accounts for magnetic field effects in its forward dose calculations. Back-projection algorithms are not capable of correct for the presence of magnetic fields. An alternative would be to compare the reconstructed dose to a new plan in the TPS, calculated without the magnetic field just for verification purposes (a ‘non-magnet’ solution, similarly to the ‘in-aqua’ concept for lung cases⁸⁶). Alternatively, a back-projection of the EPID images to obtain the primary fluence in front of the patient could be used to feed a Monte Carlo simulation accounting for the magnetic field effects, and to be compared to the planned dose distribution from the TPS.

The linearity of the EPID response with dose was shown to be comparable to that of other panels in our department. The similarity between the results for the detector in the MR-linac and in a conventional linac suggests that dose linearity and dose rate dependency do not compromise the dosimetric performance of the panel in Elekta’s MR-linac.

The accuracy achieved by an EPID dosimetry solution in the MR-linac remains to be seen when the challenges listed in this paper have been addressed.

3.5. Conclusion

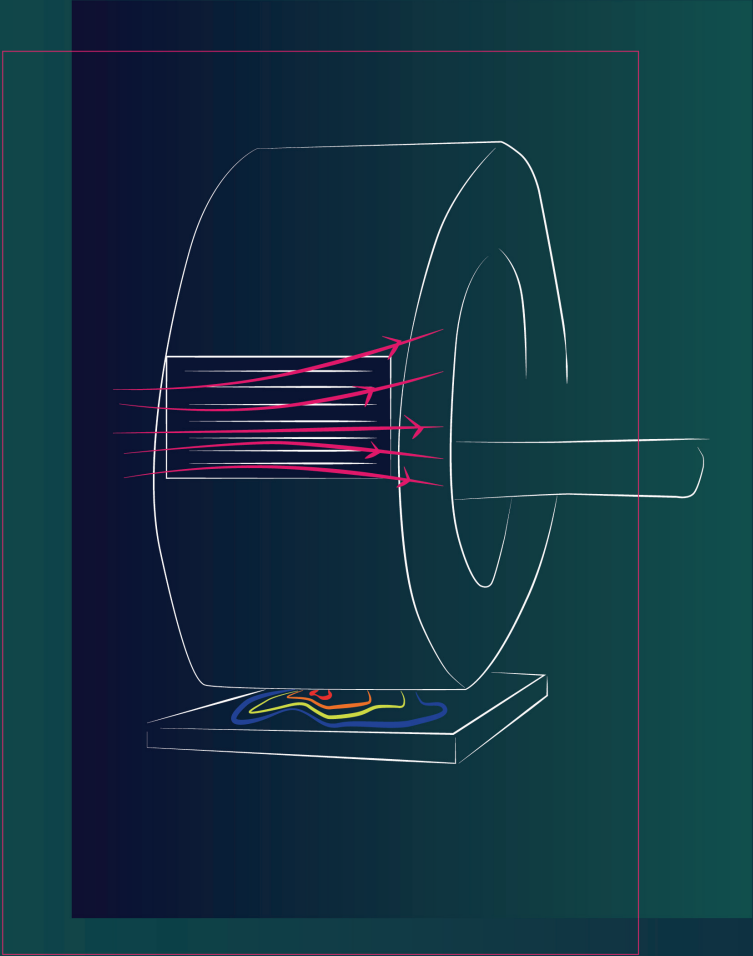
The study of several characteristics of the EPID and its use for dosimetric applications suggests that the magnetic field, the dose rate dependency, and dose linearity have similar results compared to experiments performed in conventional linacs. However, the implementation of in vivo transit EPID dosimetry solutions will have to address the challenge of the panel position and include gantry angle-dependent corrections for both the attenuation of the beam and the scatter from the MRI housing.

3.6. Disclosure of conflicts of interest

Support for this research was provided, in part, by Elekta AB, Stockholm, Sweden.

3.7. Acknowledgments

We would like to thank Jochem Kaas, Thijs Perik, Begoña Vivas and Robert Spaninks for assistance with the measurements.



4.

TWO DIMENSIONAL EPID DOSIMETRY FOR AN MR-LINAC: PROOF OF CONCEPT.

**Iban Torres-Xirau
Igor Olaciregui-Ruiz
Uulke A. van der Heide
Anton Mans**

Department of Radiation Oncology,
The Netherlands Cancer Institute–Antoni van Leeuwenhoek Hospital,
Plesmanlaan 121, 1066 CX Amsterdam, The Netherlands

*Medical Physics, Volume 46, Number 9, Pages 4193-4203
Published September 2019 • © 2019 American Association of Physicists in
Medicine*

Abstract

At our institute, *in-vivo* patient dose distributions are reconstructed for all treatments delivered using conventional linacs from Electronic Portal Imaging Device (EPID) transit images acquired during treatment using a simple back-projection model. Currently, the clinical implementation of MRI-guided radiotherapy systems, which aims for online and real-time adaptation of the treatment plan, is progressing. In our department the MR-linac (Unity, Elekta AB, Stockholm, Sweden) is now in clinical use. The aim of this work is to demonstrate the feasibility of 2D EPID dosimetric verification for the MR-linac by comparing back-projected EPID doses to ionization chamber (IC) array dose distributions.

Our conventional back projection algorithm was adapted for the MR-linac. The most important changes involve modeling of the attenuation by and scatter from the cryostat. The commissioning process involved the acquisition of square field EPID measurements using various phantom setups (varying SSD, phantom thickness and field size). Commissioning models were created for gantry 0, 90 and 180 degrees and verified by comparing EPID reconstructed 2D dose distributions to measurements made with the OCTAVIUS 1500 IC array (PTW, Freiburg, Germany) for 2 prostate and 1 rectum IMRT plans (25 beams total). The average of the γ parameters (γ -mean and γ -pass rate) and the dose difference at a reference point were reported. Due to their construction, the attenuation of couch, bridge and cryostat shows a much stronger dependence on gantry angle in the MR-linac compared to conventional linacs. We present a method to correct for these effects. This method is validated by dose reconstruction of the 25 IMRT beams recorded at a certain gantry angle using the model of another gantry angle, combined with the correction method.

For dose verification performed at a gantry angle identical to the

commissioned model the average y-mean and y-pass rate values (3% global dose, 2 mm, 10% isodose) were 0.37 ± 0.07 and 98.1, 95% CI [98.1 \pm 2.4], respectively. The average dose difference at the reference point was $-0.5\% \pm 1.8\%$. Verification at gantry angles different from the commissioned model (i.e., using the gantry angle dependent correction) reported 0.39 ± 0.08 and 97.6, 95% CI [96.9, 98.3] average y-mean and y-pass rate values. The average dose difference at the reference point was: $-0.1\% \pm 1.8\%$.

The EPID dosimetry back projection model was successfully adapted for the MR-linac at gantry 0° , 90° and 180° , accounting for the presence of the MRI housing between phantom (or patient) and the EPID. A method to account for the gantry angle dependence was also tested reporting similar results.

Keywords: EPID, portal dosimetry, dose verification, MR-linac, QA, Unity.

4.1. Introduction

Although Electronic portal imaging devices (EPIDs) were originally designed for patient position verification, their use for dosimetric applications has been acknowledged both for pre-treatment and *in vivo* dose verification. The dose-response characteristics of amorphous silicon (a-Si) EPIDs have been broadly studied^{113,114,119,138,140-143} and several EPID based solutions are being used both for intensity-modulated radiation therapy (IMRT)^{24,58,60,144-147} and VMAT^{57,59,148-150} treatments.

Recently, treatment machines combining a radiation source with an MRI system have been developed and are clinically used. In our department, the MR-linac (Unity, Elekta AB, Stockholm, Sweden)^{92,151} has been installed and patient treatments have started. The system is equipped with an EPID mounted on the rotating gantry, opposite to the accelerator head, allowing for simultaneous beam irradiation, EPID acquisition and MR imaging⁹³.

Online adaptive strategies in MRIgRT will become clinically feasible⁹⁴ as result of the ongoing developments in fast re-contouring and re-planning. In this context, independent tools for the verification of these adaptive treatments will become imperative. Existing pre-treatment tools for QA in the MR-linac are typically time-consuming solutions which, besides, are not applicable for an online adaptive workflow⁹⁷⁻¹⁰⁰. Alternative patient-specific QA solutions have been proposed, such as fast sanity checks on the adapted plan¹⁰¹, *in-vivo* geometrical accuracy of the delivery using EPID images¹⁵², or the use of independent calculations fed with linac log files^{76,153-155}.

An MR-only workflow would allow for MRI-based delineation while performing dose calculation on a synthetic CT derived from that MRI study. The use of log files in combination with an independent dose calculation algorithm using the synthetic CT is an alternative treatment verification method. However, this approach relies on the correctness

of the log files ¹⁰⁵ and synthetic CT, and independent dose algorithms that consider the magnetic field are not widely available.

Currently, in all institutions that have started treating patients on the MR-linac, the dosimetric verification of adapted plans if performed is done after the treatment fraction using a detector array or film in combination with a phantom. The use of transit EPID dosimetry provides a complementary solution to these methods, able to perform an independent end-to-end check of the entire chain, verifying data transfer, dose delivery, patient set-up, MLC calibration and dose calculation ¹⁰⁵, and also synthetic CT determination. Moreover, the EPID is already attached to the machine, and allows for automation and even in real-time treatment verification ^{89,133}. However, it also comes with limitations given the position of the panel with respect to the beam, and when used without taking the magnetic field into account in the back-projection dose engine.

We have shown the dosimetric characteristics of the EPID to be similar in the MR-linac compared to conventional linacs ¹⁵⁶. Furthermore, the magnetic field at the EPID location is very low (the time-varying component during imaging even lower) and has been demonstrated not to influence the EPID images ¹⁵⁶. This suggests feasibility of the adaptation of existing back-projection models to the MR-linac geometry. The feasibility of correcting EPID images for the presence of extra scattering and attenuating material between phantom and EPID has also been demonstrated ¹³⁹. The aim of this study is to bring all these prior results together, and demonstrate the feasibility of back-projection EPID dosimetry for the MR-linac by comparing 2D EPID reconstructed dose distributions to absolute dose measurements in a phantom.

4.2. Materials and Methods

4.2.1 Accelerator, EPID, acquisition software and measuring equipment.

The MR-linac system combines a 7 MV flattening filter free (FFF) beam linac (Elekta AB, Stockholm, Sweden) with an integrated wide bore 1.5 T MRI scanner (Philips Medical Systems, Best, the Netherlands). The MR-linac uses an Elekta Agility-based multi-leaf collimator (MLC) consisting of 160 leaves with a projected width of a single leaf of 0.72 cm at the isocenter plane.

The accelerator and EPID are mounted on a ring gantry built around the MRI scanner. The source-to-isocenter distance is 143.5 cm, and the source-to-detector distance (SDD) is fixed to 265.3 cm, resulting in a magnification factor of 1.84. The central region of the magnet is free of gradient coils and shimming hardware, allowing for minimal and homogenous attenuation of the beam by the cryostat. This region determines the maximum allowed field size in the longitudinal direction (± 11 cm at isocenter). The effective size of the beam exiting the MRI scanner is larger due to divergence, limiting the EPID acquisition of un-attenuated beams to an irradiation field of a maximum of ± 4.8 cm in each direction of the longitudinal axis at the isocenter. For larger fields, the exit beam's dimensions exceed the coil-free region and therefore, the exit beam is inhomogeneously attenuated. Moreover, due to the non-centered position of the EPID with respect to the beam axis, fields exceeding 8 cm in the positive longitudinal axis are not entirely captured by the EPID. **Figure 4.1** illustrates the EPID position in the MR-linac geometry and the characteristics of acquired images. Therefore, in this study the reconstructed dose distributions are truncated at ± 5.6 cm, close to the border of the area of homogenous attenuation.

Due to the rigid ring gantry on the Unity system, the EPID sag is smaller than in conventional linacs. On our system, the isocenter position on the panel was determined to be stable within 0.5 mm, which we considered negligible to our purposes. The Elekta iViewGT panel is an a-Si flat panel X-ray detector (XRD 1642 AP, Perkin Elmer Optoelectronics, Wiesbaden, Germany) with a $41 \times 41 \text{ cm}^2$ detection area (1024×1024 pixels), and a pixel pitch of 0.4 mm. Images were acquired using Elekta's MVIC software. Array measurements were performed using an MR-compatible OCTAVIUS 1500 2D detector array (PTW, Freiburg, Germany), having 1405 vented ICs with 7.1 mm center-to-center distance, with an uncertainty of $\pm 0.5\%$, which was cross-calibrated to a known value for a reference beam.

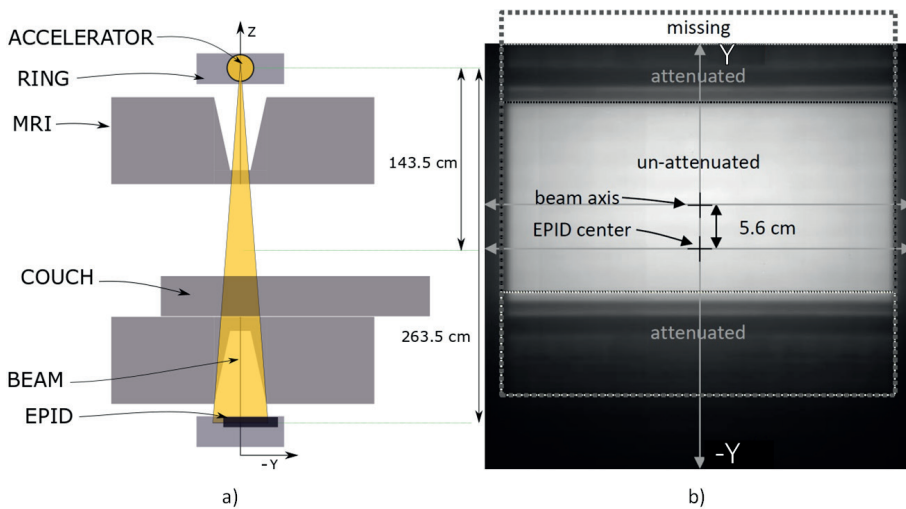


Figure 4.1: a) MR-linac cross-section. In the Y direction, the beam center is not aligned with the center of the EPID. Therefore, parts of large fields fall outside the EPID detection area. b) EPID image of a $20 \times 20 \text{ cm}^2$ (FFF) beam. The centers of the EPID and the beam are marked with a cross and a dashed line shows the entire square shape of the field arriving to the EPID, which the EPID receives in un-attenuated parts (like in conventional linacs), attenuated parts, and missing parts.

4.2.2. Back-projection algorithm for the MR linac

4.2.2.1. Rationale

The conventional back-projection algorithm requires the portal dose distribution at the EPID level, the transmission through the phantom (or patient) and the geometry of the phantom (or patient). For the determination of the portal dose distribution at the EPID level, the parameters of our algorithm are fitted against IC dose measurements performed at the level of the EPID. Such measurements are made by an IC inside a cylindrical miniphantom at the location of the EPID^{58,70}. This is impossible in the MR-linac due to the location of the panel, as there is no physical space to execute such measurements. Therefore, similar measurements were made at the isocenter and rescaled to the EPID level using the inverse square law (ISQL), to be used as surrogate for measurements at position of the EPID in the absence of the cryostat. The purpose of these adaptations to the back-projection algorithm is to estimate the attenuation and scatter sensed by the EPID, generated by the cryostat, couch and bridge. Using this result, the primary dose at the EPID level can be determined. Effectively, the adapted algorithm removes the influence of the cryostat and the intrinsic scatter generated within the EPID in the conversion from pixel values to portal dose distributions at EPID level. The other parts of the back-projection algorithm are not modified.

4.2.2.2 IC array measurements

The array is used in two configurations. First, to measure dose at d_{max} (with 13 mm of buildup) at isocenter as a surrogate for dose measurements in the miniphantom for conventional linacs. Second, for measurements at 10 cm depth, the detector array is placed at 10 cm from surface of a 23 cm slab phantom, since the couch of the MR-linac does not allow for vertical motion and the isocenter lies at 13 cm above the couch.

4.2.2.3. Image processing

All acquired EPID images are pre-processed into the PV_{ij}^{proc} , which is the time-integrated pixel value EPID image corrected for the dark field, the flood field and for bad pixels ¹¹⁹, and shifted 5.6 cm in the Y-direction to compensate for the off-axis alignment of the panel with respect to the beam ¹⁵⁶.

4.2.2.4. Sij Matrix

The Sij matrix is a correction directly applied to each PV_{ij}^{proc} image to compensate for pixel sensitivity variations and off-axis differential photon energy ⁴⁶. Note that in MR-linac case, the Sij matrix is also influenced by the attenuation of the beam through the MRI scanner between isocenter and EPID. The Sij matrix is defined as follows:

$$S_{ij} = \frac{OCT_{ij}^{ISO \rightarrow EPID, 22 \times 22}}{PV_{ij}^{proc, 22 \times 22}} \quad (1)$$

where OCT is the measurement of a large field (22x22 cm²) by the OCTAVIUS 1500 detector array at d_{max} positioned at isocenter and scaled to EPID level (using the ISQL). $PV_{ij}^{proc, 22 \times 22}$ is the corresponding EPID image after processing. The OCTAVIUS 2D array field was bilinearly interpolated and later a uniform smoothing over a 5x5 pixel neighborhood was performed to achieve the spatial resolution of the EPID.

4.2.2.5 Determination of the portal dose

Ideally, the conversion from pixel values to dose should be linear. The dose response D_r is defined as the ratio between the central region pixels and their corresponding dose measurement. The resulting image is called dose image:

$$D_{ij}^{EPID} = PV_{ij}^{proc} \cdot S_{ij} \cdot D_r \quad (2)$$

Note that the S_{ij} matrix was obtained with measurements performed with a large field ($22 \times 22 \text{cm}^2$), so the dose image corresponds to the measured portal dose distribution only for this field size. However, the component of scatter from the MRI scanner towards the EPID, $Sc_{ij}^{MRI \rightarrow EPID}$ and the component of lateral scatter within the EPID, Sc_{ij}^{EPID} , are field size dependent. Hence, for any arbitrary field size, the dose image can be expressed as:

$$D_{ij}^{EPID} = PD_{ij}^{EPID'} + Sc_{ij}^{MRI \rightarrow EPID} + Sc_{ij}^{EPID}, \quad (3)$$

where $PD_{ij}^{EPID'}$ is the portal dose distribution measured for an arbitrary field size, without the extra effects of the cryostat, couch and bridge, and the scatter of the EPID. The scatter from the MRI towards the EPID is modeled as a convolution between the dose image D_{ij}^{EPID} and a scatter kernel $K_{ij}^{MRI \rightarrow EPID}$. Simultaneously, the scatter occurring within the EPID Sc_{ij}^{EPID} , is modeled as a deconvolution between the resulting dose image D_{ij}^{EPID} minus the scatter from the MRI to the EPID, and a scatter kernel K_{ij}^{EPID} :

$$Sc_{ij}^{MRI \rightarrow EPID} = D_{ij}^{EPID} \otimes K_{ij}^{MRI} \quad (4)$$

$$Sc_{ij}^{EPID} = (D_{ij}^{EPID} - Sc_{ij}^{MRI \rightarrow EPID}) \otimes^{-1} K_{ij}^{EPID} \quad (5)$$

As kernels we use a Gaussian filter for $K_{ij}^{MRI \rightarrow EPID}$ and the kernel suggested in ⁷⁰ for the K_{ij}^{EPID} :

$$K_{ij}^{MRI} = \frac{c_{MRI}}{2\pi\sigma_{MRI}^2} \exp\left(-\frac{r_{ij}^2}{2\sigma_{MRI}^2}\right) \quad (6)$$

$$K_{ij}^{EPID} = c_{DR} \begin{cases} c_1 \cdot \frac{e^{-\mu r_{ij}}}{r_{ij}^2} & \text{for } r_{ij} \neq 0 \\ 1 & \text{for } r_{ij} = 0 \end{cases}, \quad (7)$$

Where r_{ij} is the distance of a pixel ij from the central axis and c_{MRI} , σ_{MRI}^2 , c_{DR} , c_1 and μ are the kernel parameters. The portal dose in (3) is then calculated as:

$$PD_{ij}^{EPID'} = D_{ij}^{EPID} - (D_{ij}^{EPID} \otimes K_{ij}^{MRI \rightarrow EPID}) - (D_{ij}^{EPID} - (D_{ij}^{EPID} \otimes K_{ij}^{MRI \rightarrow EPID})) \otimes^{-1} K_{ij}^{EPID} \quad (8)$$

Which is a function of the dose response Dr , and the parameters that determine the kernels K_{ij}^{EPID} and K_{ij}^{MRI} as expressed by:

$$PD_{ij}^{EPID'}(Dr, \sigma_{MRI}^2, c_{MRI}, c_{DR}, c_1, \mu) \quad (9)$$

The values of these model parameters are determined by a parametric fit of on-axis EPID-reconstructed dose values and the corresponding array measurements, for a set of field sizes (2x2 – 22x22 cm²). For an accurate description of the portal dose image over the entire field of view, a 2D fitting procedure is finally introduced to minimize the difference in profiles of PD_{ij}^{EPID} images and array measurements. The corrected dose image PD_{ij}^{EPID} is defined as the dose image, $PD_{ij}^{EPID'}$ convolved with a kernel, K_{ij}^{prof} :

$$PD_{ij}^{EPID} = PD_{ij}^{EPID'} \otimes K_{ij}^{prof}, \quad (10)$$

K_{ij}^{prof} is defined as a Gaussian kernel:

$$K_{ij}^{prof} = \frac{c_{prof}}{2\pi\sigma_{prof}^2} \exp\left(-\frac{r_{ij}^2}{2\sigma_{prof}^2}\right), \quad (11)$$

In order to determine the optimal σ_{prof}^2 and c_{prof} parameters of, K_{ij}^{prof} , the Euclidian distance between EPID and normalized measured profiles was minimized for all field sizes.

4.2.2.6 Final steps

After the portal dose image is calculated, the next steps of the adapted back-projection algorithm are identical to the conventional model: the portal dose is used to calculate the primary transmission using portal images with and without the phantom (or patient) in the beam. The primary dose within the phantom, P_r , is weighted with the Scatter-to-Primary Ratio (SPR) determined under reference conditions, SPR_{ref} , which accounts for the thickness dependence of the scatter. The SPR is parametrized as a function of the primary transmission, the thickness of the patient and the depth of the reconstruction plane. Next, the result is convolved with the scatter kernel $K_{mid,ij}$, accounting for the field size dependence of the scatter in the reconstruction plane.

4.2.3. Full commissioning at gantries $0^\circ, 90^\circ, 180^\circ$

In our back-projection algorithm for conventional linacs, all gantry angles are equivalent in terms of EPID pixel conversion to dose. Hence, the parameters of the back-projection model are commissioned using measurements performed at gantry 0° , which are applied for all gantry angles. The only gantry angle dependent factor in the model is the correction for the attenuation of the couch top at the exit side of the patient. This is accounted for by a 2D couch attenuation model¹⁵⁷. In the MR-linac geometry, however, the attenuation of the cryostat, couch and bridge (at the exit side of the phantom) varies considerably with

gantry angle. Ideally, the commissioning of the back-projection model would be performed for each possible gantry angle. However, as a gantry-mounted detector setup is not feasible within a slab phantom in the MR-linac, the commissioning process can only be carried out when the detector is perpendicular to the radiation beam, that is for gantry angles of 0° , 90° , 180° and 270° . Because of symmetry on the set-up, gantry angle 270° was omitted from this study. The set of measurements required for the full commissioning of our model is summarized in **Table 4.1**.

Table 4.1: Set of absolute dose measurements needed for the EPID back-projection model commissioning in the MR-linac geometry. Note that an EPID image needs to be acquired for each of these measurements.

Measurement	Comment	Equipment	Phantom (cm ³)	Field Size (cm ²)
1. S_{ij} matrix	To measure the relative sensitivity over the entire EPID and the 2D transmission through the MRI scanner	OCTAVIUS 1500 array at d_{\max}		22x22
2. Field size series	No phantom, varying field size	OCTAVIUS 1500 array at d_{\max}		2x2-20x20
3. Phantom series	Constant phantom thickness, varying field size	OCTAVIUS 1500 array at isocenter in slab phantom	30x30x20	2x2-20x20
4. Thickness series	Constant field size, varying phantom thickness	OCTAVIUS 1500 array at isocenter in slab phantom	30x30x 4-32	10x10

5. Gantry Angle Corr.	Large field at every gantry angle.	OCTAVIUS 1500 array at d_{\max}	22x22
--------------------------	---------------------------------------	---	-------

4.2.4. IMRT plans validation at gantries 0°, 90°, 180°:

At the time of this study, we chose patient categories that were likely to be treated first on the MR-linac. 3 plans (2 prostate and 1 rectum) were used, with around 1000 MU each, consisting of 25 beams (9, 9 and 7 respectively) ranging from 5 to 20 segments per beam, with a largest irradiated segment per plan of 48 cm² to 280 cm² were irradiated to a 23 cm slab phantom at the three gantry angles (0°, 90° and 180°). Additionally, the 2D detector array was used to measure dose distributions at the isocenter level at 10 cm depth. The EPID images were back-projected to the isocenter plane using the adapted back-projection algorithm commissioned at the corresponding gantry angle. 2D γ analysis (3% global, 2mm at 10% isodose) was performed between the detector array and EPID reconstructed dose distributions. The reference point was determined as the point with the lowest gradient within the points with dose value equal to or greater than 80% of the maximum in the measured dose.

4.2.5. Gantry angle correction

A method was introduced to adapt the commissioning model for use at arbitrary gantry angles. This approach assumes that the differences between the different gantry configurations affect the S_{ij} matrix and the dose response. The modification of the S_{ij} Matrix is given by:

$$S_{ij}^{CGA \rightarrow AGA} = S_{ij}^{CGA} \frac{PV_{ij}^{proc, 22x22, CGA} OCT_{ij}^{ISO \rightarrow EPID, 22x22, AGA}}{PV_{ij}^{proc, 22x22, AGA} OCT_{ij}^{ISO \rightarrow EPID, 22x22, CGA}} \quad (12)$$

Where S_{ij}^{CGA} is the S_{ij} matrix obtained at a commissioned gantry angle (CGA, i.e., 0° , 90° or 180°) and $PV_{ij}^{proc,22x22,CGA}$ and $PV_{ij}^{proc,22x22,GAC}$ correspond to the pre-processed open images of a 22×22 cm² field at a CGA and at an arbitrary gantry angle (AGA), respectively.

$OCT_{ij}^{ISO \rightarrow EPID, 22 \times 22, CGA}$ and $OCT_{ij}^{ISO \rightarrow EPID, 22 \times 22, AGA}$ are the 2D array measurements at isocenter at d_{max} for a 22×22 cm² field, scaled to the EPID level, both at CGA and AGA, respectively. Note that this correction requires the acquisition of an EPID image and a 2D array measurement of a large field (e.g. 22×22 cm²) for each clinically relevant gantry angle, as included in **Table 1**. However, since in this study the validation of the method could only be performed with the 2D array positioned perpendicular to the beam, only data for gantries 0, 90 and 180 was acquired.

A normalization factor is applied to account for the differences in transmission leading to different dose response. Therefore, the dose response Dr is modified to fit the central region of a back-projected EPID image of a 10×10 cm² field irradiated to a slab phantom and back-projected to the isocenter at 10 cm depth, $\langle D_{ij}^{mid, 10 \times 10} \rangle_{Roi}^{CGA}$, to the dose measured with the array, $\langle OCT_{ij}^{10 \times 10} \rangle_{Roi}^{AGA}$.

$$N^{AGA} = \frac{\langle D_{ij}^{mid, 10 \times 10} \rangle_{Roi}^{CGA}}{\langle OCT_{ij}^{10 \times 10} \rangle_{Roi}^{AGA}} \quad (14)$$

The adapted Dose response is defined as:

$$Dr^{CGA \rightarrow AGA} = Dr^{CGA} N^{AGA} \quad (15)$$

Where Dr^{CGA} is the dose response of the commissioned gantry angle, and N^{AGA} is the normalization factor.

4.2.6. Validation of adaptation to arbitrary gantry angles

To validate this approach, a full commissioning of the cardinal gantry angles was performed first, and three models were created. For each of the three models, the gantry angle correction can be applied. EPID images of IMRT fields irradiated at gantry 90° were back-projected using the model commissioned at gantry 0° , EPID images irradiated at gantry 180° were back-projected using the model commissioned at gantry 90° and EPID images acquired at gantry 0° were back-projected using the model of gantry 180° . The back-projected 2D dose distributions of the 25 IMRT beams were compared to the original array measurements of gantry angles 90° and 180° and 0° , respectively.

4.3. Results

4.3.1. Validation of the algorithm

The performance of $K_{ij}^{MRI \rightarrow EPID}$, K_{ij}^{EPID} and K_{ij}^{prof} , which correct for the presence of scatter at the EPID level, can be seen in **Figure 4.2**, where EPID measured output factors before and after fitting to the IC measurements at isocenter, are shown. **Figure 4.3** presents the normalized EPID X profiles before and after applying the scatter kernels K_{ij}^{prof} , K_{ij}^{EPID} and $K_{ij}^{MRI \rightarrow EPID}$, compared to the measured dose profile with the detector array at isocenter at d_{max} , after scaling to the EPID level.

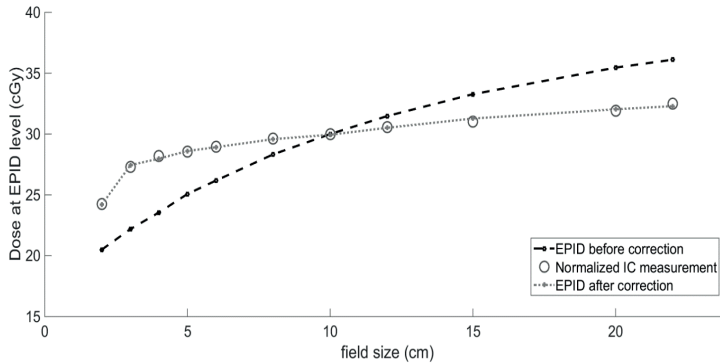


Figure 4.2: Output factors measured with the 1500 OCTAVIUS detector array, (open circles) and EPID (lines). The normalized central pixel dose of the EPID before scatter correction is plotted in dashed black. After applying the scatter kernels K_{ij}^{EPID} and K_{ij}^{MRI} , the EPID signal corrected for the scatter is derived (dotted grey line). Note that due to possible small misalignments, to the spatial resolution of the detector used in this study (1500 OCTAVIUS array) and the size of the ionization chambers, for small fields (e.g. $2 \times 2 \text{ cm}^2$) the measured dose on-axis might be underestimated.

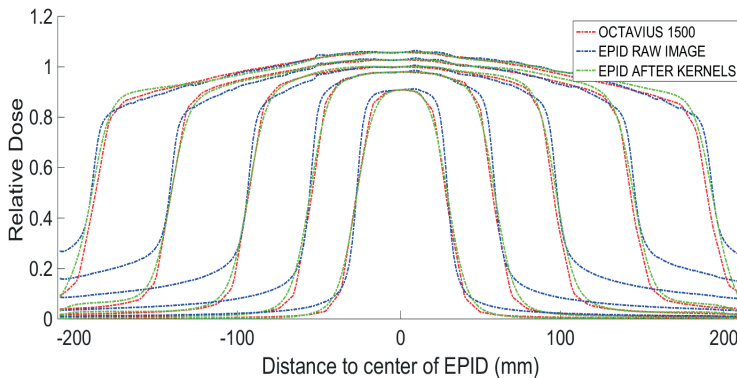


Figure 4.3: X profiles of the raw (dashed blue) and after convolving with the scatter kernels (dashed green) EPID images for 3×3 , 5×5 , 10×10 , 15×15 and $20 \times 20 \text{ cm}^2$ square fields, compared to the profiles measured with the OCTAVIUS 1500 array (red).

4.3.2. IMRT beams at gantries 0° , 90° and 180°

25 IMRT fields from three treatments (2 prostate, 1 rectum) were verified for the three commissioned gantry angles. An arbitrary subset of γ maps

of these fields comparing detector array and EPID reconstructed dose distributions is shown in **Figure 4.4**. **Table 4.2** reports the average and standard deviation of three parameters: γ -mean, γ -pass rate and dose difference at the reference point (ΔDose_{RP}).

Table 4.2: Averaged γ results and dose difference at a reference point for 25 IMRT fields at gantry 0° , 90° and 180° .

Gantry angle	$\langle \gamma_{mean} \rangle$	$\langle \text{Passrate } \%_{\gamma < 1} \rangle$	$\langle \Delta\text{Dose}_{RP} \rangle$
0	0.37 ± 0.07	97.9, 95% CI [96.7, 99.1]	$-0.8\% \pm 1.8\%$
90	0.36 ± 0.09	98.1, 95% CI [97.5, 99.3]	$-0.3\% \pm 1.9\%$
180	0.37 ± 0.06	97.9, 95% CI [97.2, 98.7]	$-0.5\% \pm 1.7\%$

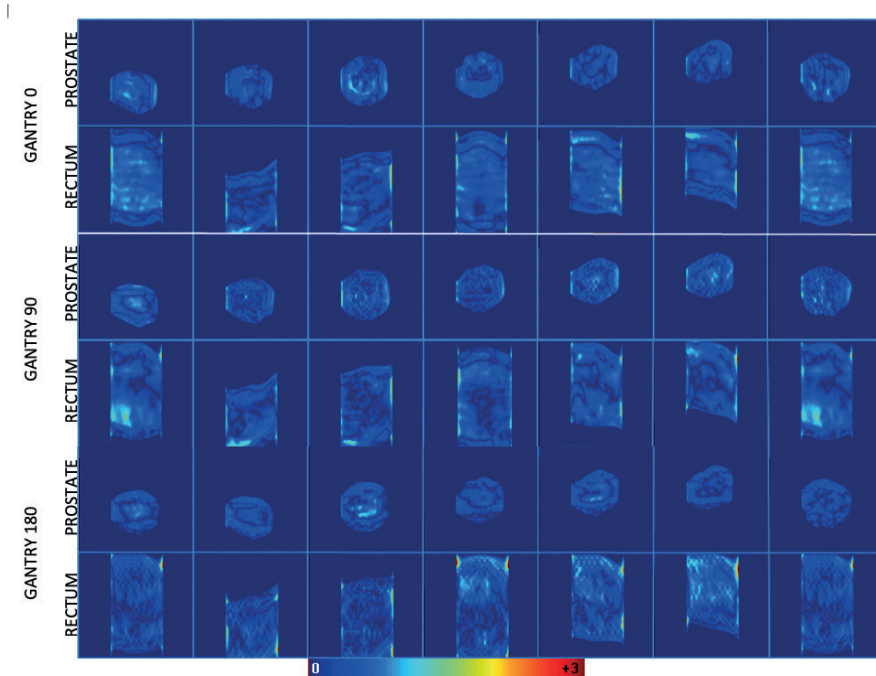


Figure 4.4: The first 2 rows show a random subset of γ maps (3%, 2mm, global 10% isodose) for 7 prostate plans and 7 rectum plans irradiated at gantry 0° . Rows 3 and 4 show the γ maps for the same rectum and prostate plans irradiated at 90° degrees. The last two rows are the γ maps for the same fields irradiated at and 180° .

A sample of X and Y profiles of both EPID and array measured dose distributions at gantries 0° , 90° and 180° is presented in **Figure 4.5**, where the reference point is also indicated for each image.

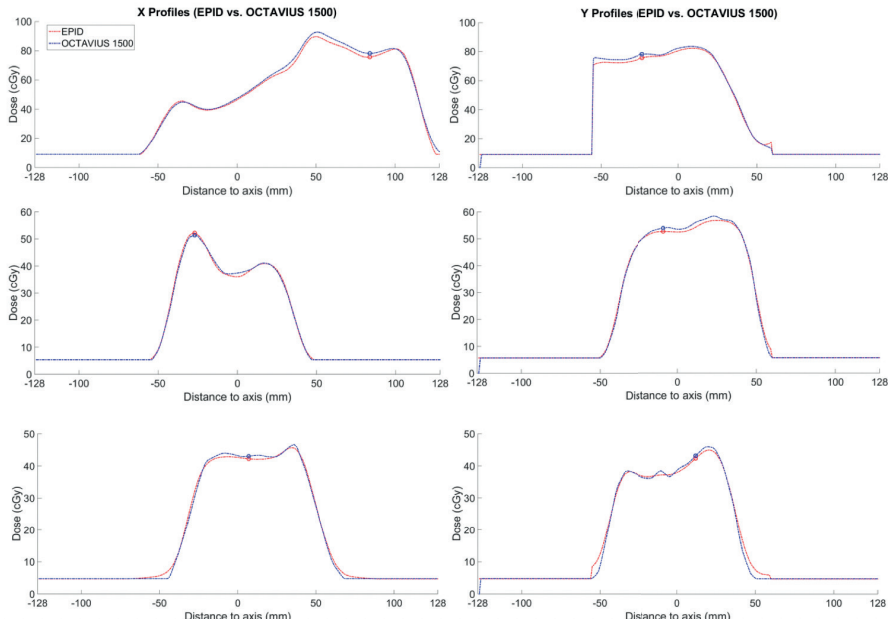


Figure 4.5: X (left) and Y (right) EPID and measured array profiles for one prostate IMRT field (first row) and two rectum (second and third rows) IMRT fields irradiated at gantry angles 0° (first row), 90° (second row) and 180° (third row). EPID profiles are plotted in dashed red and array profiles in dashed blue. The blue and red circles determine the reference point where the dose difference was calculated. Note in the Y profile of the prostate beam, that the signal of both EPID and array measured dose distributions were truncated at ± 5.6 cm.

4.3.3. Gantry angle dependency validation

The same EPID images acquired for the 25 IMRT fields at three gantry angles were used to validate the gantry angle correction method. The 25 images acquired at gantry angle 90° were back-projected using the model commissioned at gantry angle 0. Similarly, EPID images acquired at gantry angle 180° were back-projected using the model of

gantry angle 90° and EPID images acquired at gantry angle 0° were back-projected using the model of gantry angle 180° . Dose difference at reference point and γ results are reported for the comparison to detector array measurements. **Figure 4.6** shows the γ maps for the same fields as in **Figure 4.4**, in this case using the gantry angle correction. **Table 4.3** reports the averaged γ -mean and γ -pass rate together with the dose difference at a reference point (ΔDose_{RP}).

Table 4.3: Average γ results and dose difference at a reference point for 25 IMRT fields acquired at gantry 0° , 90° and 180° , using the gantry adaptation solution and the models of gantries 180° , 0° and 90° as a baseline, respectively.

Measurement / model gantry angle	$\langle \gamma_{mean} \rangle$	$\langle \text{Passrate } \%_{\gamma < 1} \rangle$	$\langle \Delta\text{Dose}_{RP} \rangle$
$0^\circ / 180^\circ$	0.39 ± 0.07	97.9, 95% CI [97.7, 99.0]	$-0.5\% \pm 2.1\%$
$90^\circ / 0^\circ$	0.37 ± 0.08	98.4, 95% CI [97.3, 98.9]	$-0.3\% \pm 1.8\%$
$180^\circ / 90^\circ$	0.39 ± 0.07	97.9, 95% CI [96.5, 98.3]	$0.5\% \pm 1.7\%$

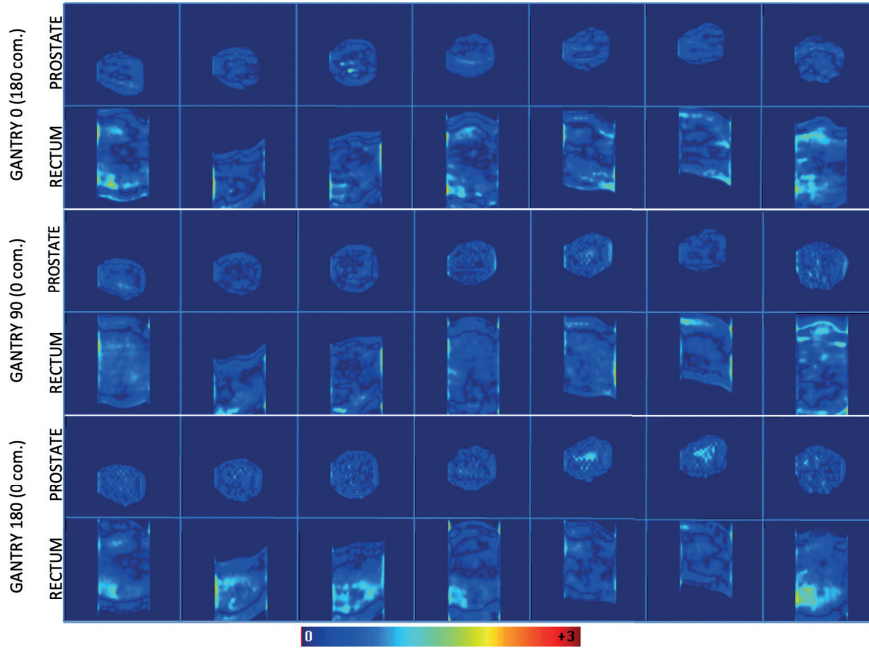


Figure 4.6: The first 2 rows show a subset of γ maps (3%, 2mm, global 10% isodose) for 7 prostate plans and 7 rectum plans irradiated at gantry 0° and reconstructed using the gantry angle correction from $180 \rightarrow 0$. Rows 3 and 4 show the γ maps for the same rectum and prostate plans irradiated at 90 degrees and reconstructed using the correction $0 \rightarrow 90$. The last two rows are the γ maps for the same fields irradiated at and 180 degrees and reconstructed using the correction $90 \rightarrow 180$.

4.4. Discussion

We successfully adapted our EPID dosimetry back-projection algorithm to the MR-linac geometry. Comparison of EPID reconstructed and IC measured 2D dose distributions at isocenter level show good correspondence. This proof of concept study demonstrates that for three cardinal gantry angles, the algorithm is able to reconstruct the dose distribution inside a slab phantom accurately. Furthermore, a method is introduced to correct for the gantry angle dependent

attenuation of the cryostat, couch and bridge, and was validated for gantry angles 0° , 90° and 180° . Validation of this correction for arbitrary angles is beyond the scope of present work, as it involves IC array measurements that, with our current equipment, can only be performed at the cardinal angles. In future work, when expanding the method to all gantry angles, attenuation of the couch, bridge and the cryostat pipe will have to be taken into account in the back-projection algorithm. A method to correct for the influence of these structures will have to be developed and tested and the accuracy of such a method will have to be assessed.

The results presented in Table 4.2 suggest a minor underdosage in EPID reconstructed dose. This can also be observed in some of the graphs in Figure 4.5. To further determine whether this underdosage is systematic or not, more data would be required. An estimate of the uncertainty, obtained from the standard deviation of the reconstruction point doses of the 25 IMRT fields (Table 2 and 3), is 2% (1 SD).

The comparison between the EPID reconstructed and IC array measured dose distributions disregard any possible dose re-distributions caused by the magnetic field inside the phantom due to the electron return effect (ERE). Our algorithm at this stage does not account for these effects. In this work, however, no inhomogeneities are present in the phantom geometry. And given the spatial resolution of the Octavius 2D array, we expect the impact of these effects to be negligible. Moreover, no skewness was observed in the S_{ij} matrix. Furthermore, the EPID measurements were fitted to array measurements performed in a 1.5T B-field and the EPID reconstructed dose was compared to dose distributions measured in a 1.5T B-field, both showing good agreement.

In the patient geometry, however, the ERE might lead to important dose redistributions. So, it is expected that for EPID in vivo dosimetry

the current solution will fall short. EPID dosimetry can be a valuable tool for the detection of gross errors in the patient and for the detection of smaller deviations in situations where the effect of ERE is small. For instance, virtual in air EPID measurements⁸⁸ can be used to reconstruct EPID dose distributions to a phantom anatomy, instead of OCTAVIUS measurements which are more cumbersome by nature.

Several solutions can be thought of to solve this problem. First is the comparison of the EPID back-projected dose distribution to a copy of the planned dose distribution calculated without the magnetic field (i.e., a ‘non-magnet’ solution, similarly to the ‘in-aqua’ concept used for verification of lung treatments⁸⁶). Alternatively, the back-projection algorithm could be modified to reconstruct the fluence in a plane before the patient and use it as input for a Monte Carlo dose calculation which accounts for the magnetic field, which can then be compared to the planned dose distribution. These approaches would, however, imply the use of a dose calculation engine, which would hamper fast computations in the verification process. The chosen technique to solve this problem is out of the scope of this work.

As with our conventional algorithm, the parameters of the model are determined using water-based kernels and consequently, the model is expected to work most accurately for back-projection in homogeneous media (such as slab phantoms or the abdomen or pelvis. For dose verification in sites involving (large) tissue heterogeneities, e.g. lung, esophagus and breast, the same in aqua vivo approach as in the conventional algorithm can be used⁸⁶. The performance of this approach will be assessed in future work

Only pelvic treatments were included in this study. However, we expect the performance of the adapted back-projection algorithm to be treatment site independent⁹⁰. Validation of the method in clinical practice falls outside the scope of this study.

Another limitation when using the EPID for dosimetry in the MR-linac in the current setup is that parts of beams exceeding 8.1 cm in the cranial direction cannot be detected due to the non-centered position of the panel. As a result, for treatments with large fields parts of the reconstructed dose distribution will be missing, and cannot be verified. Due to the design of the MR-linac, alignment of the panel with the beam is not straightforward.

The extra attenuation of the beam by the cryostat outside the window ± 5.6 cm in the longitudinal direction is another limitation of the MR-linac geometry and was not dealt with in current work. However, we are positive that the available signal in these strongly attenuated areas can be used for dosimetry purposes, although the accuracy of the final reconstructed dose distribution inside the phantom or patient will probably be lower. Overall, we observed that the verification of the treatments will be constrained by the size of the irradiated beams and therefore the accumulated EPID reconstructed dose distribution may not be possible for certain target volumes. In clinical practice this limitation does not play a role for prostate and all stereotactic treatments. For treatments with field sizes exceeding the aforementioned window, we anticipate a hybrid approach with highest accuracy in the central region, and lower accuracy in the peripheral area.

In this proof of concept, EPID-based dose reconstruction at the isocenter plane is presented as a QA tool for the MR-linac in 2D. Future work includes the adaptation of this method to allow for 3D dose reconstructions for any gantry angle and comparison to planned dose distributions.

4.5. Conclusions

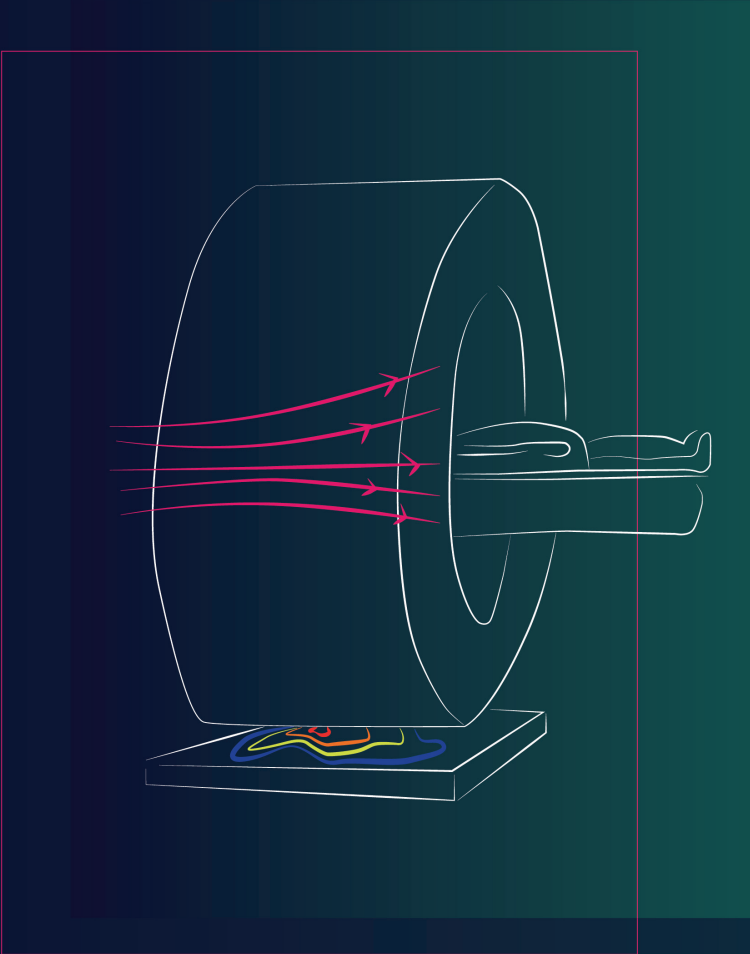
Our EPID dosimetry back projection algorithm was successfully adapted for the MR-linac geometry, accounting for the presence of the MRI housing between phantom (or patient) and EPID. Both the attenuation of the cryostat and the scatter from the cryostat reaching the panel were successfully modelled. The algorithm was commissioned at three gantry angles: 0, 90 and 180 degrees. Excellent agreement was found for 25 IMRT beams between IC measured and EPID reconstructed 2D dose distributions in a phantom positioned at the isocenter. Moreover, a solution is presented for the gantry angle dependence of the attenuation of cryostat, couch and bridge. Validation of this method using data measured at a certain cardinal angle, but back-projected using the model from another angle, again showed excellent agreement. This work is an essential step towards an accurate and independent integrated dose verification tool for the MR-linac.

4.6. Disclosure of conflicts of interest

Support for this research was provided, in part, by Elekta AB, Stockholm, Sweden.

4.7. Acknowledgments

We would like to thank Jochem Kaas, Thijs Perik and Begoña Vivas for assistance with the measurements.



5.

3D DOSIMETRIC VERIFICATION OF UNITY MR-LINAC TREATMENTS BY PORTAL DOSIMETRY.

**Iban Torres-Xirau
Igor Olaciregui-Ruiz
Jochem Kaas
Marlies E. Nowee
Uulke A. van der Heide
Anton Mans**

Department of Radiation Oncology,
The Netherlands Cancer Institute–Antoni van Leeuwenhoek Hospital,
Plesmanlaan 121, 1066 CX Amsterdam, The Netherlands

*Radiotherapy and Oncology, Volume 146, Number 9, Pages 161-166
Published March 2020 • © 2020 The Green Journal*

Abstract

3D dosimetric verification of online adaptive workflows is essential as their complexity is unprecedented in radiation oncology. The aim of this work is to demonstrate the feasibility of back-projection portal dosimetry for 3D dosimetric verification of Unity MR-linac treatments.

An earlier presented 2D back-projection algorithm for the Unity MR-linac geometry was extended for 3D dose reconstruction and comparison against planned dose distributions. ‘In-air’ as well as *in-vivo* portal EPID images can be used as input. The method was validated using data from treatments of 5 patients (2 rectal, 2 prostate cancer and one oligo metastasis). 3D pre-treatment verification of the reference plan using ‘in-air’ EPID images was performed and compared against planned and measured (with the Octavius 4D system) dose distributions. EPID reconstructed and planned dose distributions were compared for the first three adaptations of all treatments. For all comparisons, dose difference values at the reference point and γ -parameters (3%, 3 mm, global, in 50% isodose surface) were reported.

Pre-treatment verification against TPS data showed $y_{\text{mean}} = 0.41 \pm 0.04$ and $y_{\text{passrate}} = 98.4 \pm 0.1$, and $\Delta\text{Dose}_{\text{RP}} = -1.2 \pm 1.3$. The comparison against the OCTAVIUS 4D system showed $y_{\text{mean}} = 0.37 \pm 0.09$ and $y_{\text{passrate}} = 97.4$, 90% CI [95.2, 99.7], and $\Delta\text{Dose}_{\text{RP}} = -1.4 \pm 1.2$. The averaged y -results for the *in-vivo* 3D verification were $y_{\text{mean}} = 0.45 \pm 0.09$ and $y_{\text{passrate}} = 91.5 \pm 3.1$, and $\Delta\text{Dose}_{\text{RP}} = -1.4 \pm 1.2$.

3D dosimetric verification of Unity MR-linac treatments using portal dosimetry is feasible, pre-treatment as well as *in-vivo*.

Keywords: MR-linac; Unity; EPID dosimetry; portal dosimetry; 3D dosimetry; QA; *in-vivo*

5.1. Introduction

Recently, treatment machines combining a radiation source with an MRI system have been developed and are clinically introduced. The Unity MR-linac (Elekta AB, Stockholm, Sweden) ^{91,92} combines a linear accelerator with a 1.5 T MRI scanner, and is equipped with an Electronic portal imaging device (EPID) mounted on the gantry, opposite to the accelerator head, allowing for simultaneous beam irradiation, EPID acquisition and MR imaging ⁹³.

The use of EPIDs as dosimeters has been extensively studied ^{113,114,138,140–143,158}, and their applicability for dosimetric applications has been acknowledged for pre-treatment and *in-vivo* verification of both intensity-modulated radiation therapy (IMRT) ^{24,58,60,144–147} and volumetric arc therapy (VMAT) ^{59,69,149,150}.

In the Unity MR-linac, daily adaptation to patient position variations is not done by couch translations but by online replanning. In this way, patient anatomy changes can be taken into account by contour changes ^{94–96}. Due to the complexity of these workflows, the availability of tools for independent dosimetric verification is essential. Dosimetric verification of reference and daily adapted plans is usually performed using the combination of an MR compatible detector array and phantom. However, the use of these tools is typically time-consuming as cumbersome detector setup procedures are required. ^{97–100}. As a result, in most clinics dosimetric verification is limited to a few treatment fractions. Alternative patient-specific QA solutions have also been developed, such as fast sanity checks on the adapted plan ¹⁰¹, geometric accuracy of the delivered dose using *in-vivo* EPID images ¹⁵², or the use of independent calculations fed with linac log files ^{76,154,155,159,160}. These checks allow for real-time patient-specific QA that can cover most of the treatment chain, but still rely on the correct output of the machine

to generate the log files ¹⁰⁵, and on a correct morph of the daily MRI into a synthetic CT (MRCAT) ¹⁰²⁻¹⁰⁴. On the Unity system to date one of the workflows involves a density override of structures delineated on MRI scans. This presents a new element in the radiotherapy chain, which has not gone through extensive clinical validation yet, and which is not verifiable using log file based approaches.

Pre-treatment portal dosimetry using ‘in-air’ measurements avoids time consuming detector setup procedures as the panel is mounted on the gantry. *in-vivo* portal dosimetry provides a dosimetric end-to-end check of the online adaptation workflow making use of data acquired during treatment, i.e., without extra measurement time. Errors related to data transfer, dose delivery, patient set-up, MLC calibration, dose calculation ¹⁰⁵, and pseudo-CT determination or density assignment can be detected. To our knowledge, portal dosimetry is the only measurement-based method for verification of pseudo-CT creating from MR data. Furthermore, portal dosimetry methods have the potential to be extended to trailing and gating techniques ^{89,133}.

It has been shown that the dosimetric characteristics of the EPID in the Unity MR-linac are similar to conventional linacs ^{156,161}. Furthermore, we have shown that 2D back-projection portal dosimetry is feasible for the Unity MR-linac ¹⁶². The aim of this study is to extend the portal dosimetry method to 3D dose reconstruction for both pre-treatment using ‘in-air’ measurements and *in-vivo* verification

5.2. Materials and methods

Experimental set-up

The Unity MR-linac system consists of a 7 MV flattening filter free (FFF) beam linear accelerator mounted on a ring-based gantry, built around a wide bore 1.5 T MRI scanner (Philips Medical Systems, Best,

the Netherlands). On the opposite side of the accelerator, the EPID (XRD 1642 AP, Perkin Elmer Optoelectronics, Wiesbaden, Germany) is also mounted on the ring gantry. The central region of the cryostat is designed free of gradient coils and shimming hardware, allowing for minimal and homogenous attenuation of the beam by the cryostat. The dimension of this free-of-coils region determines the size of un-attenuated beams received by the EPID, allowing for a maximum field size at the isocenter of $X=\pm 11$ cm and $Y=\pm 4.8$ cm. Note that the EPID was included in the system for the purposes of machine QA and not for patient imaging or Portal Dosimetry, and it lies in a non-centered position with respect to the beam axis. As a result, beams can only be completely captured if their field size at isocenter is smaller than $X=\pm 11$ cm, $Y=[-11, +8]$ cm.

Images were acquired using Elekta's MVIC software. Array measurements were performed using an MR-compatible OCTAVIUS 1500 2D detector array (PTW, Freiburg, Germany), which has 1405 vented ICs with 7.1 mm center-to-center distance. For back-projection of the EPID images to the patient or phantom geometry, a research version of the IViewDose software (Elekta, AB, Stockholm, Sweden) was used.

Modifications to the model

The presented work builds on the back-projection algorithm described previously^{58,70}. The first steps of adapting this method to the Unity MR-linac geometry have already been presented in previous studies^{139,156,162}, showing that 2D dose reconstruction in a plane through the isocenter parallel to the EPID is possible. The steps needed for implementing 3D *in-vivo* dose reconstructions are described below.

First, the algorithm was fully commissioned at gantry angle 0° , by fitting EPID data to IC measurements for different setups.

Second, the adapted gantry angle (AGA) solution for the back-projection presented in ¹⁶² was applied for the 26 gantry angle values clinically in use at the time of this study. For each gantry angle value, a sensitivity matrix was obtained by combining EPID images with 2D array measurements made at isocenter inside the OCTAVIUS rotating phantom for a 22x22 cm² field. Additionally, the gantry angle dependent cryostat attenuation factor was determined by fitting a back-projected 10x10 cm² square field at isocenter to the dose determined using the TPS.

Third, the extension from 2D to 3D dose distributions was performed similar to ⁵⁸ by reconstructing the dose within the patient or phantom volume in multiple planes parallel to the EPID, obtaining the 3D dose distribution for each beam.

Fourth, the software was extended to read 3D planned dose distributions allowing for the verification of clinical plans in the patient CT, accounting for adaptations ¹⁶³ in the current Unity MR-linac workflow.

Fifth, the use of virtual dose reconstruction ⁸⁸ was implemented in the software allowing for 3D dose reconstruction in any geometry from 'in-air' portal images. This made pre-treatment verification possible eliminating the need using a phantom or IC array.

Finally, the parts of the beams exceeding the coil-free region of ± 4.8 cm on the cranial-caudal direction were removed, using a masking pyramid (**Figure 5.1**) per beam to both the EPID back-projected and TPS dose distributions. For all beams combined, this results in a cylinder mask in the accumulated 3D dose distribution, offering a valid comparison only in the volume where EPID images receive usable information.

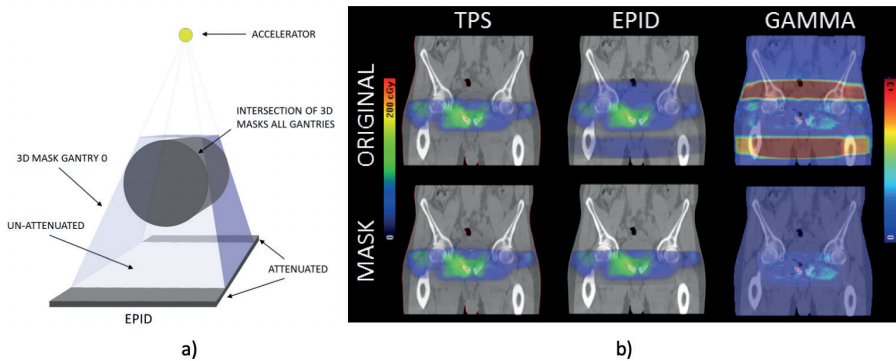


Figure 5.1: a) The EPID image is divided into the central area in which the radiation reaching the panel is minimally attenuated and the outer areas where the non-coil-free region of the cryostat causes increased attenuation. A mask is applied to the EPID reconstructed and planned dose distributions. The intersection of all masking pyramids per beam results in a cylinder per fraction. Only the un-masked volume is taken into account in the γ -evaluation. b) Planned dose, EPID reconstructed dose and γ -distributions, both without (upper row) and with the mask (lower row) applied.

Plan verification

Data from treatments of five patients were used (2 rectal-, 2 prostate cancer and one lymph node oligo metastasis patient, with 9 to 12 step-and-shoot IMRT beams). For 3D pre-treatment verification, the virtual EPID dose reconstruction of the reference plan in the OCTAVIUS phantom geometry was compared both to the array and to the TPS dose distributions calculated on the phantom geometry. The virtual EPID dose reconstruction of the reference plan was also calculated in the patient geometry and compared to the corresponding TPS patient dose distribution. For all analyses, dose difference at the reference point (ΔD_{RP}), and γ results (3%, 3 mm, 50% isodose) were reported. The isocenter was used as reference point for the OCTAVIUS phantom. The center of the PTV was used as reference point in patient dose reconstructions. For 3D *in-vivo* verification, EPID data of the first three daily adapted plans were acquired. The EPID reconstructed dose distributions were compared to their corresponding plan of the day, by

γ -analysis both in 2D per beam (3%, 3 mm, 20% isodose), and in 3D per fraction (3%, 3 mm, 50% isodose). The differences in dose value at the center of the PTV (ΔD_{PTV_C}) were also reported.

5.3. Results

Table 5.1 displays the averaged phantom pre-treatment verification results of the 5 reference plans (per site and total). Note that rectum cases present slightly worse agreement than prostate and oligo treatments.

Table 5.1: Average and standard deviation of γ -parameters (γ_{mean} , γ_{passrate}) and dose difference at reference point (ΔD_{RP}), in the comparison of virtual EPID dose distributions with both Octavius and TPS dose distributions calculated in the Octavius phantom geometry.

Site	Rectal cancer (2)	Prostate cancer (2)	Oligo metastasis (1)	Total
γ_{mean}	0.46 \pm 0.04 / 0.45 \pm 0.08	0.28 \pm 0.03 / 0.33 \pm 0.02	0.34 / 0.45	0.37 \pm 0.09 / 0.40 \pm 0.07
γ_{passrate} (%)	93.7 \pm 0.3 / 94.2 \pm 3.5	99.9 \pm 0.0 / 99.8 \pm 0.1	99.4 / 99.2	97.4, 90% CI [95.2, 99.7] / 97.4, 90% CI [94.9, 99.9]
ΔD_{RP} (%)	-1.4 \pm 0.1 / -2.8 \pm 0.4	-0.7 \pm 1.0 / -0.1 \pm 2.1	-0.9 / 0.8	-1.4 \pm 1.2 / -1.0 \pm 2.0

Figure 5.2 shows pre-treatment 3D dose and γ distributions calculated in the Octavius phantom geometry for a reference prostate cancer case. Additionally, A-P and L-R profiles are also shown.

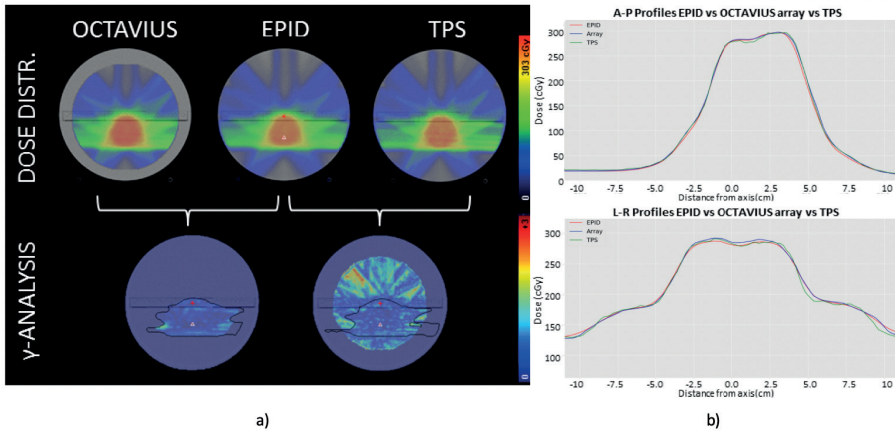


Figure 5.2: a) 3D Octavius, virtual EPID reconstructed and TPS dose distributions calculated in the Octavius phantom geometry with their corresponding γ -comparisons (3%, 2mm, global) for a prostate reference plan. The black line indicates the volume where the γ -statistics were calculated. b) A-P and L-R profiles through the isocenter are shown for the dose distributions.

Pre-treatment verification in the patient geometry using the virtual method is presented in **Figure 5.3** for a lymph node oligo metastasis treatment. In the comparison of virtual EPID with TPS dose distributions, the averaged γ -parameters of the combined results for the 5 reference plans were $\gamma_{\text{mean}} = 0.41 \pm 0.04$ and $\gamma_{\text{passrate}} = 97.9 \pm 1.7$, with an average dose difference at the center of the PTV (ΔD_{PTV}) of $-0.9\% \pm 0.9\%$. These results compare to the agreement in phantom pre-treatment verification.

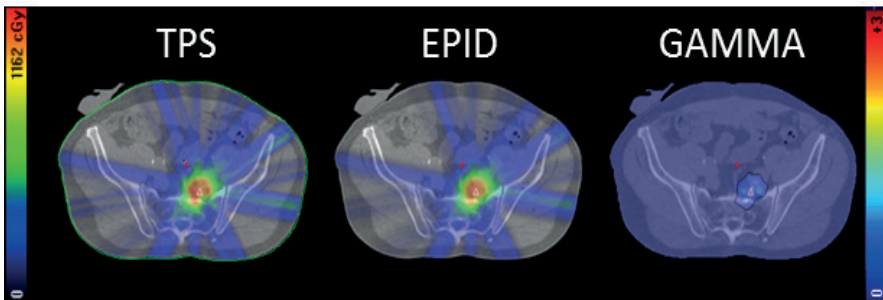


Figure 5.3: Planned and virtual EPID reconstructed dose distributions and the corresponding γ -evaluation (3%, 2mm, global) for the oligo metastasis reference plan in

the patient geometry. The color scale on the left, ranging from 0 to 1162 cGy, indicates the dose level for the TPS and EPID dose distribution maps. The color bar on the right, ranging from 0 to +3, indicates the γ values for the γ -map on the right figure, comparing TPS to EPID.

For the first three adapted fractions of 5 patients, **Table 5.2** presents averaged γ -parameters (γ_{mean} , γ_{passrate}) and dose difference at center of the PTV (ΔD_{PTV}) of the *in-vivo* verification for both the 3D per fraction and the 2D per beam analysis. As expected, *in-vivo* verification shows slightly worse agreement than pre-treatment, due to extra uncertainties in the patient anatomy during the actual treatment.

Table 5.2: γ -parameters (γ_{mean} , γ_{passrate}) and dose difference at the reference point ($\% \Delta D_{\text{RP}}$) for the γ -analysis (3%, 2mm, global) in 2D per beam and in 3D per fraction, averaged over the first three fractions for the 5 patients, presented per site and total. Results are presented as average \pm 1SD.

Site	Rectum (2)	Prostate (2)	Oligo metastasis (1)	Total
2D per beam Comparison EPID vs. TPS				
γ_{mean}	0.63 \pm 0.14	0.56 \pm 0.15	0.58 \pm 0.12	0.59 \pm 0.14
γ_{passrate} (%)	80.0, 95% CI [77.7, 82.4]	84.3, 95% CI [81.7, 87.0]	84.6, 95% CI [81.7, 87.5]	82.7, 95% CI [81.2, 84.3]
ΔD_{PTV} (%)	-1.4 \pm 6.3	0.9 \pm 6.2	3.7 \pm 6.5	0.5 \pm 6.6
3D per fraction Comparison EPID vs. TPS				
γ_{mean}	0.56 \pm 0.04	0.48 \pm 0.05	0.52 \pm 0.02	0.52 \pm 0.05
γ_{passrate} (%)	88.4, 95% CI [85.2, 91.6]	95.2, 95% CI [92.1, 98.3]	95.3, 95% CI [92.9, 97.7]	92.5, 95% CI [90.2, 94.8]
ΔD_{PTV} (%)	-0.8 \pm 1.2	0.9 \pm 1.2	3.9 \pm 1.3	0.8 \pm 2.1

Note that for the oligo metastasis fractions, a somewhat large dose difference in the PTV is reported. It was observed that the center of the PTV corresponded to areas of high gradient, γ -parameters showed excellent agreement.

Figure 5.4 shows axial planes of 3D γ -distributions corresponding to the *in-vivo* verification of the first three adapted fractions of a prostate treatment.

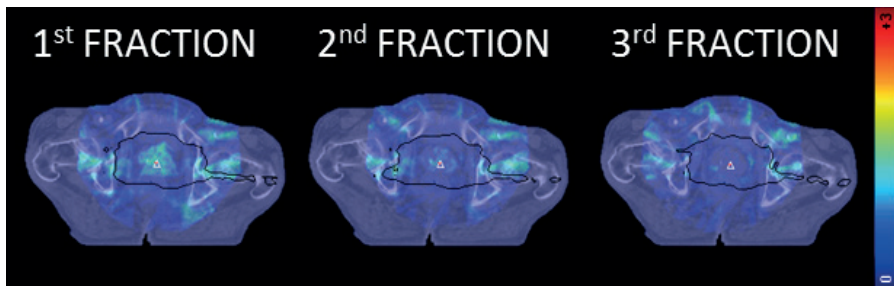


Figure 5.4: Axial planes of the 3D γ distributions (3%, 2mm, global) of the first, second and third adaptations of a prostate plan. The color scale on the right, ranging from 0 to +3 indicates the γ intensity of the 3 γ -maps.

5.4. Discussion

In this study, we have presented a method for pre-treatment and *in-vivo* 3D dosimetric verification of Unity MR-linac treatments using portal dosimetry. Treatment plans of 5 patients (3 treatment sites) were used. Comparison of the 3D back-projected EPID dose to IC array measurements using dedicated phantoms, as well as TPS dose distributions showed excellent agreement for the 5 reference plans. Moreover, the *in-vivo* results also showed good agreement when compared to the TPS for the first 3 adapted fractions. This demonstrates the feasibility of pre-treatment and *in-vivo* portal dosimetry for dosimetric verification of Unity MR-linac treatments.

The extra attenuation of the beam by the MR housing outside the window (of ± 4.8 cm) in the longitudinal direction is the main limitation of the presented work, impeding the complete dosimetric verification for large target areas. However, we believe that the available (strongly attenuated) signal outside the window can be used for dosimetry purposes, although the accuracy of the final reconstructed dose distribution might be lower. Nonetheless, many of the errors that EPID dosimetry can mitigate may not necessarily require the reconstruction of the full frame as they would be alerted already in the back-projected dose distribution of the central part of the frame.

An intrinsic limitation when using the EPID for dosimetry in the MR-linac in the current setup is that parts of beams exceeding 8.1 cm in the cranial direction cannot be detected due to the non-centered position of the panel. As a result, for treatments with large fields parts of the reconstructed dose distribution will be missing, and cannot be verified. This might also lead to a possible underestimation of scatter for large fields, as parts of the beam that originate scatter are not captured by the EPID and therefore don't contribute in the determination of the primary dose.

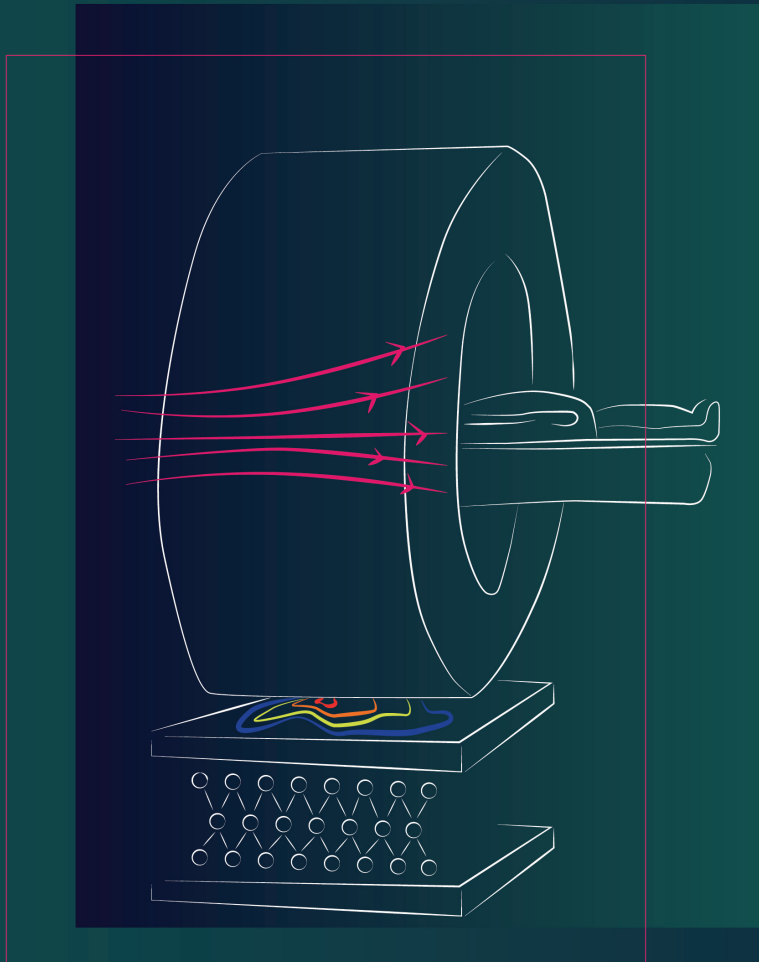
Given the complex geometry of the MR-linac, highly density structures are affecting the EPID dose reconstruction of images in which the beam traverses the bridge or the cryostat pipe, leading to less accurate dose reconstructions for certain gantry angles. In the rectum plans of this study several of these beams were present, which in combination to the underestimation of the scatter for the large fields that was only present in the rectum treatments, resulted in worse agreement in the verification of rectum plans. To further determine whether these inaccuracies could hamper the detection of errors, more data would be required.

The presented dose reconstruction method does not account for electron return effects (ERE) caused by the presence of the magnetic field. However, as there were no large inhomogeneities present in the cases studied, we presume that in the 3D dose distributions used in this study, the ERE did not play a significant role. The performance of the method for dose verification in cases with large inhomogeneities needs further investigation. Nevertheless, for a more accurate dose reconstruction taking into account the magnetic field effects, two solutions can be considered. First is the comparison of the EPID back-projected dose distribution to a copy of the planned dose distribution calculated without the magnetic field. Alternatively, the back-projection algorithm can be used to reconstruct the fluence entering the patient and use that to feed a Monte Carlo dose engine which accounts for the magnetic field.

In conclusion, our 3D EPID dosimetry back projection algorithm was successfully adapted for the Unity MR-linac geometry, accounting for the presence of the MRI housing between patient and EPID. The presented results provide the first experimental evidence that 3D EPID dosimetry is feasible for the Elekta Unity MR-linac, both pre-treatment and in-vivo. This work presents the only independent measurement-based QA solution of the entire online adaptive chain including the use of a pseudo-CT and paves the way for the development of an automated verification solution for the online adaptive workflow of the Elekta Unity MR-linac.

5.5. Disclosure of conflicts of interest

Support for this research was provided, in part, by Elekta AB, Stockholm, Sweden.



6.

A DEEP LEARNING-BASED CORRECTION TO EPID DOSIMETRY FOR ATTENUATION AND SCATTER IN THE UNITY MR-LINAC SYSTEM

Igor Olaciregui-Ruiz ^{a,*}
Iban Torres-Xirau ^{a,*}
Jonas Teuwen ^{a,b}
Uulke A. van der Heide ^a
Anton Mans ^a

Department of Radiation Oncology,
The Netherlands Cancer Institute–Antoni van Leeuwenhoek
Hospital, Plesmanlaan 121, 1066 CX Amsterdam, The
Netherlands

^b Department of Radiology and Nuclear Medicine,
Radboud University Medical Center, Geert Grooteplein Zuid 10,
6525 GA Nijmegen, The Netherlands

*Both authors contributed equally.

Abstract

EPID dosimetry in the Unity MR-Linac system allows for reconstruction of absolute dose distributions within the patient geometry. Dose reconstruction is accurate for the parts of the beam arriving at the EPID through the MRI central unattenuated region, free of gradient coils, resulting in a maximum field size of $\sim 10 \times 22 \text{ cm}^2$ at isocenter. The purpose of this study is to develop a Deep Learning-based method to improve the accuracy of 2D EPID reconstructed dose distributions outside this central region, accounting for the effects of the extra attenuation and scatter.

A U-Net was trained to correct EPID dose images calculated at the isocenter inside a cylindrical phantom using the corresponding TPS dose images as ground truth for training. The model was evaluated using a 5-fold cross validation procedure. The clinical validity of the U-Net corrected dose images (the so-called DEEPID dose images) was assessed with *in vivo* verification data of 45 large rectum IMRT fields. The sensitivity of DEEPID to leaf bank position errors ($\pm 1.5 \text{ mm}$) and $\pm 5\%$ MU delivery errors was also tested.

Compared to the TPS, *in vivo* 2D DEEPID dose images showed an average γ -pass rate of 90.2% (72.6%-99.4%) outside the central unattenuated region. Without DEEPID correction, this number was 44.5% (4.0%-78.4%). DEEPID correctly detected the introduced delivery errors.

DEEPID allows for accurate dose reconstruction using the entire EPID image, thus enabling dosimetric verification for field sizes up to $\sim 19 \times 22 \text{ cm}^2$ at isocenter. The method can be used to detect clinically relevant errors.

Keywords: Unity MR-Linac, Deep Learning, *in vivo* EPID dosimetry

6.1. Introduction

The Unity MR-Linac system offers real-time soft-tissue visualization to allow for more precise delivery and online plan adaptation ¹⁶⁴⁻¹⁶⁶. Independent quality assurance (QA) tools are required for the verification of the online adaptive strategies in magnetic resonance image-guided radiotherapy ¹⁶⁷. MR-compatible detector devices are currently employed to perform patient plan specific QA ^{97,98,100,168}. However, these solutions are typically time-consuming and not directly suitable for online adaptive workflows. Alternative solutions have been proposed, such as fast sanity checks for each adapted plan ¹⁶⁹ or the use of online independent dose calculations ¹⁵⁹. The limitation of such checks is that they verify only parts of the workflow.

For conventional linacs, Electronic Portal Image Devices (EPIDs) are commonly used as an independent end-to-end dosimetric check of the Radiotherapy (RT) chain ^{148-150,170-175}. The process can be fully automated, which is essential to reduce the number of labor-intensive and error prone tasks ⁸⁷. The Unity MR-Linac is also equipped with an EPID which is mounted on the rotating gantry, opposite to the accelerator head ¹⁵⁶. For each plan adaptation, EPID images are acquired automatically containing information about the dose absorbed by the patient. Therefore, the implementation of an automated EPID-based dosimetric verification solution for the MR-Linac adapted workflow would be within reach once EPID dosimetry becomes feasible. To that purpose, our conventional dose back-projection algorithm ^{58,176} has been adapted to the Unity MR-Linac ¹⁷⁷. The algorithm utilizes pixel values of EPID images acquired during delivery to estimate the dose delivered to the patient. Patient plan specific QA is performed by comparing EPID-reconstructed dose distributions with those calculated by the Treatment Planning System (TPS) for each adapted plan. The main limitation of the method is that dose reconstruction is only accurate for

the parts of the beam that arrive at the EPID through the MRI central unattenuated region free of gradient coils, resulting in a maximum field size of $\sim 10 \times 22 \text{ cm}^2$ at isocenter. EPID-based dosimetric verification for larger fields is currently not possible, excluding, for instance, Intensity Modulated radiotherapy (IMRT) rectum plans.

Recent advances in deep learning are highly impacting various fields in science including healthcare and medical imaging¹⁷⁸. In particular, convolutional neural networks (CNNs) have been largely applied in image detection and recognition¹⁷⁹, image segmentation¹⁸⁰, image registration¹⁸¹ or image reconstruction¹⁸². The U-Net architecture, which comprises decoder, encoder and skip-connection modules integrated in a single network, has become the de-facto standard for image segmentation¹⁸³. Recent studies have also modified the original design of the U-Net for dose prediction¹⁸⁴.

In this study, we present a Deep Learning-based method to improve the accuracy of 2D EPID reconstructed dose distributions outside the central unattenuated region, accounting for the effects of the extra attenuation and scatter. A U-Net was trained using 2D EPID and TPS dose images calculated at the isocenter inside a cylindrical phantom as training data. The goal was to use U-Net corrected dose images (the so-called DEEPID dose images) to accurately reconstruct *in vivo* 2D patient dose distributions using the entire EPID image, thus allowing for dosimetric verification of field sizes up to $\sim 19 \times 22 \text{ cm}^2$ at isocenter. The clinical validity of DEEPID was assessed with *in vivo* verification data of 45 rectum IMRT fields. To ensure that the presented Deep Learning-based method is capable of detecting clinically relevant errors, the sensitivity of DEEPID to leaf bank position errors and monitor unit (MU) errors was also tested.

6.2 Methods

6.2.1. Equipment

The Unity MR-linac system combines a 7 MV flattening filter free (FFF) beam linac (Elekta AB, Stockholm, Sweden) with an integrated wide bore 1.5 T MRI scanner (Philips Medical Systems, Best, the Netherlands)¹²⁶. An a-Si flat panel X-ray detector (XRD 1642 AP, Perkin Elmer Optoelectronics, Wiesbaden, Germany) is mounted on the ring gantry built around the MRI scanner at a fixed source-to-detector distance (SDD) of 265.3 cm, and with a detection area of 41x41 cm²¹⁵⁶, see **Fig. 6.1**. EPID images were down sampled from their original size of 1024x1024 pixels to 256x256 pixels yielding a pixel pitch of 1.6 mm. The central region of the magnet is free of gradient coils, allowing for minimal and homogenous attenuation of the beam for field sizes up to ± 11 cm in the cranial-caudal (CC) direction at isocenter (± 20.2 cm at EPID level). However, since the effective size of the beam exiting the MRI scanner is larger due to divergence, the EPID acquisition of un-attenuated beams is limited to ± 4.8 cm in the CC direction at the isocenter (± 8.8 cm at EPID level). The EPID image is therefore divided into a central region receiving un-attenuated signal and an outer region receiving signal with extra attenuation and scatter due to exceeding the free-coils region. Since the detector is displaced 5.7 cm in the cranial direction with respect to the beam axis, fields exceeding 8.1 cm in the caudal direction at isocenter plane cannot be entirely acquired by the EPID and parts of the beam fall outside the panel. After the EPID images were cropped to remove the region where beams cannot be received (> 20.5 cm in cranial direction), the size of the input EPID images for dose reconstruction was 35.3 x 41 cm² (224x256 pixels).

Plans were generated using the Monaco 5.4 (Elekta AB, Stockholm, Sweden) treatment planning system (TPS). EPID images were measured

using Elekta's MVIC acquisition software.

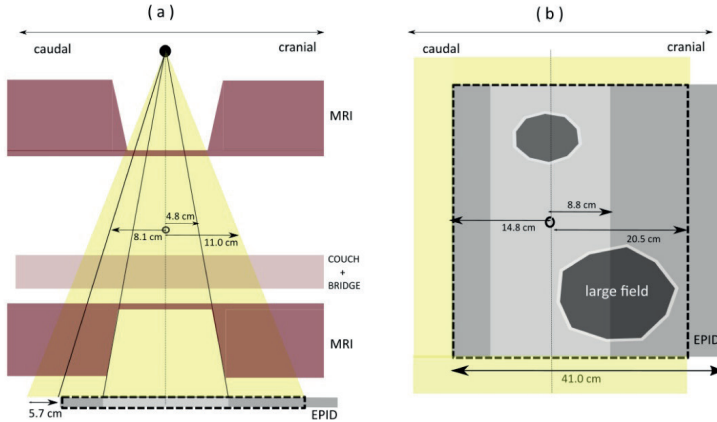


Fig. 6.1. (a) Unity MR-Linac sagittal cross section showing in yellow the maximum field size of 22 cm in the cranial-caudal (CC) direction at isocenter (black circle). The scale of the diagram has been adapted for viewing purposes. (b) Beams at the level of the EPID are received in a central unattenuated region (light grey) and in an outer attenuated region (dark grey). In the context of this study, a field is considered 'large' if the corresponding acquired EPID image contains signal in the outer region. The dashed black rectangle represents the cropped EPID image used for dose reconstruction.

6.2.2. Limitations of EPID dosimetry for large fields

For EPID dose reconstruction in this study, an adapted version of IViewDose software (Elekta, AB, Stockholm, Sweden) was used, which incorporates the adaptation of the conventional back-projection algorithm to the MR-Linac geometry¹⁷⁷. The algorithm has two modes of operation: non-transit and transit EPID dosimetry^{115,185}. In non-transit mode, *in air* EPID images acquired without a phantom/patient in the beam are utilized to reconstruct dose in any arbitrary geometry¹⁸⁶. This mode is commonly used for pre-treatment verification of the reference plan. In transit mode, EPID images acquired behind the

patient are utilized to reconstruct dose within the patient. This mode is commonly used for *in vivo* verification of adapted plans.

To illustrate the limitations of transit EPID dosimetry for large fields, square fields (5x5, 10x10, 15x15 and 20x20 cm², 100MU) were irradiated at gantry angle 0° to a 20 cm thick slab phantom consisting of 30x30x1 cm³ polystyrene slabs. Note that the measurements behind the phantom were used as a *surrogate* for *in vivo* measurements made behind the *patient*. TPS and EPID reconstructed dose profiles through the isocenter of the phantom were calculated and compared in both left-right (LR) and CC directions.

6.2.3. Deep learning architecture

Fig. 6.2 displays the U-Net architecture used in this study. A U-Net of depth 4 was used, where each down-sampling block consists of two blocks containing a convolution layer, followed by batch normalization¹⁸⁷ and a rectified linear unit (ReLU) activation function¹⁸⁸. This block was subsequently followed by a max pooling layer of size 2x2. Convolutional filters in same mode with kernel 5x5 were selected. The number of filters started at 16 and was doubled for each subsequent block. The encoder was connected to the decoder by a last layer involving two 5x5 convolution layers. At the decoder parts, the up-convolutions were concatenated with the feature maps from the same layer of the encoding path¹⁸⁹. The concatenated features followed the same sequence of convolution layers as in the decoder parts. This succession was repeated also four times. The final layer used a 1x1 convolution with a sigmoid as activation function. Each max pooling and concatenated layer was followed by a dropout layer with a drop rate of 0.3¹⁹⁰. The network was optimized using Adam¹⁹¹, an algorithm for first-order gradient-based optimization of stochastic objective functions using default values of 0.9 and 0.999 for β_1 and β_2 , respectively and a learning rate of 0.001. Mean squared error was utilized as loss

function for the training. The algorithm was trained for a maximum of 150 epochs but training could stop earlier if no improvement was found after 50 epochs. The U-Net was implemented in Python 3.6 with TensorFlow v1.7, an open source deep learning software library¹⁹². Training and evaluation of the network was performed on a GTX 1080 NVIDIA GPU. The hyperparameters of the network were tuned manually using the results of one of the cross-validation folds. As this showed the relative insensitivity to the selected hyperparameters, they were fixed for the rest of the study.

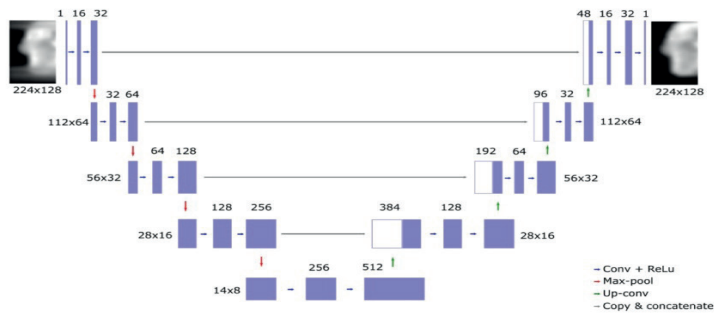


Fig. 6.2. Encoder and decoder pathways of our U-Net architecture.

6.2.4. Model training and validation

In-air EPID measurements were acquired for 90 IMRT fields corresponding to 12 adapted rectum plans of 6 patients. The *in air* EPID raw images were utilized in combination with the CT data set of the Octavius^{MR} 4D phantom (PTW, Freiburg, Germany) to reconstruct 2D EPID dose distributions at the isocenter plane in the phantom geometry using non-transit EPID dosimetry. More details regarding the employed methodology can be found elsewhere¹⁸⁵. These EPID reconstructed dose images were utilized as input data for the training.

The corresponding dose distributions recalculated by the TPS on the phantom geometry were used as ground truth, or ideal output of the U-Net. The training of the model is performed with phantom data in order to have a well-controlled environment. The use of *in vivo* dose distributions for training would be problematic as the actual delivered dose to the patient is unknown (i.e. no 'ground truth' for training). Non-transit EPID reconstructed dose distributions were chosen for training to eliminate the need for phantom positioning. The choice of the Octavius^{MR} 4D phantom was made because TPS dose calculations were already available for that geometry.

The iViewDose software stored the EPID reconstructed 2D dose images in AVS field file format (Advance Visual Systems Inc, Waltham, MA, USA). Planned dose distributions were exported from the TPS in DICOM format and imported into iViewDose to calculate 2D dose distributions at the isocenter plane which were also stored in AVS format. The AVS files were then converted into numpy arrays for network training using in-house developed python code.

Regarding data augmentation, the EPID dose images were flipped around the cranial-caudal axis first and then split into nine crops of 128x224 pixels along the same axis. A total of 1620 (90x2x18) image patches were available as training pairs (EPID, TPS) to the network. The model was evaluated using a 5-fold cross validation procedure. The evaluation was scored by comparing U-Net corrected DEEPID dose images with TPS dose images by γ -analysis using 3% of the maximum dose and 3 mm as dose-difference and distance-to-agreement criteria, respectively. The results were calculated within the region surrounded by the 10% isodose line. γ -statistics were obtained for the outer attenuated region separately.

6.2.5. *in vivo* DEEPID dosimetry

in vivo EPID images were acquired behind the patient for 45 IMRT fields corresponding to 5 adapted rectum plans of 3 patients. Approximately half of these IMRT fields were large fields. The EPID raw images were utilized in combination with the CT data set of the patient to reconstruct *in vivo* 2D EPID dose distributions at the isocenter plane in the patient geometry using transit EPID dosimetry. The resulting 2D EPID dose images were passed to the U-Net to calculate the corrected DEEPID dose images. *in vivo* EPID and DEEPID 2D dose distributions at the isocenter were then compared with TPS dose distributions by γ -analysis. γ -statistics were obtained for the central and for the outer regions separately.

6.2.6. Introduction of errors

Machine delivery errors were introduced by manual modification of the treatment prescription file before import into the record-and-verify system (MOSAIQ version 2.65, Elekta Inc., Sunnyvale, CA, USA). An adapted rectum plan was delivered correctly first and then with leaf bank position errors introduced: leaves moved 1.5 mm inwards (closing the fields) and leaves moved 1.5 mm outwards (opening the fields). Similarly, another adapted rectum plan corresponding to a different treatment was also delivered correctly first and then with an increase and a decrease in the number of MUs of 5%. *In air* EPID raw measurements were acquired for all cases and were utilized in combination with the CT data set of the patient to reconstruct 2D EPID dose distributions at the isocenter plane in the patient using non-transit EPID dosimetry. The resulting EPID 2D dose images were passed to the U-Net to calculate the corrected DEEPID dose images.

6.3. Results

6.3.1. Limitations of EPID dosimetry for large fields

Fig. 6.3 displays TPS and EPID-reconstructed dose profiles through the isocenter in a phantom for four square fields. In the LR direction, the agreement was good for all field sizes. In the CC direction, however, for the 10x10 cm² and 15x15 cm² fields there was an overestimation of the EPID reconstructed dose outside the field. For the 15x15 cm² field, there was an underestimation of the EPID reconstructed dose inside the field. The agreement was again good for the 20x20 cm² field, see discussion section for more details.

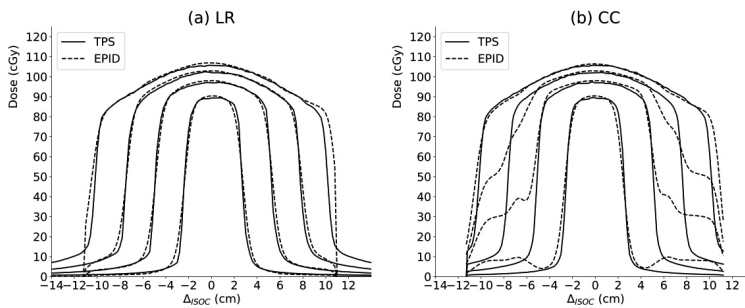


Fig. 6.3. LR and CC profiles of EPID-reconstructed and TPS dose distributions through the isocenter in a 20cm thick slab phantom consisting of 30x30x1 cm³ polystyrene slabs for four representative square fields (5x5, 10x10, 15x15 and 20x20 cm², 100MU).

6.3.2. Model validation

Fig. 6.4.a illustrates the results of the 5-fold cross validation by presenting boxplots of γ -pass rate values for each fold calculated for the outer attenuated region only. The average median and interquartile range (IQR) values were $91.9 \pm 1.3\%$ (1SD) and $8.2 \pm 1.7\%$ (1SD), respectively. For comparison, **Fig. 6.4.b** presents the corresponding results obtained with EPID dosimetry before the DEEPID correction. The average

γ -pass rate values corresponding to the results of all folds combined were 91.6% (80.7%-100%) and 42.2% (4.9%-98.3%), for DEEPID and EPID respectively. Over the entire field, the average γ -pass rate values were 92.2% (80.8%, 99.6%) and 76.4% (51.7%,98.9%), for DEEPID and EPID respectively.

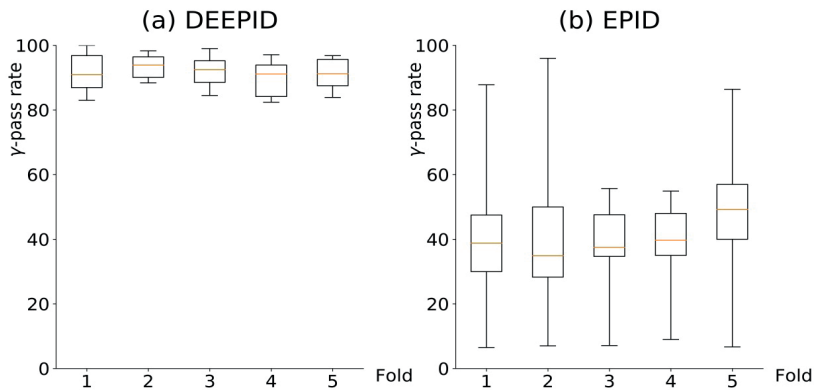


Fig. 6.4. 5-fold validation results presented as boxplots of γ -pass rate values corresponding to the comparison for the outer attenuated region between TPS dose distributions with (a) U-Net corrected DEEPID dose images and (b) EPID dose images before the correction. The box extends from the lower to upper quartile values of the data, with a line at the median. The whiskers are set at the 5th and 95th percentiles of the data. Outliers are not shown.

6.3.3. In vivo DEEPID dosimetry

Table 6.1 presents the results of the comparison between DEEPID and EPID with TPS dose distributions corresponding to the *in vivo* verification of 45 rectum IMRT fields. The agreement between DEEPID and TPS was similar for the central attenuated and the outer unattenuated regions. This can be also observed in the example presented in **Fig. 6.5** where *in vivo* EPID and DEEPID cranio-caudal dose profiles of a large rectum IMRT field are shown. Without the DEEPID correction, similar to the results of Fig. 3, there was an

underestimation of the EPID-reconstructed dose for the parts that were within the field. A good agreement with the TPS was only observed in the central unattenuated region. With DEEPID, the agreement with the TPS is also good in the outer attenuated region. TPS, EPID and DEEPID 2D dose distributions and γ -distributions for five rectum IMRT fields are displayed in **Fig. 6.6**.

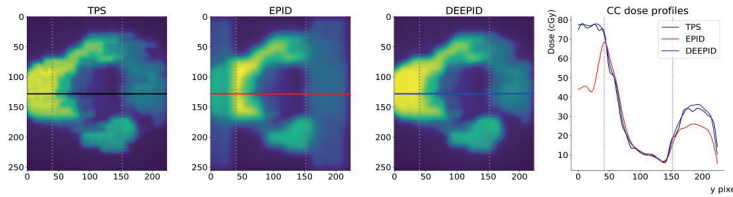


Fig. 6.5. TPS, EPID and DEEPID 2D dose distributions at the isocenter corresponding to the *in vivo* verification of a large rectum IMRT field. Cranial-caudal dose profiles are displayed in black, red and blue, respectively. The dotted grey lines represent the boundaries between central and outer regions.

	DEEPID		EPID	
	γ -pass rate %	γ -mean	γ -pass rate %	γ -mean
Central region	91.6 \pm 6.6	0.47 \pm 0.11	88.8 \pm 7.5	0.56 \pm 0.12
Outer region	90.2 \pm 8.9	0.52 \pm 0.14	44.5 \pm 22.4	2.22 \pm 2.70
Entire field	91.0 \pm 6.7	0.49 \pm 0.11	79.2 \pm 13.3	0.84 \pm 0.35

Table 6.1. Results of the comparison between DEEPID and EPID with TPS 2D dose distributions corresponding to the *in vivo* verification of 45 rectum IMRT fields. Results are presented as AVG \pm (1SD).

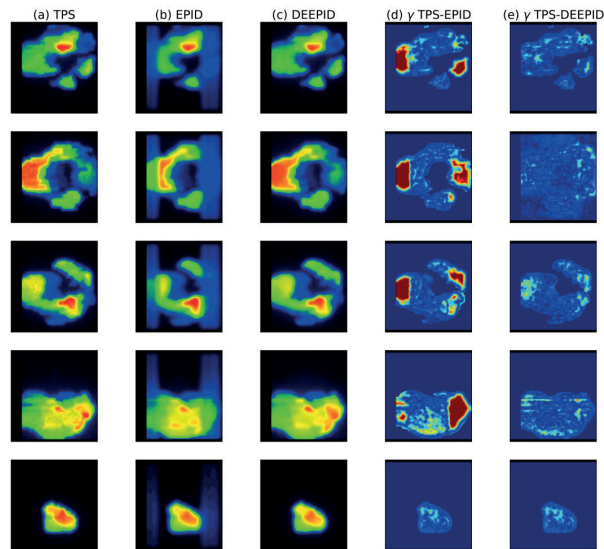


Fig. 6.6. TPS, EPID and DEEPID 2D dose distributions and γ -maps for five representative rectum IMRT fields. Only the last one is not a large field.

6.3.4. Introduction of errors

Results after ± 1.5 mm movements of the leaf bank are displayed in **Fig. 6.7** for both EPID and DEEPID dose reconstructions. As in the example of Fig. 5, the DEEPID correction accurately reconstructs the dose in the outer region. The sensitivity to the error is also higher with DEEPID, as can be deduced from the presented γ -maps. Regarding the effect of -5% and +5% MU errors on DEEPID dose images, the isocenter dose difference for all fields combined with respect to the no-error situation was found to be -4.4% and +5.3%, respectively. The sensitivity of DEEPID to this error is further illustrated in **Fig. 6.8**, where dose profiles corresponding to one rectum field are displayed. Note that, in this case, the DEEPID correction improved also the agreement with the TPS in the central region for the no-error case, see Figs. **6.8.c** and **6.8.d**.

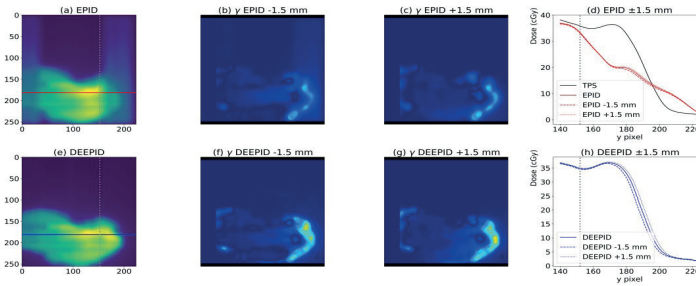


Fig. 6.7. Effect of ± 1.5 mm leaf bank errors on EPID and DEEPID dose distributions. (a) EPID dose distributions for the no-error delivery of a large rectum field, (b,c) γ -distributions (2% / 1 mm) between no-error and error EPID dose distributions and (d) dose profiles. The same is displayed in (e,f,g,h) for DEEPID. The TPS dose profile for the no-error delivery is displayed for comparison.

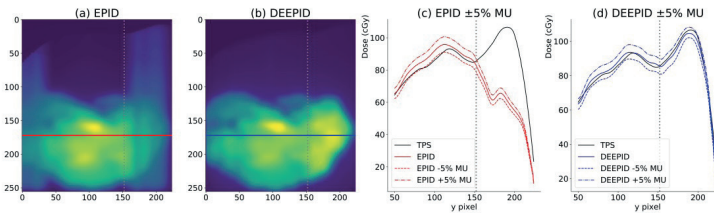


Fig. 6.8. Effect of $\pm 5\%$ MU errors on EPID and DEEPID dose distributions. (a,b) EPID and DEEPID 2D dose distributions for the no-error delivery and (c,d) EPID and DEEPID dose profiles. The TPS dose profile for the no-error delivery is displayed for comparison.

6.4. Discussion

In this study, we have used deep learning to correct the limitations of the EPID dose back-projection algorithm in the outer attenuated region of EPID images of the Unity MR-linac, making *in vivo* dosimetric validation feasible using the entire EPID image. The deficiencies of EPID dosimetry for the Unity MR-Linac were presented with square field measurements in **Fig. 6.3**. They illustrate how the EPID dose modelling of the panel fails to account for the differences in scatter

and attenuation in a range of field sizes for beams that traverse the non-coil free regions. During the last step of the pixel to portal dose response fit in the commissioning process¹⁷⁷, the parameters of a kernel are fitted to minimize the difference between the reconstructed dose at the EPID level and array measurements profiles in both LR and CC directions for a set of square fields irradiated at gantry angle 0°. The kernel is a rotationally symmetric gaussian kernel with no directional bias, producing incorrect results in the outer attenuated region. The use of asymmetric kernels and/or dedicated correction masks in the dose modelling of the panel was unsuccessfully explored prior to the investigation of the Deep Learning-based solution presented in this study.

The results of the 5-fold cross validation demonstrate how DEEPID improves the accuracy of dose reconstructions in the outer attenuated region. This was also corroborated with the *in vivo* verification results presented in **Table 6.1** and with the example of **Fig. 6.5**. The results presented in section 6.3.4. prove that DEEPID is sensitive to errors introduced in the outer attenuated region as it was the case with the ± 1.5 mm leaf bank errors introduced for a large rectum IMRT field. The dosimetric effects of $\pm 5\%$ MUs errors were also correctly considered by DEEPID. This demonstrates the capability of the method to detect clinically relevant errors.

The EPID dose images utilized for training were reconstructed using non-transit EPID dosimetry from raw portal data acquired without a phantom/patient in the beam. However, the intended use of the model is for *in vivo* verification using transit EPID dosimetry from raw portal data acquired behind the patient. Although the dose engines for non-transit and transit EPID dosimetry are similar, they are not identical. Therefore, a more accurate model is expected if the EPID dose images utilized for training were reconstructed using transit EPID dosimetry from raw portal data acquired behind a phantom.

Secondly, TPS dose calculations on the Octavius^{MR} phantom were used as the ideal output of the U-Net during training. These calculations are believed to be accurate enough for the purpose of the study. Absolute dose measurements made with an MR-compatible Octavius 1500 2D detector array (PTW, Freiburg, Germany) were alternatively considered as ground truth for training. However, this option was disregarded due to the low resolution of the detector array (1405 vented ionization chambers with 7.1 mm center-to-center distance). Finally, the attenuation of the cryostat, couch and bridge (at the exit of the phantom) varies considerably with gantry angle ¹⁷⁷. Results should improve if a dedicated U-Net model was trained for each gantry angle separately. Finally, beams exceeding 8.1 cm in the caudal direction at isocenter plane, or 11 cm in the cranial direction, or ± 11 cm in the lateral direction, will have parts that fall outside the panel. Evidently, no reconstruction method will be able to detect errors when these occur in these undetected parts of the beam.

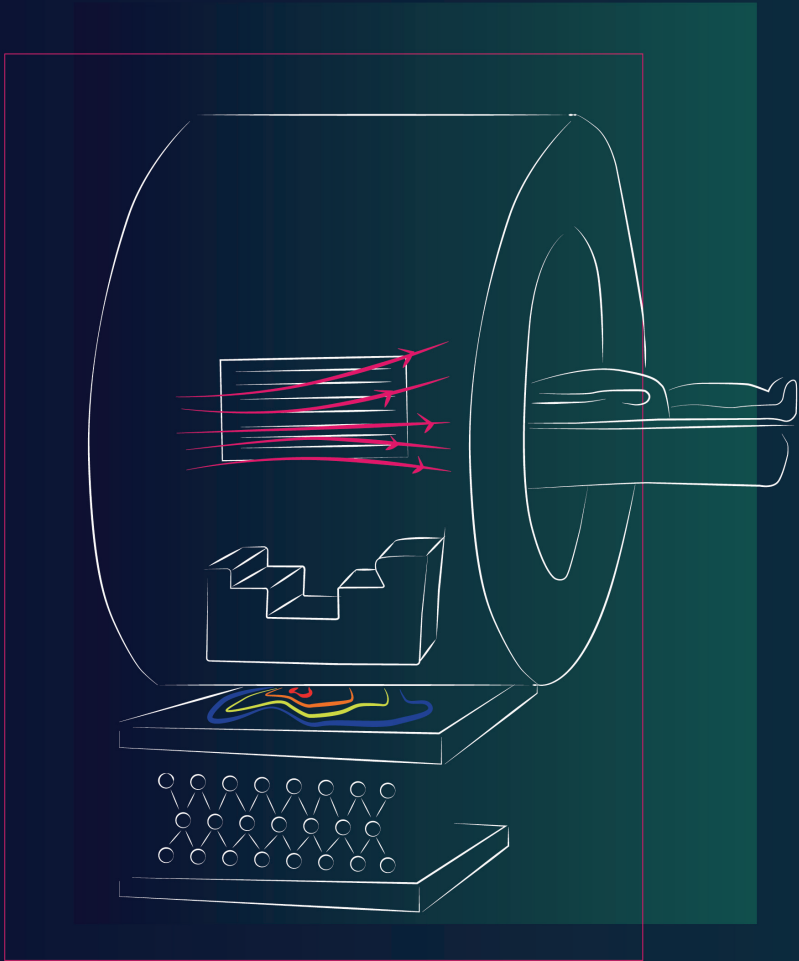
The study demonstrates that Deep Learning can become a very powerful technique to correct deficiencies of portal dosimetry algorithms. A first estimate of the delivered dose distribution is generated using EPID dosimetry and then we pass the results to a convolutional neural network for a final correction.

6.5. Conclusions

A Deep Learning-based method corrects the deficiencies of EPID dosimetry to account for the extra attenuation and scatter in the outer attenuated region. The method allows for accurate dose back-projection at the isocenter plane using the entire EPID image. With this method, dosimetric verification becomes possible for field sizes up to $\sim 19 \times 22$ cm² at isocenter. The method can be used to detect clinically relevant errors.

6.6. Acknowledgements

The authors wish to thank B. Vivas-Maiques, A. Torres Valderrama and S. v.d. Velden for their fruitful discussions.



7.

GENERAL DISCUSSION

7.1. General discussion and thesis achievements

In-vivo EPID dosimetry is a quality control method to improve patient safety in radiotherapy^{51,193}. In this thesis we aimed to develop and validate a method for pre-treatment and *in-vivo* 3D dosimetric verification of Unity MR-linac treatments using EPID dosimetry. This aim was met by adapting the physics models and software used for EPID dosimetry on conventional linacs. We provided clinical evidence that 3D portal dosimetry is feasible and can be a valuable tool for QA in the workflow of the Unity MR-linac. To this end, in Chapter 3 we characterized the dosimetric properties of the a-Si EPID panel in the Unity MR-linac and its behavior in close proximity to the MRI scanner. We further adapted an existing back-projection algorithm used with conventional linacs to the geometry of the Unity MR-linac. Based on the results presented in Chapter 2 and Chapter 4, the EPID dosimetry software was adapted to provide a comparison between EPID reconstructed dose distributions and the TPS. The first 3D *in-vivo* verification results were reported in Chapter 5.

The position of the panel with respect to the patient and the beam represented the main challenges when using the EPID for back-projection portal dosimetry. To avoid the presence of the Lorentz force in the accelerator gun, it is mounted on a rotating ring gantry in a low magnetic field area. The EPID is located in the same low B-field donut, opposite to the linac head. Furthermore, due to the MRI design, only the central part of the beam arrives to the panel with homogeneous attenuation. Outside this window, the beam is considerably more attenuated before reaching the panel. As a result, using the method described in Chapter 5, EPID dose distributions are accurately reconstructed only for radiation detected through the window free of gradient coils and shimming hardware. In Chapter 6 we developed a method that uses deep learning to correct the extra attenuation outside

the aforementioned window, making in vivo dosimetric validation feasible for the entire EPID image.

While automation is not the focus of the presented work, the development of an automated QA EPID-based solution is being implemented clinically now, which is essential to create a smooth system capable to generate verification reports. With such a system available, physicists can focus on the clinical relevance of dosimetric deviations instead of performing tedious manual labor for plan QA.

7.2. The use of EPID Dosimetry in MR-guided Radiotherapy

Currently, the first centers are gaining experience in the use of MR-guided radiotherapy with the Unity system and the methods for QC and QA that need to be applied. The needs for in-vivo dosimetry in MR-guided radiotherapy clearly differ from the needs in conventional External Beam Radiation Therapy (EBRT) QA.

In conventional EBRT, dosimetric verification is first of all performed to verify the accuracy of TPS dose calculation, but, depending on the workflow, also for data transfer verification. Given the fact that a plan is created off-line, prior to the treatment, pre-treatment verification is applied. However, with in-vivo EPID dosimetry, a complete end-to-end dosimetric verification of the treatment chain became feasible. It was shown that errors related to data transfer, dose delivery, patient set-up, MLC calibration and dose calculation could be detected ¹⁰⁵. Furthermore, clinical workload of in vivo EPID dose verification was limited with respect to pre-treatment verification.

With the rise of newly developed systems for MR-guided radiotherapy ^{93,106,108,109}, workflow concepts have evolved and QA needs have changed. For instance, in the Unity system, for every fraction a different plan

is created online while the patient is on the couch^{96,194,195}. In some institutions, an independent TPS is employed to perform online verification of the dose calculation. Even when such a TPS does not consider the magnetic field, it should detect gross deviations. At NKI we use an in-house developed program that conducts a simple check of plan characteristics, such as number and area of segments, number of MU's etc.

It is obvious that conventional pre-treatment dosimetry methods are of limited use for such a workflow. Therefore, it is necessary to establish a routine tool for the dosimetric verification of the TPS dose calculation that also serves as an end-to-end check of the entire chain. In MRgRT, the end-to-end check is actually more important due to the unprecedented complexity of the workflow. The sensitivity of EPID in-vivo for dosimetric verification is still to be further investigated, but what we can claim is that, as it is a measurement-based method, it is a perfect candidate for such an end-to-end check.

Most of the existing measurement devices, such as 2D arrays, film or IC's in rotating phantoms can only perform pre-treatment verification of the reference plan, which serves to validate issues such as MLC calibration, dose calculation, linac delivery errors and data transfer. However daily adapted plans can't be dosimetrically verified prior to irradiation with these techniques as the new plan is only generated once the patient is in position.

At this moment, the use of a pseudo CT is not yet clinical for the Unity system. Instead, an attenuation map is used for dose calculations that can either be a pre-treatment planning CT that doesn't represent the anatomy of the time of treatment, or an MRI with density overrides. In the future this may be replaced by a pseudo CT, with a representative attenuation map derived from MRI.

Dosimetric verification of Unity treatments can also be achieved by using the linac log files in combination with an (independent) dose engine and an accurate patient model. Potentially, when the actual anatomy of the patient is used, patient related errors (patient set-up, intra-fraction motion, tumor shrinkage, etc.) can be detected without additional measurement time. A drawback of this method is that it is not based on an independent transmission measurement and its reliability depends on the assumption of a correct determination of both the output of the linear accelerator and the anatomy (pre-treatment planning CT, MRI with density overrides or pseudo CT), which can only be verified with measurements. In this sense, EPID in vivo dosimetry is a more comprehensive check as it verifies the entire adapted chain.

For the MR-linac, recent studies ^{166,196} show that pre-treatment QA performed using 2D IC arrays in phantoms in different institutes have detected minimum differences when comparing measured and planned dose distributions. This suggests that the reproducibility and accuracy of the Unity systems is high and that errors in dose calculation and delivery are rare. While this may reduce the need for on-line verification of the dose calculation, errors related to data transfer, patient setup, and pseudo-CT determination are still feasible. A measurement-based system that efficiently and independently checks the entire workflow from end-to-end with almost no added time will help understand the weak points of the new workflow and its most relevant error sources and types.

7.3. Challenges and future work

7.3.1. Implementation challenges

The presented results show very good agreement between EPID and TPS dose distributions, but several issues still need to be addressed to create a tool for the clinic that can be used for all fractions automatically, reducing workload and adding value to existing methods. This is both the research and implementation work that needs to be done to have a full-working in-vivo EPID dosimetry solution for the Unity MR-linac.

Verification of every treatment by means of in-vivo EPID dosimetry to date requires manual work, which should be automated to make it a practical tool for all deliveries. This requires acquired data to be automatically transferred and linked to the correct daily CT and plan data. It further requires software to operate in batch mode and store results in a proper inspection software for quick analysis.

If the software is implemented to run in real-time during delivery^{89,133} gross error detection could potentially be used to halt the machine. This would result in a solution that would not only catch but also prevent major dose deviations. This requires automation, but also a reduction of computational time of the dose calculations to allow synchronization with the delivery. It further needs integration with the Unity software. Additionally, thresholds for errors that should stop the linac would need to be established based on a retrospective analysis of the deviations detected. This would probably be necessary for each treatment site.

One of the main drawbacks of the design of the machine for the presented algorithm is the position of the EPID with respect to the beam and the patient. Some parts of the beams arriving to the panel are either not uniformly attenuated because they traverse a thicker in-

homogeneous region of the MRI scanner, or are directly not captured by the panel because they fall outside the detection area.

EPID-based dosimetric verification for fields falling outside the central region is not accurate, as is the case, for instance, in current clinical IMRT rectum plans. However, in Chapter 6 we explore an approach that uses Deep Learning to correct the limitations of the EPID dose back-projection algorithm in the outer attenuated region of the 2D EPID frames making *in vivo* dosimetric validation feasible for the entire EPID frame. However, the clinical development of such solution represents a major challenge in terms of platform implementation. Moreover, the extension of 2D to 3D deep learning-based correction is also not straightforward and would require further research. Another option would be to improve the physical model at the EPID level to account and correct for the in-homogeneous attenuation of the primary beam and the MRI to EPID scatter arriving to the panel.

Beams, falling outside the panel (parts exceeding 8.1 cm in the caudal direction at isocenter plane) cannot be reconstructed with any possible method, as that information is not captured at all. The only alternative would be the engineering of new larger panels integrated in the machine, or the combination of two panels covering the entire field area.

7.3.2. Clinical considerations of in-vivo EPID dosimetry for the MR-Linac

Once the issues described in the previous section are resolved, the focus needs to shift to the decision making that is done based on observed EPID dose deviations

In our clinical practice for conventional linacs only 3 fractions are inspected per treatment. However, in the daily adapted workflow, all fractions could potentially be verified by means of in-vivo EPID

dosimetry, at no additional cost in terms of measurement time. Nevertheless, this would require more work from the medical physicists to inspect QA reports of all fractions or it would need further automation. It is an open issue to set a good balance between the number of fractions to verify and the amount of inspection work that it would arise.

Although in Chapter 6 we introduce errors ($\pm 5\%$ MU, ± 1.5 mm shifts) in the delivery of rectum plans to assess the degree of confidence of our deep-learning based correction, the exact magnitude of the errors that can be detected with EPID in-vivo dosimetry is still not determined. Its main use in the Unity system is aimed to catch gross errors, but finding out its limitations will ultimately determine the use of this tool in the clinic. In order to have an estimate of such, a specificity and sensitivity study should be performed. It would help to set optimal thresholds for the chosen evaluation criteria (γ , DVH), leading to a good balance between false positives and false negatives, and reasonable inspection workload in the clinic. For the completeness of this study, it would be interesting to carry out a study about the magnitude of errors per site, to establish site-specific thresholds, allowing more or less restrictive criteria for sites that usually show larger deviations than others. For instance, lung and head-and-neck are traditionally more difficult to verify given their inhomogeneities.

As for now, all results shown in this thesis compare TPS doses that include the presence of the magnetic field to back-projected dose distributions that do not account for it. It has been shown that for large inhomogeneities in the irradiated volume, the dose re-distributions due to the electron return effect caused by the magnetic field are significant^{91,100,136,197}. However, as γ -results of the examples of this work are comparable to values of previous studies performed with conventional linacs¹⁹⁸, it suggests that the impact of the ERE is limited in the

high dose volume in quite homogeneous regions. However, for other treatment sites (lung, head-and-neck) this might give more problems. It can be argued, that in-vivo EPID dosimetry in its current form is more suitable to detect large deviations rather than small discrepancies. A dedicated study would be required to assess its importance (by introduction of errors related to the absence of the magnetic, as stated in previous paragraph), which ultimately will determine the scope of its use: gross error detection or accurately reconstruction of the delivered dose. In any case, as discussed throughout this thesis, two alternatives are on the table to cope with this issue: first, a comparison of the EPID back-projected doses to a version of the TPS that switches off the magnetic field; second, to back-project the EPID dose to a plane above the patient, to be used to feed an independent forward dose-engine¹⁷⁰ that accounts for the magnetic field, and then compare it to the TPS.

We might be able to shed light on some of the discussed open issues and limitations by means of introducing different magnitudes of errors to EPID in-vivo dose reconstructions. By doing so, we will be able to establish the extent of our solution and determine proper alert criteria. Within the scope of these studies, it is of particular interest to observe the response of our solution to the introduction of the following errors:

- errors in the patient anatomy (MRI with wrong density overrides -for now-) and in the set-up, to have a clear idea of the magnitude of errors that we are capable to detect related to this new step of the adapted workflow.
- a study on the response of our method to introduced errors in the outer region of the panel -where reconstruction is poor- would also shed light on the accuracy and sensitivity of the deep learning method proposed in Chapter 6.
- Errors related to the absence of the magnetic field in the EPID reconstructed dose distributions. If studies show large deviations due to ERE effects, this issue needs to be addressed with high priority.

7.4. Conclusion

We have developed the first system to verify MR-guided RT treatments using transit EPID images acquired during irradiation.

The work presented in this thesis represents a step forward in MR-guided radiotherapy patient safety to verify both pre-treatment and in-vivo fractions and provide a strong reduction in clinical workload.

8.

REFERENCES

1. Sandoiu A. MedicalNewsToday. <https://www.medicalnewstoday.com/articles/323677.php>.
2. Baskar R, Dai J, Wenlong N, Yeo R, Yeoh K-W. Biological response of cancer cells to radiation treatment. *Front Mol Biosci.* 2014;1(November):1-9. doi:10.3389/fmolb.2014.00024
3. Colgan R, McClelland J, McQuaid D, et al. Planning lung radiotherapy using 4D {CT} data and a motion model. *Phys Med Biol.* 2008;53(20):5815-5830. doi:10.1088/0031-9155/53/20/017
4. Differding S, Hanin F-X, Grégoire V. PET imaging biomarkers in head and neck cancer. *Eur J Nucl Med Mol Imaging.* 2015;42(4):613-622. doi:10.1007/s00259-014-2972-7
5. Sergieva S, Mihailova I, Zahariev Z, Dimcheva M, Bozhikov S. Role of SPECT-CT in radiotherapy. *J BUON.* 2014;19(3):831-835.
6. van der Meer S, Bloemen-van Gurp E, Hermans J, et al. Critical assessment of intramodality 3D ultrasound imaging for prostate IGRT compared to fiducial markers. *Med Phys.* 2013;40(7):71707. doi:10.1118/1.4808359
7. Groenendaal G, Moman MR, Korporaal JG, et al. Validation of functional imaging with pathology for tumor delineation in the prostate. *Radiother Oncol.* 2010;94(2):145-150. doi:10.1016/j.radonc.2009.12.034
8. Bentzen SM. Theragnostic imaging for radiation oncology: Dose-painting by numbers. *Lancet Oncol.* 2005;6(2):112-117. doi:10.1016/S1470-2045(05)01737-7
9. van der Heide UA, Houweling AC, Groenendaal G, Beets-Tan RGH, Lambin P. Functional MRI for radiotherapy dose painting. *Magn Reson Imaging.* 2012;30(9):1216-1223. doi:<https://doi.org/10.1016/j.mri.2012.04.010>
10. Even AJG, Van Der Stoep J, Zegers CML, et al. PET-based dose painting in non-small cell lung cancer: Comparing uniform dose escalation with boosting hypoxic and metabolically active sub-volumes. *Radiother Oncol.* 2015;116(2):281-286. doi:10.1016/j.radonc.2015.07.013

11. Harat M, Małkowski B, Makarewicz R. Pre-irradiation tumour volumes defined by MRI and dual time-point FET-PET for the prediction of glioblastoma multiforme recurrence: A prospective study. *Radiother Oncol.* 2016;120(2):241-247. doi:10.1016/j.radonc.2016.06.004
12. Uzan J, Nahum AE, Syndikus I. Prostate Dose-painting Radiotherapy and Radiobiological Guided Optimisation Enhances the Therapeutic Ratio. *Clin Oncol.* 2016;28(3):165-170. doi:10.1016/j.clon.2015.09.006
13. Zamboglou C, Sachpazidis I, Koubar K, et al. Evaluation of intensity modulated radiation therapy dose painting for localized prostate cancer using 68Ga-HBED-CC PSMA-PET/CT: A planning study based on histopathology reference. *Radiother Oncol.* 2017;123(3):472-477. doi:10.1016/j.radonc.2017.04.021
14. BOGDANICH W. As Technology Surges, Radiation Safeguards Lag. *New York Times.*
15. BOGDANICH W. Radiation Offers New Cures, and Ways to Do Harm. *New York Times.*
16. Times T. Case Studies : When Medical Radiation Goes Awry. *New York Times.* <https://www.nytimes.com/2010/01/27/us/27RADIATIONSIDEBAR.html>. Published 2010.
17. Williams M V. Improving patient safety in radiotherapy by learning from near misses, incidents and errors. *Br J Radiol.* 2007;80(953):297-301. doi:10.1259/bjr/29018029
18. Derreumaux S. Lessons From Recent Accidents in. 2008;131(January):130-135.
19. Asnaashar K, Gholami S, Khosravi HR. Lessons learnt from errors in radiotherapy centers. *Iran J Radiat Res.* 2014;12(4):361-367. <http://www.scopus.com/inward/record.url?eid=2-s2.0-84920135613&partnerID=tZOtx3y1>
20. Das P, Johnson J, Hayden SE, et al. Rate of Radiation Therapy Events in a Large Academic Institution. *J Am Coll Radiol.* 2013;10(6):452-455. doi:https://doi.org/10.1016/j.jacr.2012.12.010

21. Spraker MB, Fain R, Gopan O, et al. Evaluation of near-miss and adverse events in radiation oncology using a comprehensive causal factor taxonomy. *Pract Radiat Oncol.* 2017;7(5):346-353. doi:10.1016/j.prro.2017.05.008
22. Ford EC, Evans SB. Incident learning in radiation oncology: A review. *Med Phys.* 2018;45(5):e100-e119. doi:10.1002/mp.12800
23. McKenzie EM, Balter PA, Stingo FC, Jones J, Followill DS, Kry SF. Toward optimizing patient-specific IMRT QA techniques in the accurate detection of dosimetrically acceptable and unacceptable patient plans. *Med Phys.* 2014;41(12):1-15. doi:10.1118/1.4899177
24. van Elmpt W, Nijsten S, Mijnheer B, Dekker A, Lambin P. The next step in patient-specific QA: 3D dose verification of conformal and intensity-modulated RT based on EPID dosimetry and Monte Carlo dose calculations. *Radiother Oncol.* 2008;86(1):86-92. doi:10.1016/j.radonc.2007.11.007
25. Agazaryan N. Patient specific quality assurance for the delivery of intensity modulated radiotherapy. *J Appl Clin Med Phys.* 2003;4(1):40. doi:10.1120/1.1525243
26. Ramachandran P, Tajaldeen A, Taylor D, Wanigaratne D, Roozen K, Geso M. Evaluation and Performance of ArcCheck and Film using Gamma Criteria in Pre-treatment Quality Assurance of Stereotactic Ablative Radiotherapy. *J Med Phys.* 2017;42(4):251-257. doi:10.4103/jmp.JMP_132_16
27. Blackwell CR, Coursey BM, Gall KP, et al. Radiochromic Film Dosimetry: Recommendations of AAPM Radiation Therapy Task Group 55. *Med Phys.* 1998;25(63):2093-2115.
28. Borca VC, Pasquino M, Russo G, et al. Dosimetric characterization and use of GAFCHROMIC EBT3 film for IMRT dose verification. *J Appl Clin Med Phys.* 2013;14(2):158-171. doi:10.1120/jacmp.v14i2.4111
29. Ulya S, Wibowo WE, Nuruddin N, Pawiro SA. Dosimetric Characteristics of EBT3 Gafchromic Film on Small Field

- Electron. AIP J. 2016;(2016):8-13.
30. Devic S. Radiochromic film dosimetry: Past, present, and future. *Phys Medica*. 2011;27(3):122-134. doi:10.1016/j.ejmp.2010.10.001
 31. Fuss M, Sturtewagen E, Wagter C De, Georg D. Dosimetric characterization of {GafChromic} {EBT} film and its implication on film dosimetry quality assurance. *Phys Med Biol*. 2007;52(14):4211-4225. doi:10.1088/0031-9155/52/14/013
 32. Banci Buonamici F, Compagnucci A, Marrazzo L, Russo S, Bucciolini M. An intercomparison between film dosimetry and diode matrix for IMRT quality assurance. *Med Phys*. 2007;34(4):1372-1379. doi:10.1118/1.2713426
 33. Lee PC, Sawicka JM, Glasgow GP. Patient dosimetry quality assurance program with a commercial diode system. *Int J Radiat Oncol*. 1994;29(5):1175-1182. doi:https://doi.org/10.1016/0360-3016(94)90415-4
 34. Esch A Van, Clermont C, Devillers M, Iori M, Huyskens DP. On-line quality assurance of rotational radiotherapy treatment delivery by means of a 2D ion chamber array and the Octavius phantom. *Med Phys*. 2007;34(10):3825-3837. doi:10.1118/1.2777006
 35. O'Daniel J, Das S, Wu QJ, Yin FF. Volumetric-modulated arc therapy: Effective and efficient end-to-end patient-specific quality assurance. *Int J Radiat Oncol Biol Phys*. 2012;82(5):1567-1574. doi:10.1016/j.ijrobp.2011.01.018
 36. Poppe B, Blechschmidt A, Djouguela A, et al. Two-dimensional ionization chamber arrays for IMRT plan verification. *Med Phys*. 2006;33(4):1005-1015. doi:10.1118/1.2179167
 37. Spezi E, Angelini AL, Romani F, Ferri A. Characterization of a 2D ion chamber array for the verification of radiotherapy treatments. *Phys Med Biol*. 2005;50(14):3361-3373. doi:10.1088/0031-9155/50/14/012
 38. Bouchard H, Seuntjens J. Ionization chamber-based reference dosimetry of intensity modulated radiation beams. *Med Phys*. 2004;31(9):2454-2465. doi:10.1118/1.1781333

39. Almond PR, Svensson H. Ionization chamber dosimetry for photon and electron beams. *Acta Oncol (Madr)*. 1977;16(2):177-186. doi:10.3109/02841867709134310
40. De Deene Y, De Wagter C, Van Duyse B, Derycke S, De Neve W, Achten E. Three-dimensional dosimetry using polymer gel and magnetic resonance imaging applied to the verification of conformal radiation therapy in head- and-neck cancer. *Radiother Oncol*. 1998;48(3):283-291. doi:10.1016/S0167-8140(98)00087-5
41. Gustavsson H, Karlsson A, Bäck SÅJ, et al. MAGIC-type polymer gel for three-dimensional dosimetry: Intensity-modulated radiation therapy verification. *Med Phys*. 2003;30(6):1264-1271. doi:10.1118/1.1576392
42. Vergote K, Deene Y De, Duthoy W, et al. Validation and application of polymer gel dosimetry for the dose verification of an intensity-modulated arc therapy (IMAT) treatment. *Phys Med Biol*. 2004;49(2):287-305. doi:10.1088/0031-9155/49/2/008
43. Low DA, Dempsey JF, Venkatesan R, et al. Evaluation of polymer gels and MRI as a 3-D dosimeter for intensity-modulated radiation therapy. *Med Phys*. 1999;26(8):1542-1551. doi:10.1118/1.598650
44. van Herk M, Meertens H. A matrix ionisation chamber imaging device for on-line patient setup verification during radiotherapy. *Radiother Oncol*. 1988;11(4):369-378. doi:https://doi.org/10.1016/0167-8140(88)90208-3
45. Meertens H, van Herk M, Bijhold J, Bartelink H. First clinical experience with a newly developed electronic portal imaging device. *Int J Radiat Oncol*. 1990;18(5):1173-1181. doi:https://doi.org/10.1016/0360-3016(90)90455-S
46. Essers M, Hoogervorst BR, van Herk M, Lanson H, Mijnheer BJ. Dosimetric characteristics of a liquid-filled electronic portal imaging device. *Int J Radiat Oncol Biol Phys*. 1995;33(5):1265-1272. doi:10.1016/0360-3016(95)00108-5
47. Korevaar EW, Wauben DJL, van der Hulst PC, Langendijk JA,

- van't Veld AA. Clinical introduction of a linac head-mounted 2D detector array based quality assurance system in head and neck IMRT. *Radiother Oncol.* 2011;100(3):446-452. doi:<https://doi.org/10.1016/j.radonc.2011.09.007>
48. Alrowaili ZA, Lerch MLF, Carolan M, et al. 2D mapping of the {MV} photon fluence and 3D dose reconstruction in real time for quality assurance during radiotherapy treatment. *J Instrum.* 2015;10(09):P09019--P09019. doi:10.1088/1748-0221/10/09/p09019
 49. Litzenberg DW, Moran JM, Fraass BA. Verification of dynamic and segmental IMRT delivery by dynamic log file analysis. *J Appl Clin Med Phys.* 2002;3(2):63-72. doi:10.1120/jacmp.v3i2.2578
 50. Qian J, Lee L, Liu W, et al. Dose reconstruction for volumetric modulated arc therapy (VMAT) using cone-beam CT and dynamic log files. *Phys Med Biol.* 2010;55(13):3597-3610. doi:10.1088/0031-9155/55/13/002
 51. Mans A, Wendling M, McDermott LN, et al. Catching errors with in vivo EPID dosimetry. *Med Phys.* 2010;37(6):2638-2644. doi:10.1118/1.3397807
 52. Ford EC, Terezakis S, Souranis A, Harris K, Gay H, Mutic S. Quality control quantification (QCQ): A tool to measure the value of quality control checks in radiation oncology. *Int J Radiat Oncol Biol Phys.* 2012;84(3):e263-e269. doi:10.1016/j.ijrobp.2012.04.036
 53. Piermattei A, Fidanzio A, Stimato G, et al. In vivo dosimetry by an aSi-based EPID. *Med Phys.* 2006;33(11):4414-4422. doi:10.1118/1.2360014
 54. Piermattei A, Fidanzio A, Azario L, et al. In patient dose reconstruction using a cine acquisition for dynamic arc radiation therapy. *Med Biol Eng Comput.* 2009;47(4):425-433. doi:10.1007/s11517-009-0456-x
 55. Chytyk K, Mccurdy BMC. Comprehensive fluence model for absolute portal dose image prediction. *Med Phys.* 2009;36(4):1389-1398. doi:10.1118/1.3083583

56. Chytyk-Praznik K, Vanuytven E, Vanbeek TA, Greer PB, McCurdy BMC. Model-based prediction of portal dose images during patient treatment. *Med Phys.* 2013;40(3). doi:10.1118/1.4792203
57. Bedford JL, Hanson IM, Hansen VN. Portal dosimetry for VMAT using integrated images obtained during treatment. *Med Phys.* 2014;41(2). doi:10.1118/1.4862515
58. Wendling M, McDermott LN, Mans A, Sonke J-J, van Herk M, Mijnheer BJ. A simple backprojection algorithm for 3D in vivo EPID dosimetry of IMRT treatments. *Med Phys.* 2009;36(7):3310-3321. doi:10.1118/1.3148482
59. Mans A, Remeijer P, Olaciregui-Ruiz I, et al. 3D Dosimetric verification of volumetric-modulated arc therapy by portal dosimetry. *Radiother Oncol.* 2010;94(2):181-187. doi:10.1016/j.radonc.2009.12.020
60. van Elmpt W, Nijsten S, Petit S, Mijnheer B, Lambin P, Dekker A. 3D In Vivo Dosimetry Using Megavoltage Cone-Beam CT and EPID Dosimetry. *Int J Radiat Oncol Biol Phys.* 2009;73(5):1580-1587. doi:10.1016/j.ijrobp.2008.11.051
61. van Elmpt W, Petit S, De Ruyscher D, Lambin P, Dekker A. 3D dose delivery verification using repeated cone-beam imaging and EPID dosimetry for stereotactic body radiotherapy of non-small cell lung cancer. *Radiother Oncol.* 2010;94(2):188-194. doi:10.1016/j.radonc.2009.12.024
62. Scalchi P, Francescon P. Calibration of a MOSFET detection system for 6-MV in vivo dosimetry. *Int J Radiat Oncol Biol Phys.* 1998;40(4):987-993. doi:10.1016/S0360-3016(97)00894-8
63. Halvorsen PH. Dosimetric evaluation of a new design MOSFET in vivo dosimeter. *Med Phys.* 2005;32(1):110-117. doi:10.1118/1.1827771
64. Higgins PD, Alaei P, Gerbi BJ, Dusenbery KE. In vivo diode dosimetry for routine quality assurance in IMRT. *Med Phys.* 2003;30(12):3118-3123. doi:10.1118/1.1626989
65. Kirby MC, Williams PC. The use of an electronic portal imaging

- device for exit dosimetry and quality control measurements. *Int J Radiat Oncol.* 1995;31(3):593-603. doi:[https://doi.org/10.1016/0360-3016\(94\)00388-2](https://doi.org/10.1016/0360-3016(94)00388-2)
66. Essers M, Lanson JH, Leunens G, Schnabel T, Mijnheer BJ. The accuracy of CT-based inhomogeneity corrections and in vivo dosimetry for the treatment of lung cancer. *Radiother Oncol.* 1995;37(3):199-208. doi:[https://doi.org/10.1016/0167-8140\(95\)01659-7](https://doi.org/10.1016/0167-8140(95)01659-7)
 67. Boellaard R, Van Herk M, Uiterwaal H, Mijnheer B. Two-dimensional exit dosimetry using a liquid-filled electronic portal imaging device and a convolution model. *Radiother Oncol.* 1997;44(2):149-157. doi:[10.1016/S0167-8140\(97\)00073-X](https://doi.org/10.1016/S0167-8140(97)00073-X)
 68. Kroonwijk M, Pasma KL, Quint S, Koper PCM, Visser AG, Heijmen BJM. In vivo dosimetry for prostate cancer patients using an electronic portal imaging device (EPID); demonstration of internal organ motion. *Radiother Oncol.* 1998;49(2):125-132. doi:[10.1016/S0167-8140\(98\)00122-4](https://doi.org/10.1016/S0167-8140(98)00122-4)
 69. Van Uytven E, Van Beek T, McCowan PM, Chytyk-Praznik K, Greer PB, McCurdy BMC. Validation of a method for in vivo 3D dose reconstruction for IMRT and VMAT treatments using on-treatment EPID images and a model-based forward-calculation algorithm. *Med Phys.* 2015;42(12):6945-6954. doi:[10.1118/1.4935199](https://doi.org/10.1118/1.4935199)
 70. Wendling M, Louwe RJW, McDermott LN, Sonke J-J, van Herk M, Mijnheer BJ. Accurate two-dimensional IMRT verification using a back-projection EPID dosimetry method. *Med Phys.* 2006;33(2):259-273. doi:[10.1118/1.2147744](https://doi.org/10.1118/1.2147744)
 71. Method NEW, Obtain TO, Midplane THE, Using D, Dosimetry INV. New Method To Obtain the Midplane Dose Using Portal. *Radiat Oncol.* 1998;41(2):465-474.
 72. Dosisoft epigray. <https://www.dosisoft.com/patient-qa/in-vivo-epigray.html>
 73. SunNuclear PerFraction. <http://www.sunnuclear.com/solutions/>

patientqa/perfraction

74. IBA OmniPro-InViDos. <http://www.iba-dosimetry.com/complete-solutions/radiotherapy/in-vivo-dosimetry/omnipro-invidos>
75. Elekta iViewDose. <https://www.elekta.com/radiotherapy/treatment-solutions/quality-assurance/iviewdose>
76. Vazquez-Quino LA, Huerta-Hernandez CI, Rangaraj D. Clinical experience with machine log file software for volumetric-modulated arc therapy techniques. *Baylor Univ Med Cent Proc.* 2017;30(3):276-279. doi:10.1080/08998280.2017.11929614
77. Teke T, Bergman AM, Kwa W, Gill B, Duzenli C, Popescu IA. Monte Carlo based, patient-specific RapidArc QA using Linac log files. *Med Phys.* 2010;37(1):116-123. doi:10.1118/1.3266821
78. Stell AM, Li JG, Zeidan OA, Dempsey JF. An extensive log-file analysis of step-and-shoot intensity modulated radiation therapy segment delivery errors. *Med Phys.* 2004;31(6):1593-1602. doi:10.1118/1.1751011
79. Lee L, Le QT, Xing L. Retrospective IMRT Dose Reconstruction Based on Cone-Beam CT and MLC Log-File. *Int J Radiat Oncol Biol Phys.* 2008;70(2):634-644. doi:10.1016/j.ijrobp.2007.09.054
80. Liu S, Mazur TR, Li H, et al. A method to reconstruct and apply 3D primary fluence for treatment delivery verification. *J Appl Clin Med Phys.* 2017;18(1):128-138. doi:10.1002/acm2.12017
81. Barbeiro AR, Ureba A, Baeza JA, et al. 3D VMAT verification based on monte carlo log file simulation with experimental feedback from film dosimetry. *PLoS One.* 2016;11(11):1-19. doi:10.1371/journal.pone.0166767
82. Low DA, Harms WB, Mutic S, Purdy J a. A technique for the quantitative evaluation of dose distributions. *Med Phys.* 1998;25(5):656-661. doi:10.1118/1.598248
83. Szczurek L, Juszkat R, Szczurek J, Turek I, Sosnowski P. Pre-treatment 2D and 3D dosimetric verification of volumetric arc

- therapy. A correlation study between gamma index passing rate and clinical dose volume histogram. *PLoS One*. 2019;14(8):1-17. doi:10.1371/journal.pone.0221086
84. van der Bijl E, van Oers RFM, Olaciregui-Ruiz I, Mans A. Comparison of gamma- and DVH-based in vivo dosimetric plan evaluation for pelvic VMAT treatments. *Radiother Oncol*. 2017;125(3):405-410. doi:10.1016/j.radonc.2017.09.014
 85. McDermott LN, Wendling M, Nijkamp J, et al. 3D in vivo dose verification of entire hypo-fractionated IMRT treatments using an EPID and cone-beam CT. *Radiother Oncol*. 2008;86(1):35-42. doi:10.1016/j.radonc.2007.11.010
 86. Wendling M, N. McDermott L, Mans A, et al. In aqua vivo EPID dosimetry. *Med Phys*. 2011;39(1):367-377. doi:10.1118/1.3665709
 87. Olaciregui-Ruiz I, Rozendaal R, Mijnheer B, Van Herk M, Mans A. Automatic in vivo portal dosimetry of all treatments. *Phys Med Biol*. 2013;58(22):8253-8264. doi:10.1088/0031-9155/58/22/8253
 88. Olaciregui-Ruiz I, Rozendaal R, van Oers RFM, Mijnheer B, Mans A. Virtual patient 3D dose reconstruction using in air EPID measurements and a back-projection algorithm for IMRT and VMAT treatments. *Phys Medica*. 2017;37:49-57. doi:10.1016/j.ejmp.2017.04.016
 89. Spreeuw H, Rozendaal R, Olaciregui-Ruiz I, et al. Online 3D EPID-based dose verification: Proof of concept. *Med Phys*. 2016;43(7):3969-3974. doi:10.1118/1.4952729
 90. Mijnheer BJ, González P, Olaciregui-Ruiz I, Rozendaal RA, van Herk M, Mans A. Overview of 3-year experience with large-scale electronic portal imaging device-based 3-dimensional transit dosimetry. *Pract Radiat Oncol*. 2015;5(6):e679-e687. doi:10.1016/j.prro.2015.07.001
 91. Raaijmakers a JE, Raaymakers BW, Lagendijk JJW. Integrating a MRI scanner with a 6 MV radiotherapy accelerator: dose increase at tissue-air interfaces in a lateral magnetic field due to returning electrons. *Phys Med Biol*. 2005;50(7):1363-1376.

doi:10.1088/0031-9155/50/7/002

92. Lagendijk JJW, Raaymakers BW, van Vulpen M. The Magnetic Resonance Imaging-Linac System. *Semin Radiat Oncol.* 2014;24(3):207-209. doi:10.1016/j.semradonc.2014.02.009
93. Raaymakers BW, de Boer JCJ, Knox C, et al. Integrated megavoltage portal imaging with a 1.5 T MRI linac. *Phys Med Biol.* 2011;56(19):N207-N214. doi:10.1088/0031-9155/56/19/N01
94. Kupelian P, Sonke J. Magnetic Resonance – Guided Adaptive Radiotherapy: A Solution to the Future. *Semin Radiat Oncol.* 2014;24(3):227-232. doi:10.1016/j.semradonc.2014.02.013
95. Seregni M, Paganelli C, Summers P, Bellomi M, Baroni G, Riboldi M. A hybrid image registration and matching framework for real-time motion tracking in MRI-guided radiotherapy. *IEEE Trans Biomed Eng.* 2018;65(1):131-139. doi:10.1109/TBME.2017.2696361
96. Kashani R, Olsen JR. Magnetic Resonance Imaging for Target Delineation and Daily Treatment Modification. *Semin Radiat Oncol.* 2018;28(3):178-184. doi:10.1016/j.semradonc.2018.02.002
97. Houweling AC, De Vries JHW, Wolthaus J, et al. Performance of a cylindrical diode array for use in a 1.5 T MR-linac. *Phys Med Biol.* 2016;61(3):N80-N89. doi:10.1088/0031-9155/61/3/N80
98. Smit K, Kok JGM, Lagendijk JJW, Raaymakers BW. Performance of a multi-axis ionization chamber array in a 1.5 T magnetic field. *Phys Med Biol.* 2014;59(7):1845-1855. doi:10.1088/0031-9155/59/7/1845
99. De Vries JHW, Seravalli E, Houweling AC, et al. Characterization of a prototype MR-compatible Delta4 QA system in a 1.5 tesla MR-linac. *Phys Med Biol.* 2018;63(2). doi:10.1088/1361-6560/aa9d26
100. Lee HJ, Roed Y, Venkataraman S, Carroll M, Ibbott GS. Investigation of magnetic field effects on the dose–response of 3D dosimeters for magnetic resonance – image guided radiation therapy applications. *Radiother Oncol.* 2017;125(3):426-432.

doi:10.1016/j.radonc.2017.08.027

101. Kaas Jochem et al. A fast automated sanity check for online plan adaptation in MR-guided RT. In: ESTRO37. ; 2018:994.
102. Shafai-Erfani G, Wang T, Lei Y, et al. Dose evaluation of MRI-based synthetic CT generated using a machine learning method for prostate cancer radiotherapy. *Med Dosim.* 2019;(xxxx):12-16. doi:10.1016/j.meddos.2019.01.002
103. Pathmanathan AU, van As NJ, Kerkmeijer LGW, et al. Magnetic Resonance Imaging-Guided Adaptive Radiation Therapy: A “Game Changer” for Prostate Treatment? *Int J Radiat Oncol Biol Phys.* 2018;100(2):361-373. doi:10.1016/j.ijrobp.2017.10.020
104. Kemppainen R, Suilamo S, Tuokkola T, Lindholm P, Deppe MH, Keyriläinen J. Magnetic resonance-only simulation and dose calculation in external beam radiation therapy: a feasibility study for pelvic cancers. *Acta Oncol (Madr).* 2017;56(6):792-798. doi:10.1080/0284186X.2017.1293290
105. Neal B, Ahmed M, Kathuria K, et al. A clinically observed discrepancy between image-based and log-based MLC positions A clinically observed discrepancy between image-based and log-based MLC positions. *Med Phys.* 2016;43:2933. doi:10.1118/1.4949002
106. Mutic S, Dempsey JF. The ViewRay System : Magnetic Resonance -. *Semin Radiat Oncol.* 2014;24(3):196-199. doi:10.1016/j.semradonc.2014.02.008
107. Fallone BG, Murray B, Rathee S, et al. First MR images obtained during megavoltage photon irradiation from a prototype integrated linac-MR system. *Med Phys.* 2009;36(6):2084-2088. doi:10.1118/1.3182419
108. Fallone BG. The Rotating Biplanar Linac-Magnetic Resonance Imaging System. *Semin Radiat Oncol.* 2014;24(3):200-202. doi:10.1016/j.semradonc.2014.02.011
109. Keall PJ, Barton M, Crozier S. The Australian Magnetic Resonance Imaging-Linac Program. *Semin Radiat Oncol.*

- 2014;24(3):203-206. doi:10.1016/j.semradonc.2014.02.015
110. Heid O, Kleemann M, Heller J. Integrated MRI-LINAC Radiotherapy Machine. *Proc Intl Soc Mag Reson Med*. 2015;23(1):3068.
 111. Grein EE, Lee R, Luchka K. An investigation of a new amorphous silicon electronic portal imaging device for transit dosimetry. *Med Phys*. 2002;29(10):2262-2268. doi:10.1118/1.1508108
 112. Warkentin B, Steciw S, Rathee S FB. Dosimetric IMRT verification with a flat-panel EPID. *Med Phys*. 2003;30(12):3143-3155. doi:10.1118/1.1843471
 113. Greer PB, Popescu CC. Dosimetric properties of an amorphous silicon electronic portal imaging device for verification of dynamic intensity modulated radiation therapy. *Med Phys*. 2003;30(7):1618-1627. doi:10.1118/1.1582469
 114. McDermott LN, Louwe RJW, Sonke JJ, van Herk MB, Mijnheer BJ. Dose-response and ghosting effects of an amorphous silicon electronic portal imaging device. *Med Phys*. 2004;31(2):285-295. doi:10.1118/1.1637969
 115. Elmpt W Van, McDermott L, Nijsten S, Wendling M, Lambin P, Mijnheer B. A literature review of electronic portal imaging for radiotherapy dosimetry. *Radiother Oncol*. 2008;88:289-309. doi:10.1016/j.radonc.2008.07.008
 116. Mijnheer BJ, Gonzalez P, Olaciregui-Ruiz I, Rozendaal RA, van Herk M MA. Overview of 3-year experience with large-scale electronic portal imaging device-based 3-dimensional transit dosimetry. *Pr Radiat Oncol*. 2015;Dec 5(6):e679-87.
 117. Raaijmakers a JE, Raaymakers BW, Lagendijk JJW. Experimental verification of magnetic field dose effects for the MRI-accelerator. *Phys Med Biol*. 2007;52(14):4283-4291. doi:10.1088/0031-9155/52/14/017
 118. Essers M, Hoogervorst BR, van Herk M, Lanson H, Mijnheer BJ. Dosimetric characteristics of a liquid-filled electronic portal imaging device. *Int J Radiat Oncol Biol Phys*. 1995;33(5):1265-

1272. doi:10.1016/0360-3016(95)00108-5
119. Louwe RJW, McDermott LN, Sonke JJ, et al. The long-term stability of amorphous silicon flat panel imaging devices for dosimetry purposes. *Med Phys.* 2004;31(11):2989-2995. doi:10.1118/1.1803751
 120. Swindell W, Evans PM. Scattered radiation in portal images: a Monte Carlo simulation and a simple physical model. *Med Phys.* 1996;23(1):63-73. doi:10.1118/1.597792
 121. Hansen VN, Swindell W, Evans PM. Extraction of primary signal from EPIDs using only forward convolution. *Med Phys.* 1997;24(9):1477-1484. doi:10.1118/1.598036
 122. Spies L, Partridge M, Groh B a, Bortfeld T. An iterative algorithm for reconstructing incident beam distributions from transmission measurements using electronic portal imaging. *Phys Med Biol.* 2001;46(8):N203-N211. doi:10.1088/0031-9155/46/8/402
 123. Chuter RW, Rixham PA, Weston SJ, Cosgrove VP. Feasibility of portal dosimetry for flattening filter-free radiotherapy. *J Appl Clin Med Phys.* 2016;17(1):112-120. doi:10.1120/jacmp.v17i1.5686
 124. K Smit, DA Roberts, JGM Kok JL and BR. The impact of beam transmission through a closed bore MRI on several beam characteristics for a prototype MR-linac system. *Manuscr Prep Submiss.* Published online 2015.
 125. Court L. MRI Guided Radiotherapy: Integration of a Philips MRI scanner with an Elekta Linac.
 126. Raaymakers BW, Lagendijk JJW, Overweg J, et al. Integrating a 1.5 T MRI scanner with a 6 MV accelerator: proof of concept. *Phys Med Biol.* 2009;54(12):N229-N237. doi:10.1088/0031-9155/54/12/N01
 127. Liu B, Adamson J, Rodrigues A, Zhou F. A novel technique for VMAT QA with EPID in cine mode on a Varian TrueBeam linac A novel technique for VMAT QA with EPID in cine mode on a Varian TrueBeam linac. Published online 2013. doi:10.1088/0031-

9155/58/19/6683

128. Woodruff HC, Fuangrod T, Rowshanfarzad P, Mccurdy BMC, Greer PB, Greer PB. Gantry-angle resolved VMAT pretreatment verification using EPID image prediction Gantry-angle resolved VMAT pretreatment verification using EPID. 2014;081715(2013). doi:10.1118/1.4816384
129. Han B, Ding A, Lu M, Xing L. Pixel response-based EPID dosimetry for patient specific QA. 2017;(May 2016):9-17. doi:10.1002/acm2.12007
130. van Zijtveld M, Dirkx MLP, de Boer HCJ, Heijmen BJM. Dosimetric pre-treatment verification of IMRT using an EPID; clinical experience. *Radiother Oncol.* 2006;81(2):168-175. doi:10.1016/j.radonc.2006.09.008
131. Van Esch A, Depuydt T, Huyskens DP. The use of an aSi-based EPID for routine absolute dosimetric pre-treatment verification of dynamic IMRT fields. *Radiother Oncol.* 2004;71(2):223-234. doi:10.1016/j.radonc.2004.02.018
132. Herman MG. Clinical use of electronic portal imaging. *Semin Radiat Oncol.* 2005;15(3):157-167. doi:10.1016/j.semradonc.2005.01.002
133. Woodruff HC, Fuangrod T, Uytven E Van, et al. First Experience With Real-Time EPID-Based Delivery Verification During IMRT and VMAT Sessions. *Radiat Oncol Biol.* 2015;93(3):516-522. doi:10.1016/j.ijrobp.2015.07.2271
134. Reynolds M, Fallone BG, Rathee S. Dose response of selected ion chambers in applied homogeneous transverse and longitudinal magnetic fields. *Med Phys.* 2013;40(4):042102. doi:10.1118/1.4794496
135. Smit K, van Asselen B, Kok JGM, Aalbers a HL, Lagendijk JJW, Raaymakers BW. Towards reference dosimetry for the MR-linac: magnetic field correction of the ionization chamber reading. *Phys Med Biol.* 2013;58(17):5945-5957. doi:10.1088/0031-9155/58/17/5945

136. Raaijmakers a JE, Raaymakers BW, Lagendijk JJW. Magnetic-field-induced dose effects in MR-guided radiotherapy systems: dependence on the magnetic field strength. *Phys Med Biol.* 2008;53(4):909-923. doi:10.1088/0031-9155/53/4/006
137. McDermott LN, Nijsten SMJJG, Sonke J-J, Partridge M, van Herk M, Mijnheer BJ. Comparison of ghosting effects for three commercial a-Si EPIDs. *Med Phys.* 2006;33(7):2448-2451. doi:10.1118/1.2207318
138. Winkler P, Hefner A, Georg D. Dose-response characteristics of an amorphous silicon EPID. *Med Phys.* 2005;32(10):3095-3105. doi:10.1118/1.2040711
139. Torres-Xirau I, Olaciregui-Ruiz I, Rozendaal R, et al. A back-projection algorithm in the presence of an extra attenuating medium : towards EPID dosimetry for the MR-Linac. *Phys Med Biol.* 2017;62:6322-6340.
140. McCurdy BM, Luchka K, Pistorius S. Dosimetric investigation and portal dose image prediction using an amorphous silicon electronic portal imaging device. *Med Phys.* 2001;28(6):911-924. doi:10.1118/1.1374244
141. Greer PB. Correction of pixel sensitivity variation and off-axis response for amorphous silicon EPID dosimetry. *Med Phys.* 2005;32(12):3558-3568. doi:10.1118/1.2128498
142. Vial P, Gustafsson H, Oliver L, Baldock C, Greer PB. Direct-detection EPID dosimetry: Investigation of a potential clinical configuration for IMRT verification. *Phys Med Biol.* 2009;54(23):7151-7169. doi:10.1088/0031-9155/54/23/008
143. McCowan PM, McCurdy BMC. Frame average optimization of cine-mode EPID images used for routine clinical in vivo patient dose verification of VMAT deliveries. *Med Phys.* 2016;43(1):254-261. doi:10.1118/1.4938413
144. Nijsten SMJJG, Mijnheer BJ, Dekker ALAJ, Lambin P, Mincken AWH. Routine individualised patient dosimetry using electronic portal imaging devices. *Radiother Oncol.* 2007;83(1):65-75.

doi:10.1016/j.radonc.2007.03.003

145. Nelms BE, Rasmussen KH, Tomé WA. Evaluation of a fast method of EPID-based dosimetry for intensity modulated radiation therapy. *J Appl Clin Med Phys*. 2011;11(2):1-28.
146. Berry SL, Polvorosa C, Cheng S, Deutsch I, Chao KSC, Wu CS. Initial clinical experience performing patient treatment verification with an electronic portal imaging device transit dosimeter. *Int J Radiat Oncol Biol Phys*. 2014;88(1):204-209. doi:10.1016/j.ijrobp.2013.09.045
147. Francois P, Boissard P, Berger L, Mazal A. In vivo dose verification from back projection of a transit dose measurement on the central axis of photon beams. *Phys Medica*. 2011;27(1):1-10. doi:10.1016/j.ejmp.2010.06.002
148. Van Uytven E, Van Beek T, McCowan PM, Chytyk-Praznik K, Greer PB, McCurdy BMC. Validation of a method for in vivo 3D dose reconstruction for IMRT and VMAT treatments using on-treatment EPID images and a model-based forward-calculation algorithm. *Med Phys*. 2015;42(12):6945-6954. doi:10.1118/1.4935199
149. McCowan PM, Asuni G, Van Uytven E, et al. Clinical Implementation of a Model-Based In Vivo Dose Verification System for Stereotactic Body Radiation Therapy-Volumetric Modulated Arc Therapy Treatments Using the Electronic Portal Imaging Device. *Int J Radiat Oncol Biol Phys*. 2017;97(5):1077-1084. doi:10.1016/j.ijrobp.2017.01.227
150. Persoon LCGG, Podesta M, Nijsten SMJJG, Troost EGC, Verhaegen F. Time-Resolved Versus Integrated Transit Planar Dosimetry for Volumetric Modulated Arc Therapy: Patient-Specific Dose Differences During Treatment, a Proof of Principle. *Technol Cancer Res Treat*. 2016;15(6):NP79-NP87. doi:10.1177/1533034615617668
151. Raaijmakers AJE, Raaymakers BW, Lagendijk JJW, et al. Experimental verification of magnetic field dose effects for the MRI-accelerator. doi:10.1088/0031-9155/52/14/017

152. B W Raaymakers et al. First patients treated with a 1 . 5 T MRI-Linac : clinical proof of concept of a high-precision , high- field MRI guided radiotherapy treatment First patients treated with a 1 . 5 T MRI- Linac : clinical proof of concept of a high-precision , high-field M. Published online 2017.
153. Chen G, Ahunbay E, Li XA. Technical Note : Development and performance of a software tool for quality assurance of online replanning with a conventional Linac or MR-Linac.
154. Kontaxis C, Bol GH, Stemkens B, et al. Towards fast online intrafraction replanning for free-breathing stereotactic body radiation therapy with the MR-linac Towards fast online intrafraction replanning for free-breathing stereotactic body radiation therapy with the MR-linac.
155. Glitzner M, Crijs SPM, Denis De Senneville B, et al. On-line MR imaging for dose validation of abdominal radiotherapy. *Phys Med Biol.* 2015;60(22):8869-8883. doi:10.1088/0031-9155/60/22/8869
156. Torres-Xirau I, Olaciregui-Ruiz I, Baldvinsson G, Mijnheer BJ, Van Der Heide UA, Mans A. Characterization of the a-Si EPID in the unity MR-linac for dosimetric applications. *Phys Med Biol.* 2018;63(2). doi:10.1088/1361-6560/aa9dbf
157. Olaciregui-Ruiz I, Rozendaal R, Mijnheer B, A M. A 2D couch attenuation model for in vivo EPID transit dosimetry. *Biomed Phys Eng Express.* 2017;4(2):5027.
158. Louwe RJW, McDermott LN, Sonke J-J, et al. The long-term stability of amorphous silicon flat panel imaging devices for dosimetry purposes. *Med Phys.* 2004;31(11):2989-2995. doi:10.1118/1.1803751
159. Hackett S, van Asselen B, G F, et al. SU-F-J-148: A Collapsed Cone Algorithm Can Be Used for Quality Assurance for Monaco Treatment Plans for the MR-Linac. *Med Phys.* 2016;43(6Part11):3441. doi:10.1118/1.4956056
160. Chen GP, Ahunbay E, Li XA. Technical Note: Development and

- performance of a software tool for quality assurance of online replanning with a conventional Linac or MR-Linac. *Med Phys.* 2016;43(4):1713-1719. doi:10.1118/1.4943795
161. Rathee S, Fallone BG, Steciw S. Technical Note: <sc>EPID</sc>'s response to 6 <sc>MV</sc> photons in a strong, parallel magnetic field. *Med Phys.* Published online 2018:mp.13285. doi:10.1002/mp.13285
 162. Torres-Xirau I, Olaciregui-Ruiz I, van der Heide UA, Mans A. 2D <sc>EPID</sc> dosimetry for an <sc>MR</sc> -linac: proof of concept. *Med Phys.* Published online 2019:mp.13664. doi:10.1002/mp.13664
 163. Bol GH, Lagendijk JJW, Raaymakers BW. Virtual couch shift (VCS): Accounting for patient translation and rotation by online IMRT re-optimization. *Phys Med Biol.* 2013;58(9):2989-3000. doi:10.1088/0031-9155/58/9/2989
 164. Lagendijk JJW, Raaymakers BW, Van Den Berg CAT, Moerland MA, Philippens ME, Van Vulpen M. MR guidance in radiotherapy. *Phys Med Biol.* 2014;59(21):R349-R369. doi:10.1088/0031-9155/59/21/R349
 165. Kontaxis C, Bol GH, Stemkens B, et al. Towards fast online intrafraction replanning for free-breathing stereotactic body radiation therapy with the MR-linac. *Phys Med Biol.* Published online 2017. doi:10.1088/1361-6560/aa82ae
 166. Raaymakers BW, Jürgenliemk-Schulz IM, Bol GH, et al. First patients treated with a 1.5 T MRI-Linac: Clinical proof of concept of a high-precision, high-field MRI guided radiotherapy treatment. *Phys Med Biol.* 2017;62(23):L41-L50. doi:10.1088/1361-6560/aa9517
 167. Kupelian P, Sonke JJ. Magnetic Resonance-Guided Adaptive Radiotherapy: A Solution to the Future. *Semin Radiat Oncol.* 2014;24(3):227-232. doi:10.1016/j.semradonc.2014.02.013
 168. Vries JHW De, Seravalli E, Houweling AC, et al. Characterization of a prototype MR-compatible Characterization of a prototype

- MR-compatible Delta4 QA system in a 1.5 tesla MR-linac. Published online 2018.
169. Kaas J, Van den Wollenberg W, Van de Schoot AJAJ, Wittkämper FW, Janssen TM. PO-0994: A fast automated sanity check for online plan adaptation in MR-guided RT. *Radiother Oncol*. Published online 2018. doi:10.1016/s0167-8140(18)31304-5
 170. Bedford JL, Hanson IM, Hansen VN. Comparison of forward- and back-projection in vivo EPID dosimetry for VMAT treatment of the prostate. *Phys Med Biol*. 2018;63(2). doi:10.1088/1361-6560/aa9c60
 171. Celi S, Costa E, Wessels C, Mazal A, Fourquet A, Francois P. EPID based in vivo dosimetry system: Clinical experience and results. *J Appl Clin Med Phys*. 2016;17(3):262-276. doi:10.1120/jacmp.v17i3.6070
 172. Nailon WH, Welsh D, McDonald K, et al. <sc>EPID</sc> - based in vivo dosimetry using Dosimetry Check™: Overview and clinical experience in a 5-yr study including breast, lung, prostate, and head and neck cancer patients. *J Appl Clin Med Phys*. Published online 2018:acm2.12441. doi:10.1002/acm2.12441
 173. Cilla S, Ianiro A, Craus M, et al. Epid-based in vivo dose verification for lung stereotactic treatments delivered with multiple breath-hold segmented volumetric modulated arc therapy. *J Appl Clin Med Phys*. 2019;20(3):37-44. doi:10.1002/acm2.12538
 174. Bedford JL, Hanson IM, Hansen VN. Portal dosimetry for VMAT using integrated images obtained during treatment. *Med Phys*. 2014;41(2). doi:10.1118/1.4862515
 175. Persoon LCGG, Nijsten SMJJG, Wilbrink FJ, et al. Interfractional trend analysis of dose differences based on 2D transit portal dosimetry. *Phys Med Biol*. 2012;57(20):6445-6458. doi:10.1088/0031-9155/57/20/6445
 176. Mans A, Remeijer P, Olaciregui-Ruiz I, et al. 3D Dosimetric verification of volumetric-modulated arc therapy by portal

- dosimetry. *Radiother Oncol.* 2010;94(2). doi:10.1016/j.radonc.2009.12.020
177. Torres-Xirau I, Olaciregui-Ruiz I, van der Heide UA, Mans A. 2D EPID dosimetry for an MR -linac: proof of concept . *Med Phys.* Published online 2019. doi:10.1002/mp.13664
178. Meyer P, Noblet V, Mazzara C, Lallement A. Survey on deep learning for radiotherapy. *Comput Biol Med.* 2018;98(May):126-146. doi:10.1016/j.combiomed.2018.05.018
179. Ghesu FC, Georgescu B, Zheng Y, et al. Multi-Scale Deep Reinforcement Learning for Real-Time 3D-Landmark Detection in CT Scans. *IEEE Trans Pattern Anal Mach Intell.* Published online 2019. doi:10.1109/TPAMI.2017.2782687
180. Xu X, Zhou F, Liu B. Automatic bladder segmentation from CT images using deep CNN and 3D fully connected CRF-RNN. *Int J Comput Assist Radiol Surg.* Published online 2018. doi:10.1007/s11548-018-1733-7
181. Miao S, Wang JZ, Liao R. Convolutional Neural Networks for Robust and Real-Time 2-D/3-D Registration. In: *Deep Learning for Medical Image Analysis.* ; 2017. doi:10.1016/B978-0-12-810408-8.00016-X
182. Wang G, Ye JC, Mueller K, Fessler JA. Image Reconstruction is a New Frontier of Machine Learning. *IEEE Trans Med Imaging.* Published online 2018. doi:10.1109/TMI.2018.2833635
183. Ronneberger O, Fischer P, Brox T. U-Net: Convolutional Networks for Biomedical Image Segmentation. :1-8.
184. Nguyen D, Long T, Jia X, et al. A feasibility study for predicting optimal radiation therapy dose distributions of prostate cancer patients from patient anatomy using deep learning. *Sci Rep.* 2019;9(1):1-10. doi:10.1038/s41598-018-37741-x
185. Olaciregui-Ruiz I, Vivas-Maiques B, Kaas J, et al. Transit and non-transit 3D <sc>EPID</sc> dosimetry versus detector arrays for patient specific <sc>QA</sc>. *J Appl Clin Med Phys.* Published online 2019:acm2.12610. doi:10.1002/acm2.12610

186. Olaciregui-Ruiz I, Rozendaal R, van Oers RFM, Mijnheer B, Mans A. Virtual patient 3D dose reconstruction using in air EPID measurements and a back-projection algorithm for IMRT and VMAT treatments. *Phys Medica*. 2017;37. doi:10.1016/j.ejmp.2017.04.016
187. Ioffe S, Szegedy C. Batch Normalization: Accelerating Deep Network Training by Reducing Internal Covariate Shift. Published online 2015.
188. Nair V, Conference GH-P of the 27th international, 2010 U. Rrte Amount. *CsTorontoEdu*. 2010;(3):6421113. doi:10.1.1.165.6419
189. Drozdal M, Vorontsov E, Chartrand G, Kadoury S, Pal C. The importance of skip connections in biomedical image segmentation. *Lect Notes Comput Sci (including Subser Lect Notes Artif Intell Lect Notes Bioinformatics)*. 2016;10008 LNCS:179-187. doi:10.1007/978-3-319-46976-8_19
190. Srivastava N, Hinton G, Krizhevsky A, Sutskever I, Salakhutdinov R. Dropout: A simple way to prevent neural networks from overfitting. *J Mach Learn Res*. Published online 2014.
191. Kingma DP, Ba J. Adam: A Method for Stochastic Optimization. Published online 2014:1-15.
192. Agarwal A, Barham P, Brevdo E, et al. TensorFlow: Large-Scale Machine Learning on Heterogeneous Distributed Systems. Published online 2015.
193. McDermott LN, Wendling M, Sonke JJ, van Herk M, Mijnheer BJ. Replacing Pretreatment Verification With In Vivo EPID Dosimetry for Prostate IMRT. *Int J Radiat Oncol Biol Phys*. 2007;67(5):1568-1577. doi:10.1016/j.ijrobp.2006.11.047
194. Winkel D, Bol GH, Kiekebosch IH, et al. Evaluation of Online Plan Adaptation Strategies for the 1.5T MR-linac Based on “First-In-Man” Treatments. *Cureus*. 2018;10(4):1-7. doi:10.7759/cureus.2431
195. Kontaxis C, Bol GH, Stemkens B, et al. Towards fast online intrafraction replanning for free-breathing stereotactic body

- radiation therapy with the MR-linac Related content Effect of intra-fraction motion on the accumulated dose for free-breathing MR-guided stereotactic body radiation therapy . *Inst Phys Eng Med Phys Med Biol.* 2017;62:7233-7248. doi:10.1088/1361-6560/aa82ae
196. Chen X, Paulson ES, Ahunbay E, Sanli A, Klawikowski S, Li XA. Measurement validation of treatment planning for a MR-Linac. *J Appl Clin Med Phys.* 2019;20(7):28-38. doi:10.1002/acm2.12651
197. Uilkema S, Van Der Heide U, Sonke JJ, Moreau M, Van Triest B, Nijkamp J. A 1.5 T transverse magnetic field in radiotherapy of rectal cancer: Impact on the dose distribution. *Med Phys.* 2015;42(12). doi:10.1118/1.4936097
198. Olaciregui-Ruiz I, Vivas-Maiques B, Kaas J, et al. Transit and non-transit 3D EPID dosimetry versus detector arrays for patient specific QA. *J Appl Clin Med Phys.* 2019;20(6):79-90. doi:10.1002/acm2.12610

9.

SUMMARIES

9.1. Summary:

Radiotherapy treatments need adequate quality control (QC) to ensure a correct delivery of the prescribed dose to the target area. One of the most extended safety nets for treatments in conventional radiotherapy machines is in-vivo EPID dosimetry, which uses the dose acquired by an Electronic Portal Imaging Device (EPID) during treatment to accurately reconstruct the dose as it was delivered to the patient. Once EPID images are back-projected into the patient geometry, a comparison in 2D or 3D with the dose distribution from the treatment planning system can be performed. To quantify potential differences gamma analysis is performed. Gamma analysis is a method to identify not only differences in dose but also in distance between two 2D or 3D maps. This serves medical physicists to determine whether the delivered dose is within acceptance parameters or not, and in that case, take actions.

In this work we developed a method to validate radiotherapy treatments delivered on a novel system: the Unity MR-Linac. This machine, which combines a radiation source (linac) and an imaging device (MRI), will help to irradiate tumors more accurately by means of a new range of techniques only available thanks to the image guidance of the MRI during irradiation. The verification of such treatments can be performed by using images of the delivered beam captured by an EPID situated opposite to the radiation source, behind the cryostat of the MRI scanner. This project focuses on the adaptation of an already existing algorithm used with conventional linacs to the new physics and design characteristics of the Unity MR-linac. The main challenge for this adaptation is the presence of the MRI scanner between the patient and the EPID, acting as a secondary source of scatter and as an attenuation medium for the beam.

Chapter 2 describes the first step of the project, aimed to create a model to account for the extra scatter and attenuation measured by the panel when the photon beam irradiated by the linac traversed a mock-up of the MRI scanner consisting of a structure of 11 cm of aluminum. The parameters of the adapted algorithm were estimated by fitting EPID data to ionization chamber (IC) dose measurements for different set-ups both with and without the aluminum structure. Validation of the modified model was performed in 2D using 58 IMRT fields delivered to a slab phantom, with and without the aluminum mock-up. EPID reconstructed dose distributions were compared to planned dose distributions using the γ -evaluation method. The γ_{mean} obtained with the adapted projection algorithm was similar to that obtained with the conventional method. Dose profiles of several square fields reconstructed with our adapted algorithm showed excellent agreement when compared to TPS.

In Chapter 3 a characterization study of the EPID in the Unity MR-Linac was performed to validate the feasibility of using the panel as a dosimeter . A series of EPID images and IC measurements were used to study the effects of the magnetic field, the scatter generated in the MR housing reaching the EPID, and the inhomogeneous attenuation from the MR housing. Dose linearity and dose rate dependence were also determined. All these results were compared to the performance of similar EPID panels on conventional linacs to assess the differences (if any) of the dose-response characteristics of the panel. The results indicated that the magnetic field at the EPID level, dose rate dependence, and dose linearity show similar results compared to conventional linacs. However, it was found that gantry angle-dependent behavior of beam attenuation and scatter would pose serious challenges for the implementation of 3D in vivo dosimetry.

The first proof of concept of the complete modified algorithm was

demonstrated in **Chapter 4**. Making use of the results of Chapter 2 and 3, proper adaptations in the physics modelling to accommodate for the aforementioned challenges of the Unity MR-linac, were made. To validate the method, 25 IMRT beams were irradiated at 3 cardinal gantry angles (0° , 90° , 180°) and the EPID images acquired during delivery were back-projected to the isocenter plane. The 2D reconstructed dose distributions were compared to dose measurements using the 2D OCTAVIUS 1500 IC array (PTW, Freiburg, Germany). A method to account for the gantry-angle dependence due to the geometry of couch, bridge and cryostat was introduced.

In **Chapter 5** all the necessary ingredients for 3D in-vivo EPID dosimetry were combined and a functioning environment for radiotherapy treatment verification in the Unity MR-linac was presented. Furthermore, a direct comparison of the reconstructed dose distributions to the treatment planning system was performed. The method was first validated using data from clinical treatments of 5 patients (2 rectal cancer, 2 prostate cancer and one patient with an oligo metastasis). ‘In-air’ EPID images were acquired and used to reconstruct the 3D dose distributions which were compared against planned and measured (with the Octavius 4D system) dose distributions. Pre-treatment verification against TPS data showed $y_{\text{mean}} = 0.41 \pm 0.04$ and $y_{\text{passrate}} = 98.4 \pm 0.1$. The comparison against the OCTAVIUS 4D system showed $y_{\text{mean}} = 0.37 \pm 0.09$ and $y_{\text{passrate}} = 97.4$, 90% CI [95.2, 99.7]. In short, it was demonstrated that 3D dosimetric verification of Unity MR-linac treatments using portal dosimetry is feasible, pre-treatment as well as *in-vivo*.

The project so far has focused on dose reconstruction in the central part of the beam, with homogeneous attenuation, However, a remaining problem was to accurately reconstruct the dose in the lateral areas of strong and inhomogeneous attenuation. To solve that problem, a

study was performed in **Chapter 6** on the implementation of a deep convolutional neural network that corrects for the artifacts in the 2D dose images. A dedicated U-Net of EPID reconstructed images at the isocenter was trained using the corresponding TPS 2D dose images as ground truth. The clinical validity of the U-Net corrected dose images (the so-called DEEPID dose images) was assessed with *in vivo* verification data of 45 large rectum IMRT fields. Results showed that the use of DEEPID allows for accurate dose reconstruction using the entire EPID frame, thus enabling dosimetric verification for field sizes up to $\sim 19 \times 22$ cm² at isocenter.

9.2. Samenvatting:

Radiotherapie behandelingen hebben adequate kwaliteitscontrole nodig om de correcte afgifte van de voorgeschreven bestralingsdosis aan het doelgebied te kunnen garanderen. Een van de meest uitgebreide veiligheidssystemen voor behandelingen met conventionele radiotherapie systemen is *in vivo* EPID (Electronic Portal Imaging Device) dosimetrie. Hierbij wordt de dosis die opgenomen wordt tijdens de behandeling door een EPID gebruikt om de afgegeven dosis aan de patiënt te reconstrueren. Nadat deze terug-projectie in de patiënt geometrie voltooid is, kan het resultaat in 2D of 3D vergeleken worden met de dosisverdeling van het treatment planning systeem (TPS). De gamma analyse methode wordt hierbij gebruikt om eventuele verschillen te kwantificeren. Deze methode kwantificeert verschillen in zowel dosis als afstand tussen 2D of 3D dosisverdelingen. Dit ondersteunt klinisch fysici bij de afweging of waargenomen verschillen acceptabel zijn en indien dat niet het geval is, actie te ondernemen.

Dit proefschrift heeft als doel om een methode te ontwikkelen en valideren voor radiotherapie behandelingen op een nieuw systeem: de Unity MRI-versneller. Dit apparaat, dat een stralingsbron (versneller)

combineert met beeldvorming (MRI), heeft als doel om tumoren nauwkeuriger te bestralen door nieuwe technieken die beschikbaar zijn dankzij de MRI beeldvorming voor en tijdens de bestraling. Voor de verificatie van zulke behandelingen kan gebruik gemaakt worden van beelden van de bestraling die gemaakt worden door de EPID die tegenover de stralingsbron gepositioneerd is, achter de cryostaat van de MRI scanner. De focus van dit project is de aanpassing van een algoritme dat ontwikkeld is voor conventionele versnellers, aan het ontwerp en de fysieke eigenschappen van de Unity MRI-versneller. De grootste uitdaging hierin vormt de aanwezigheid van de MRI scanner tussen de patiënt en de EPID. Deze verzwakt de stralingsbundel namelijk aanzienlijk en is tevens een extra bron van strooistraling.

Hoofdstuk 2 beschrijft de eerste stap van het project, wat als doel heeft om de extra strooistraling te modelleren die de EPID bereikt wanneer een fotonen bundel door een model van de MRI scanner (bestaande uit een 11 cm dikke aluminium constructie) gaat. De parameters van het aangepaste algoritme zijn geschat door EPID metingen te fitten aan ionisatiekamer (IC) dosismetingen voor verschillende configuraties, met en zonder de aluminium constructie. Het model is gevalideerd in 2D waarbij gebruik gemaakt is van 58 IMRT bundels afgestraald op een platenfantoom, zowel met als zonder de aluminium constructie. De EPID gereconstrueerde en geplande dosisverdelingen zijn vergeleken met de gamma evaluatie methode. De gemiddelde gamma waarden verkregen met het aangepaste algoritme waren vergelijkbaar met die van het conventionele algoritme. Dosis profielen van verschillende vierkante velden, gereconstrueerd met het aangepaste algoritme, lieten uitstekende overeenkomst zien met het planning systeem.

In **hoofdstuk 3** wordt een karakterisatie studie gepresenteerd van de EPID in de MRI-versneller om de geschiktheid van de detector voor dosimetrie te beoordelen. Een serie EPID beelden en IC metingen zijn

gebruikt om de invloed van het magneetveld, de strooistraling van de MRI die de EPID bereikt en de inhomogene verzwakking door de MRI te bestuderen. De dosis lineariteit en de dosis tempo afhankelijkheid zijn ook bepaald. Al deze resultaten zijn vergeleken met het gedrag van dezelfde EPID detector voor conventionele versnellers om eventuele verschillen vast te stellen. De resultaten lieten zien dat zowel de invloed van het magneetveld, de afhankelijkheid van het dosis tempo, als de dosis lineariteit in de MRI-versneller vergelijkbaar zijn met conventionele versnellers. Er werd echter ook vastgesteld dat het gantryhoek afhankelijke gedrag van de verzwakking van de bundel en de hoeveelheid strooistraling een serieuze uitdaging zou betekenen voor de implementatie van 3D *in vivo* dosimetrie.

Dewerking van het complete aangepaste algoritme wordt gedemonstreerd in **hoofdstuk 4**. Door gebruik te maken van de resultaten van hoofdstuk 2 en 3 kon de modellering van de fysica zodanig aangepast worden dat de voorgenoemde uitdagingen voor de MRI-versneller opgelost konden worden. Om de methode te valideren zijn 25 IMRT bundels afgestraald bij drie hoofdrichtingen (0°, 90° en 180° gantryhoek). De hierbij opgenomen EPID beelden zijn teruggeprojecteerd naar het vlak door het isocentrum. Deze 2D gereconstrueerde dosisverdelingen zijn vergeleken met dosis metingen van de 2D OCTAVIUS 1500 IC matrix (PTW, Freiburg, Duitsland). Verder is een methode geïntroduceerd om de gantryhoek afhankelijkheid veroorzaakt door de geometrie van de tafel, de brug en de cryostaat te verdisconteren.

In **hoofdstuk 5** zijn alle ingrediënten voor 3D *in vivo* EPID dosimetrie gecombineerd en wordt een functionerende omgeving voor verificatie van behandelingen met de MRI-versneller gepresenteerd. Daarnaast is een directe vergelijking van de gereconstrueerde dosis verdelingen met het planning systeem uitgevoerd. De methode is eerst gevalideerd met data van de klinische behandeling van 5 patiënten (2 prostaatkanker,

2 endeldarmkanker en 1 patiënt met een oligo uitzaaiing). ‘In lucht’ EPID beelden zijn gebruikt om 3D dosisverdelingen te reconstrueren die vergeleken zijn met het planning systeem en met gemeten dosisverdelingen (door het Octavius 4D systeem). De vergelijking met het planning systeem liet een gemiddelde gamma waarde van 0.41 ± 0.04 zien en gamma passrate van $98.4 \pm 0.1\%$. De vergelijking met het Octavius 4D systeem liet een gemiddelde gamma waarde van 0.37 ± 0.09 zien en gamma passrate van 97.4% met een 90% betrouwbaarheidsinterval van $[95.2, 99.7]$. Kortom, dit hoofdstuk laat zien dat verificatie van behandelingen op de Unity MRI-versneller met 3D EPID dosimetrie mogelijk is, zowel zonder patiënt aanwezig als *in vivo*.

Tot hiertoe heeft het project zich toegespitst op dosis reconstructie in het centrale deel van de bundel, waarin de verzwakking homogeen is. Een niet opgelost probleem bleef echter om accurate dosis reconstructie uit te voeren in de laterale gebieden met sterke en inhomogene verzwakking. Om dat probleem op te lossen is in **hoofdstuk 6** een studie uitgevoerd naar het gebruik van een diep neurale netwerk dat de artefacten in 2D dosis beelden kan corrigeren. Een speciaal U-Net van gereconstrueerde EPID beelden is getraind en 2D dosisverdelingen uit het planning systeem zijn daarbij als referentie waarden gebruikt. De klinische validiteit van de U-Net gereconstrueerde dosis beelden (de zogenaamde DEEPID beelden) is beoordeeld met *in vivo* verificatie data van 45 grote velden van endeldarmkanker IMRT bestralingen. De resultaten lieten zien dat door het gebruik van DEEPID accurate dosis reconstructie mogelijk is voor het gehele EPID beeld; hiermee is dosimetrise verificatie van velden tot wel $19 \times 22 \text{ cm}^2$ in het isocentrum mogelijk.

9.3. Resum:

Els tractaments de radioteràpia necessiten un control adequat per assegurar un correcte lliurament de la dosi prescrita a la regió tumoral. Una de les xarxes de seguretat més esteses per a tractaments en màquines de radioteràpia convencionals és la dosimetria *in-vivo* mitjançant EPIDs, que utilitza la dosi adquirida per un Dispositiu Electrònic d'Imatges de Portal (EPID) durant el tractament per reconstruir amb precisió la dosi a dipositada al pacient. Una vegada que les imatges EPID es projecten a la geometria del pacient, es pot fer una comparació en 2D o 3D amb la distribució de dosis del sistema de planificació del tractament. Per quantificar les diferències que es troben entre la dosi prescrita i la dosi rebuda pel pacient es realitza un anàlisi gamma, un mètode per identificar no només les diferències en intensitat (dosi), sinó també les distàncies en espai entre dos mapes 2D o 3D. Això serveix als mèdics físics per determinar si la dosi lliurada està dins dels paràmetres d'acceptació o no, i en aquest cas, emprendre accions.

Aquest treball pretén desenvolupar un mètode per validar els tractaments de radioteràpia realitzats en un sistema nou: l'Unity MR-Linac. Aquesta màquina, que combina una font de radiació (linac) i un dispositiu d'imatge per ressonància magnètica (MRI), permet irradiar els tumors amb més precisió mitjançant tècniques només disponibles gràcies al guiatge que proporcionen les imatges de l'MRI durant la irradiació. La verificació dels tractaments realitzats amb aquesta màquina es pot fer utilitzant imatges del raig irradiat un cop capturat per un EPID situat a l'altre costat de la font de radiació, just darrere del criòstat de l'escàner MRI. Aquest projecte es centra en l'adaptació d'un algorisme que ja existeix i que s'utilitza en linacs convencionals, a les noves característiques físiques i de disseny de l'Unity MR-Linac. El principal repte d'aquesta adaptació és la presència de l'escàner de l'MRI

(o criòstat) entre el pacient i l'EPID, que actua com a font secundària de dispersió i com a medi d'atenuació del raig.

El **Capítol 2** descriu el primer pas del projecte, destinat a crear un model matemàtic per tenir en compte la dispersió i atenuació addicionals mesurades pel panell EPID quan el feix de fotons irradiat des del linac travessa un prototip de l'escàner MRI fet amb una estructura d'11 cm d'alumini. Els paràmetres de l'algoritme s'estimen mitjançant un procés minimització entre la intensitat de les imatges de l'EPID i les mesures de dosis capturades amb cambres de ionització (IC) per a diferents tamanyes d'irradiació, tant amb com sense l'estructura d'alumini. La validació d'aquest model modificat es va realitzar en imatges 2D mitjançant 58 camps IMRT (tractaments de radioteràpia d'intensitat modulada) irradiats i capturats amb l'EPID, primer amb i després sense la maqueta d'alumini. Les distribucions de dosis reconstruïdes amb l'EPID es van comparar amb les distribucions de dosis planificades mitjançant el mètode d'avaluació γ . Els valors de γ obtinguts amb l'algoritme adaptat van donar resultats similars als obtingut amb el mètode convencional. Els perfils de dosis de diversos camps quadrats reconstruïts amb el nostre algoritme adaptat van mostrar un excel·lent acord en comparació amb TPS.

Al **Capítol 3** es va realitzar un estudi de caracterització de l'EPID en l'entorn de l'Unity MR-Linac, per tal de validar la viabilitat a l'hora d'utilitzar el panell EPID com a dosímetre. Una sèrie d'imatges EPID i mesuraments de dosi amb IC es van utilitzar per estudiar els efectes del camp magnètic, la dispersió generada en l'estructura de l'MRI fins arribar a l'EPID i l'atenuació inhomogènia de l'estructura de l'MRI. També es va determinar la linealitat de la dosi i la cadència de la dosi (en MU/min). Tots aquests resultats es van comparar amb el rendiment de panells EPID similars en linacs convencionals per avaluar les diferències (en el cas d'haver-n'hi) en la resposta a les característiques

de la dosi en aquest entorn. Els resultats van indicar que el camp magnètic al nivell de l'EPID, la dependència de la velocitat de dosi i la linealitat de la dosi mostren resultats similars en comparació amb els linacs convencionals. Tanmateix, es va trobar que tan l'atenuació com la dispersió del raig tenen un comportament depenent de l'angle i per tant el seu modelat suposaria seriosos reptes per a la implementació de dosimetria 3D *in-vivo*.

La primera prova del concepte de l'algoritme modificat complet es va demostrar al **Capítol 4**. Utilitzant els resultats dels capítols 2 i 3, es van fer les modificacions adequades en el software per tenir en compte els canvis en el model físic i així adaptar-se als reptes ja esmentats que presentava l'Unity MR-linac. Per validar el mètode, es van irradiar 25 camps IMRT en 3 angles cardinals (0°, 90°, 180°) i les imatges EPID adquirides durant la irradiació van ser projectades al pla de l'isocentre per cada angle. Les distribucions de dosis reconstruïdes en 2D es van comparar amb les mesures de dosis obtingudes amb l'eina 2D OCTAVIUS 1500 IC (PTW, Friburg, Alemanya). També es va introduir un mètode per tenir en compte la dependència de l'angle d'irradiació degut a la geometria de l'estructura de l'MRI, del pont i de la taula de de la màquina.

Al **Capítol 5** es van combinar tots els ingredients necessaris per a la dosimetria EPID *in-vivo* 3D i es va presentar un entorn de funcionament per a la verificació de tractaments de radioteràpia a l'Unity MR-linac. A més, es va realitzar una comparació directa entre de les distribucions de dosis reconstruïdes amb EPID i el sistema de planificació del tractament (TPS). El mètode es va validar per primera vegada mitjançant dades de tractaments clínics de 5 pacients (2 recte, 2 de càncer de pròstata i una metàstasi a l'oligo). Les imatges EPID "a l'aire" es van obtenir sense pacients i es van utilitzar per reconstruir les distribucions de dosis 3D, que es van comparar amb les distribucions de dosis tant planificades

com mesurades (amb el sistema Octavius 4D). La verificació prèvia al tractament amb dades de TPS va mostrar els següents resultats de y : $y_{\text{mean}} = 0,41 \pm 0,04$ i $y_{\text{passrate}} = 98,4 \pm 0,1$. La comparació amb el sistema OCTAVIUS 4D va mostrar $y_{\text{mean}} = 0,37 \pm 0,09$ i $y_{\text{passrate}} = 97,4$, 90% CI [95,2, 99,7]. En resum, es va demostrar que la verificació dosimètrica en 3D dels tractaments a l'Unity MR-linac mitjançant EPIDs és factible, tant per verificació prèvia al tractament, així com *in-vivo*.

Tot el projecte fins ara s'ha centrat en la reconstrucció de la dosi a la part central del raig irradiat, on hi ha una atenuació homogènia per part del criòstat. Tot i això, un problema restant era reconstruir amb precisió la dosi a les zones laterals on es dona una atenuació forta i inhomogènia. Per solucionar aquest problema, es va realitzar un estudi complementari al **Capítol 6** sobre la implementació d'una xarxa neuronal (CNN) que corregeix els artefactes en les imatges de dosi 2D. Es va entrenar una U-Net dedicada amb imatges 2D reconstruïdes amb EPID a l'isocentre i les seves imatges 2D del TPS corresponents com a veritat fonamental. Es va avaluar la validesa clínica de les imatges de dosi corregides per la U-Net (les anomenades imatges de dosi DEEPID) amb dades de verificació *in-vivo* de 45 camps IMRT de recte. Els resultats van demostrar que l'ús de DEEPID permet una reconstrucció precisa de la dosi en tot el marc d'adquisició de l'EPID, permetent així la verificació dosimètrica de mides de camp fins a $\sim 19 \times 22 \text{ cm}^2$ a isocentre.

10.

ACKNOWLEDGMENTS

Uulke, first of all I would like to thank you for taking me under your supervision. You guided me thoroughly and spend time supporting and encouraging me to pursue my thesis. You gave me confidence and motivation to work towards my goals when I probably hesitated. It has been a pleasure to fall into your research group and benefit from your guidance. **Anton**, since the first day you trusted my capabilities on accomplishing this thesis. I would like to thank you for giving me the opportunity to work in such a rewarding environment as the NKI, for guiding and squeezing your busy agenda to have periodical meetings that served me to gain insight in the field.

A special thank you goes to my paranymphs **Igor** and **Tessa**, whom, in very different ways, played such a huge role during my PhD. I'm proud to say we are not just colleagues but also good friends. **Igor**, durante mis años en el NKI te has convertido en una especie de hermano mayor en Ámsterdam: me has cuidado dentro y fuera del departamento y te has preocupado para que me sintiera como en casa. He aprendido muchísimo contigo, de tu espectacular tarea en el NKI, pero sobre todo de tu positivismo y entusiasmo en la vida. Ha sido un placer trabajar a diario contigo durante estos años (y ver crecer a tus peques). Sin ti esta tesis no habría sido posible (y definitivamente menos divertida). **Tessa**, you've been the only PhD in the office I've share my entire NKI life with. That's every day! We got along so well that you hired me for the borrel committee. We've shared Incredible memories of dinners, parties, conferences and finally of my wedding (and your 'wedding' too). You were always there for me: in the funniest times, babysitting Berlin, and having endless coffees, but also during the toughest moments you were very supportive and I appreciate it most.

Zeno and **Bruno, completing the old guard**. It's been a total pleasure to share moments with both of you in the pitch and outside of it. **Zeno**, thanks for introducing me to your football team when I arrived

in town, you opened that door to me when I was barely a stranger. It was wonderful to get to know you better through football and borrels. **Bruno**, it was such a relief when you arrived to the NKI: finally some Latin blood to team up with at everything. I have the feeling that for some reason you and I immediately build some strong bonds and we just understood each other so well. I am so happy of you moving to Barcelona. **Roel** and **Patrick**, you were the dream team of the EPID room when I joined, you were a true inspiration to my research. **Ben**, your wise support and documented advise help me conduct rigorous science. **Begoña, Thjis, Jochem**, thanks for being always so supportive and willing to collaborate with tedious measurements I always needed. To **Jonas, Anja, Natashja, Martin**, it has been fun and a great pleasure to spend these years next to you. **Diedie** and **Patricia**, thank you for always being available to solve any problem, you are the safety net of this department. **Mathjis, Sander, Gauti, Vineet, Theo, Nikita, Anke**, it was short but intense. **Catarina, Natasja, Kleopatra, Tom, Uros, Edzo, Chris, Lucas**, I had the pleasure to share few years with you. **To you all** thanks for being the party people any PhD student can only dream about.

To all friends in Amsterdam, whom in one way or another were present and supportive. A special mention goes to: **Mar** for your continuous wisdom councils. Your ability to listen and positivity fueled me with energy when I needed it. **David, Laura** (and **Clara**), living in Ten Kate was probably the funniest time in Amsterdam. Thanks for your patience and joy. To **Carla, Nuria, Anaka, Marus, Paul** and **Anna**, each of you in a different way contributed to the feeling that Amsterdam was home during these years. To **Reinout**, my *Berlin's Dutch friend*. Wikipedia should have a picture of you next to the word *Friendship*. To all my friends in **Sabadell**, gràcies als terroristes, per fer que cada escapada a Sabadell ens omplís d'energia per tornar a Amsterdam fins la propera visita. To my **ETB brotherhood** friends, for our yearly reunions proving

that Berlin was just a stepping Stone of our friendship.

Georgina. Gràcies per tot. Per sempre. Per fer-me creure capaç de tot. Per demostrar-me que venir a Amsterdam va ser la millor decisió de la meua vida. Per acompanyar-me en els bons moments i sobretot per fer-me costat en els dolents. Per no rendir-nos mai. Per dir-me “sí, vull” a la caleta. Per acceptar casar-nos a Can Torres i per seguir caminant junts. Per fer-me feliç. A l'**Axel** per fer-me sentir sempre tan especial, tan valent, tan segur. Per fer-me sentir privilegiat al repetir-me l'enveja que et feia l'experiència que he viscut tots aquests anys fora. Al **Papa**, per la teua serenor, per cuidar-nos i ajudar-nos sempre. Incondicionalment. Per aguantar els cops de la manera que ho has fet. Has sigut un exemple i estic orgullós de tu. A la **Mama**, perquè has sigut i seràs sempre el motor que em dona tota l'energia positiva. Et trobo moltíssim a faltar. Cada dia. T'estimo.

11.

LIST OF PUBLICATIONS

This thesis is based on the following publications:

A back-projection algorithm in the presence of an extra attenuating medium: towards portal dosimetry for the MR-linac.

Torres-Xirau I, Olaciregui-Ruiz I, Rozendaal R, González P, J Mijnheer B, Sonke J-J, et al.

Phys. Med. Biol. 2017;62:6322–6340.

DOI: 10.1088/1361-6560/aa779e

Characterization of the A-Si EPID in the Unity MR-Linac for dosimetric applications.

Torres-Xirau I, Olaciregui-Ruiz I, Baldvinsson G, Mijnheer BJ, Van Der Heide UA, Mans A.

Phys. Med. Biol. IOP Publishing; 2018;63.

DOI: 10.1088/1361-6560/aa9dbf

Two-dimensional EPID dosimetry for the MR-linac: proof of concept.

Torres-Xirau I, Olaciregui-Ruiz I, van der Heide UA, Mans A.

Med. Phys. 2019; mp.13664.

DOI: 10.1002/mp.13664

Clinical validation 3D in-vivo EPID dosimetry in the Unity MR-linac.

Torres-Xirau I, Olaciregui-Ruiz I, Kaas J, Nowee E Marlies, van der Heide UA, Mans A.

Rad. Onc. 2020; RO-D-19-00826R2.

DOI: 10.1016/j.radonc.2020.02.010

A Deep Learning-based correction to EPID dosimetry for attenuation and scatter in the Unity MR-Linac system.

Torres-Xirau I*, Olaciregui-Ruiz I*, Teuwen J, van der Heide UA, Mans A.

Phys. Medica, 2020, EJMP-D-19-00638;

DOI: 10.1016/j.ejmp.2020.02.020

Other publications:

Fast Approximate Nearest-Neighbour Field by Cascaded Spherical Hashing

Torres-Xirau I, Jordi Salvador, Eduardo Pérez-Pellitero.

ACCV 2014; Proc. Asian Conf. on Computer Vision 2014

DOI: 10.1007/978-3-319-16817-3_30

Fast Super-Resolution via Dense Local Training and Inverse Regressor Search

Eduardo Pérez-Pellitero, Jordi Salvador, Torres-Xirau I, Javier Ruiz-Hidalgo, Bodo Rosenhahn

ACCV 2014; Proc. Asian Conf. on Computer Vision 2014

DOI: 10.1007/978-3-319-16811-1_23

Conference abstracts:

2016 - Towards Portal Dosimetry for the MR-linac: back-projection algorithm in the presence of MRI scanner

I. Torres Xirau, R. Rozendaal, I. Olaciregui-Ruiz, P. Gonzalez, U. van der Heide, J.J. Sonke, A. Mans;

ESTRO 35

**Oral presentation*

2017 - A back-projection algorithm in the presence of an extra attenuating medium: towards portal dosimetry for the MR-Linac

I. Torres Xirau, R. Rozendaal, I. Olaciregui-Ruiz, P. Gonzalez, U. van der Heide, J.J. Sonke, A. Mans

Institute Quantivision Conference 2017

**Oral presentation*

2017 - EPID dose response in the MR-Linac with and without presence of a magnetic field

I. Torres Xirau, I. Olaciregui-Ruiz, B. J. Mijnheer, U. A. van der Heide, A. Mans

ESTRO 36

**Oral presentation*

2017 - Geometric validation of a 4D-MRI guided correction strategy on the MR-Linac

van de Lindt T. N., Koopman R., van de Schoot A., **Torres-Xirau I.**, van der Heide U. A., Sonke J.J.

ESTRO 36

**Poster*

2017 - Towards EPID dosimetry for the MR-Linac: current status

I. Torres Xirau, I. Olaciregui-Ruiz, B. J. Mijnheer, U. A. van der Heide, A. Mans

ESTRO 1st Physics Workshop

**Oral presentation*

2018 - 2-D EPID dosimetry for the MR-Linac: proof of concept

I. Torres Xirau, I. Olaciregui-Ruiz, B. J. Mijnheer, U. A. van der Heide, A. Mans

ESTRO 37

**Oral presentation*

2019 - Correction of EPID images in the MR-Linac using Deep learning

I. Torres Xirau, J. Teuwen, I. Olaciregui-Ruiz, U. A. van der Heide, A. Mans

Institute Quantivision Conference 2019

**Oral presentation*

2019 - Pre-treatment portal dosimetry for the MR-Linac

I. Torres Xirau, I. Olaciregui-Ruiz, U. A. van der Heide, A. Mans

ESTRO 38

**Oral poster presentation*

2019 - Attenuation and scatter correction of portal images in the MR-Linac using Deep learning – ICCR 2019

I. Torres Xirau, J. Teuwen, I. Olaciregui-Ruiz, U. A. van der Heide, A. Mans

ICCR 2019

**Oral presentation*

CURRICULUM VITAE

My name is Iban Torres Xirau, and I was born in Barcelona on the 5th of September of 1987. I grew up in Sabadell, where I went to school and still lived during my university time. It was in 2005 when I started an integrated bachelor's and master's program in Telecommunications Engineering at the Polytechnic University of Catalonia (UPC). In the winter of 2012, as part of my degree, I applied to an Erasmus at the Technische Universität of Berlin (TUB), and for around a year I attended to several signal and image processing courses at the Computer Vision department of the TUB. Meanwhile, I also joined the Fraunhofer Institute IPK in Berlin, where I wrote my Master Thesis as a joint project between the institute, the TUB and advised by the UPC. During this period, I focused on developing an image processing software that could detect anomalies in the production of mechanical components such as screws, bolts and nuts. Then I applied for an internship as a junior researcher at the Image processing and computer vision lab of Technicolor in Hannover, where I worked for a year on topics related to image super-resolution and fast-search structures. After a very successful year at Technicolor with 2 contributions to scientific conferences, I realized I became very interested on image processing and computer vision, but most importantly on research, so I applied for a PhD at the Radiotherapy department of Netherlands Cancer Institute. This thesis describes the research conducted during this PhD on the use of EPIDs for dosimetry in the Unity MR-linac and how we paved the way from the existing back-projection algorithm for conventional linacs to the actual use of our adapted algorithm in clinical practice.

